5-2008

Axisymmetric Coanda-Assisted Vectoring

Dustin S. Allen
Utah State University

Recommended Citation

Allen, Dustin S., "Axisymmetric Coanda-Assisted Vectoring" (2008). *All Graduate Theses and Dissertations*. 90.
https://digitalcommons.usu.edu/etd/90

AXISYMMETRIC COANDA-ASSISTED VECTORING

by

Dustin S. Allen

A thesis submitted in partial fulfillment
of the requirements for the degree

of

MASTER OF SCIENCE

in

Mechanical Engineering

Approved:

Dr. Barton L. Smith Major Professor	Dr. Robert E. Spall Committee Member
Dr. Leijun Li Committee Member	Dr. Byron R. Burnham Dean of Graduate Studies

UTAH STATE UNIVERSITY
Logan, Utah

2008

Abstract

Axisymmetric Coanda-Assisted Vectoring

by

Dustin S. Allen, Master of Science

Utah State University, 2008

Major Professor: Dr. Barton L. Smith
Department: Mechanical and Aerospace Engineering

An examination of parameters affecting the control of a jet vectoring technique used in the Coanda-assisted Spray Manipulation (CSM) is presented. The CSM makes use of an enhanced Coanda effect on axisymmetric geometries through the interaction of a high volume primary jet flowing through the center of a collar and a secondary high-momentum jet parallel to the first and adjacent to the convex collar. The control jet attaches to the convex wall and vectors according to known Coanda effect principles, entraining and vectoring the primary jet, resulting in controllable r-θ directional spraying. Several control slots (both annular and unique sizes) and expansion radii were tested over a range of momentum flux ratios to determine the effects of these variables on the vectored jet angle and profile. Two- and three-component Particle Image Velocimetry (PIV) was used to determine the vectoring angle and the profile of the primary jet in each experiment. The experiments show that the control slot and expansion radius, along with the momentum ratios of the two jets, predominantly affected the vectoring angle and profile of the primary jet. The Reynolds number range for the primary jet at the exit plane was between 20,000 and 80,000. The flow was in the incompressible Mach number range (Mach< 0.3).

(85 pages)

To Cassidy, my wife, friend, and example of eternal patience and faith, and to Dr. Smith for his untiring hours spent in guiding, aiding, and encouraging this work.

Contents

List of Tables

List of Figures

Notation

a	radius of curved surface
A_c	area of control exit slot
A_p	area of primary exit slot
b	secondary jet exit slot width; exit slot width of systems involving one Coanda jet
CSM	coanda-assisted spray manipulation
d	distance between slots in parallel jets
D	primary jet diameter at slot exit
h	height of jet on plane perpendicular to the vector angle of the jet
j	distance from the exit of the Coanda jet to the tangential center of the curved surface (location of jet impingement)
J^*	momentum ratio J_c/J_p
J_c	control momentum flux $(A_c \rho u^2)$
J_p	primary momentum flux $(A_p \rho u^2)$
$\dot{m}_c$	control mass flow rate at jet exit
$\dot{m}_p$	primary mass flow rate at jet exit
P	supply pressure
p_∞	ambient pressure
p_s	surface pressure
PIV	particle image velocimetry
Q_c	control flow rate
Q_p	primary flow rate
r	radial parameter of vectored jet
R_N	Reynolds number
s	step height

SLPM	standard liters per minute
u	x-component velocity
$\tilde{u}$	velocity in the direction parallel to $\tilde{x}$
u_s	velocity of secondary flow at exit
u_0	initial velocity of primary flow
U_{xx}	uncertainty of parameter xx
v	y-component velocity
$\tilde{v}$	velocity in the direction parallel to $\tilde{y}$
w	width of jet on plane perpendicular to the vector angle of the jet; width of slot in parallel jets
$\tilde{x}$	coordinate axis aligned with the vector angle of jet
$\tilde{y}$	coordinate axis perpendicular to the vector angle of jet
y_m	distance from surface to maximum velocity of vectored jet perpendicular to the surface
Δt	time between consecutive shots in PIV
λ	control slot circumference / primary slot circumference
ν	kinematic viscosity
Φ	vector angle
ρ	fluid density
θ	rotation direction of vectored jet; angle downstream on curved surface in previous studies
θ_{sep}	separation angle in previous studies

Chapter 1

Introduction

This thesis involves the development of a spray manipulation device called Coanda-assisted Spray Manipulation (CSM). The Coanda effect, or the tendency of jets to adhere to nearby curved surfaces (with a turning radius much larger than the jet size), is a well-established flow-control methodology. This traditional method is enhanced by adding a blowing control flow to provide profile and direction control and improve the stability of a jet, spray, or flame. Since no moving parts need be in the flow, the new device will enable long-term operation of controllable jets or sprays in harsh, corrosive, or combusting environments, such as those associated with thermal sprays [1].

1.1 Thermal Spray Application

A large market exists for the application of films to large surfaces through the use of thermal spray methods; however, current methods have disadvantages including single direction spraying, high maintenance, cumbersome spray guns or mechanisms, and no control over process parameters. Thermal spray processing [1] is an established industrial method for applying "thick coatings" of metals (stainless steel, cast iron, aluminum, titanium and copper alloys, niobium and zirconium) and metal blends, ceramics, polymers, and even biomaterials at thicknesses greater than 50 micrometers. Several different processes, including Combustion Wire Thermal Spray, Combustion Powder Thermal Spray, Arc Wire Thermal Spray, Plasma Thermal Spray, HVOF Thermal Spray, Detonation Thermal Spray, and Cold Spray Coating can benefit from the ability to alter the direction of the spray. Currently, expensive robots are commonly used for this purpose.

Thermal spray coatings are used for corrosion and erosion prevention, chemical, thermal barrier and wear protection, and general metalizing on applications ranging from aircraft engines and automotive parts to medical implants and electronics. The process involves spraying molten powder or wire feedstock onto a prepared surface (usually metallic) where impaction and solidification occur. Melting typically occurs through oxy-fuel combustion in the nozzle or an electric arc (plasma spray) located just downstream of the nozzle structure. Thermal spray processes typically result in very high material cooling rates $> 10^6$ K/s. Similarly, Flame Spray Pyrolysis (FSP), a process to synthesize metal and mixed metal oxide nanoparticles, uses a flame as an energy source to produce intraparticle chemical reactions and convert liquid sprayed reagents to the final product [2]. Due to the high temperature combustion environment present in or near these process nozzles, mechanical vectoring of the nozzle is not feasible since this would place moving parts in the jet flow, reduce device durability, and severely limit directional frequency response. Furthermore, traversing a part to be coated, which is often heated to high temperatures, is costly.

Guns and spray mechanisms used in thermal spraying processes are cumbersome. As described above, in order to spray a three-dimensional surface a thermal spray gun is controlled by a robot and motion comes via a transverse system. Also, directional spraying (for example, into a bore or around a 90 degree corner) is carried out through extension arms which multiply the bulkiness of the system [1]. Much of the awkwardness of thermal spray guns is due to the intrinsic nature of thermal sprays, and the inability to coat in a multidirectional manner is an added disadvantage.

The key significance of this research is that the resultant CSM device will make it possible to control the spray direction and several thermal-spray process parameters with a single nozzle and no moving parts in or near the flow (where combustion and/or high temperatures may be present). The Coanda effect causes a jet to follow a curved surface if the radius of curvature of the surface is much larger than the jet [3]. This effect results from the reduced pressure on the inside of the turning radius. The reduced pressure effect competes with the dissipation of boundary-layer energy until the flow ultimately detaches from the surface. While potentially useful, the Coanda effect is often bistable (meaning the flow may be completely attached or completely separated depending on initial conditions)

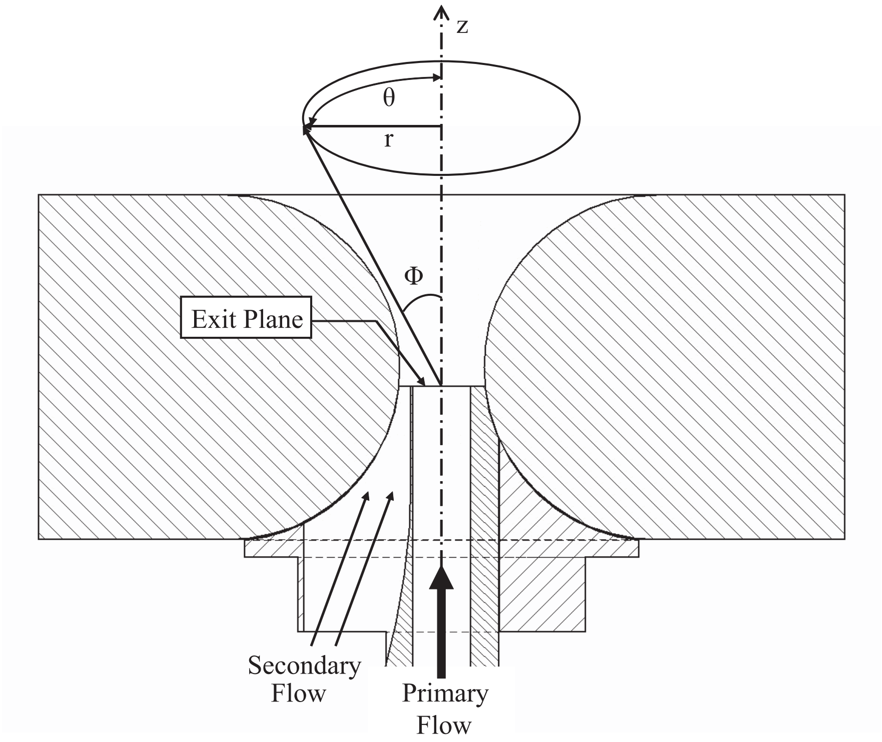

Fig. 1.1: Scale drawing of a Coanda-assisted vectoring nozzle. The application of control flow at one circumferential location will cause the primary jet to vector toward the control flow.

or even unstable, often resulting in an undesirable flapping of the flow.

Boundary layer separation, such as the separation of a jet from a Coanda surface, is often controlled by blowing through a slot parallel to the flow [4]. By applying blowing in the region where the jet meets the turning surface, as shown in Fig. 1.1, the Coanda effect can be controlled and/or enhanced. It is also possible to turn the jet over a much smaller radius with blowing. The blowing flow is applied approximately parallel to the primary flow and tangential to a curved collar. An alternative way of explaining the same process is that the control jet is under the influence of the Coanda effect and is, in turn, influencing the primary jet flow through momentum interactions. In fact, as shown below, vectoring occurs for cases where the control flow momentum flux is large compared to that of the primary flow. A similar arrangement has been used on a planar geometry for thrust vectoring by Mason and Crowther [5].

Other fluidic jet vectoring schemes may not require Coanda surfaces, but typically require larger control flows and combinations of blowing and suction such as demonstrated by Smith and Glezer [6], Bettridge et al. [7], and Hammond and Redekopp [8]. Vectoring using a Coanda surface and a synthetic jet control was demonstrated by Pack and Seifert [9]. Strykowski et al. [10] vectored a high-speed jet using an extended surface and control slot through which air was drawn.

With the Coanda-assisted vectoring scheme applied to a spray flow, by modifying the circumferential position at which the control flow is applied, the vectored spray can be rotated rapidly. Using CSM, a spray's angle can be altered constantly to maintain an orthogonal relationship to the coated surface. Coatings sprayed orthogonal to the surface have been found to exhibit higher microhardness, higher compressive residual stress, and less surface wear then off-angle spraying methods [11]. The magnitude of the vectoring and the profile of the main jet are controlled through varying the momentum flux ratio between the control jet and the primary jet. The nozzle rotates to provide rotational direction, θ in Fig. 1.1, and is the only moving part on the device. By allowing the control location to be moved to an arbitrary θ location, and by varying the vectoring angle Φ, $r - \theta$ control over a spray flow can be achieved.

1.2 Demonstration CSM

A method to address many issues discussed above is through the use of a newly designed mechanism that employs the Coanda effect. The device involves the interaction of a high volume primary jet with a high momentum secondary jet acting over a Coanda surface. The primary jet could contain powder or other particles to be applied to a substrate. The primary jet is carried through a concentric nozzle to the exit plane at the front of the device as shown in Fig. 1.2. The secondary or control flow is applied at a small exit gap, next to the exit plane of the main jet, onto a curved three-dimensional collar so that it attaches to the curved wall through the Coanda effect. The control flow entrains the primary flow through momentum interactions. In this way, the angular direction, Φ in Fig. 1.1, of the main jet is controlled.

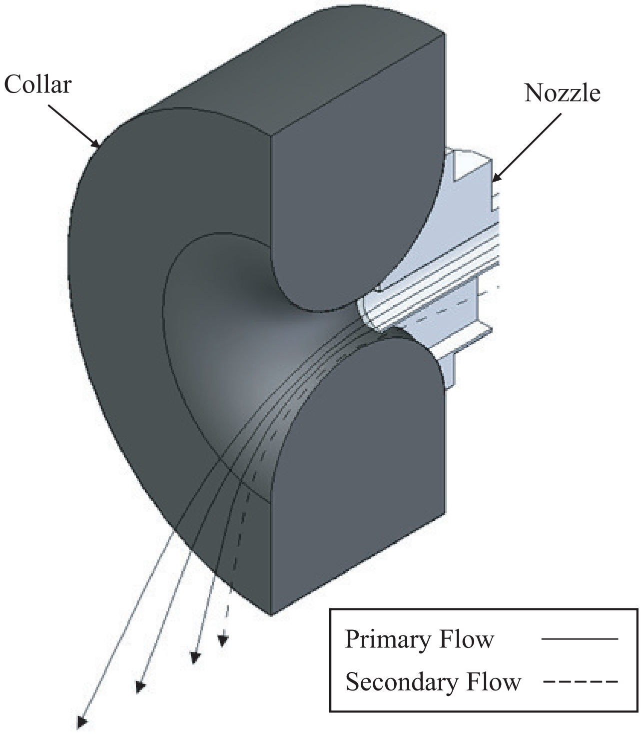

Fig. 1.2: CSM design concept showing three-dimensional exit with vectoring.

This work began with a rough prototype design as shown in Fig. 1.3. The primary jet flow was supplied through a compressed air line from the bottom of the device (A). The air then entered the jet conduit (B) which was free to rotate relative to the rest of the device. The conduit was rotated by a timing gear (C) part way up the conduit. The nozzle of the conduit (D) included a small passage (E) that channeled the control flow. The blowing control flow was also introduced at the rear of the device from a second, independent high-pressure source (F). The control flow was channeled into a plenum (G), was moved through a pressure drop to even out the flow (H), through the passage (E) and out the nozzle. The jet vectors toward the control flow at an angle that increases with the momentum of the control flow. A photo of the assembled demonstration model is shown in Fig. 1.3b.

The CSM demo had a primary jet diameter of 3.2 mm. The jet exited at the center of the collar and the collar radius to primary jet diameter was $a/D = 3.00$. The secondary slot extent was 37% of the circumference. The secondary slot width was 0.9 mm, the gap

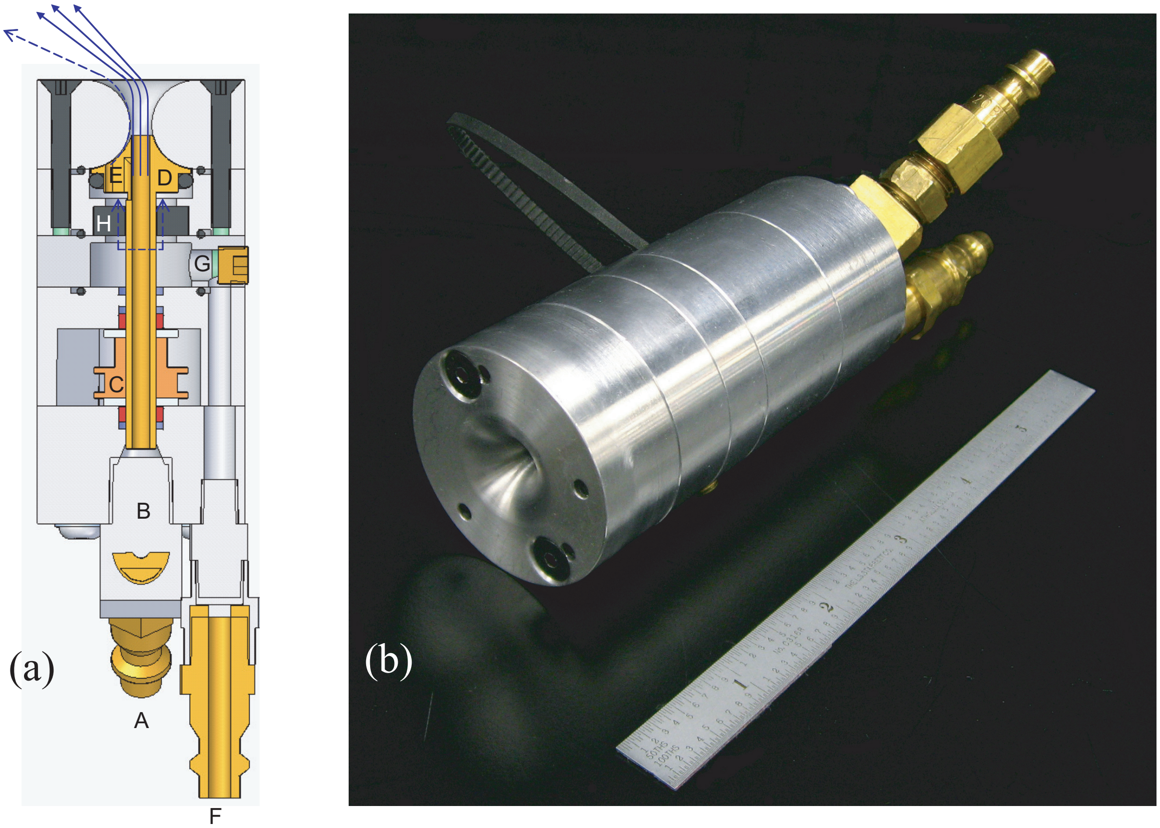

Fig. 1.3: Coanda-Assisted Spray Manipulation demonstration. (a) Scale drawing (b) Assembled device.

between the two jets to was 0.2 mm, and center of the collar was 4.8 mm in diameter. The maximum vector angle achieved was about $\Phi = 60^\circ$. The hardware used for rotation in the demonstration device limited the rotational speed to below 10 Hz for the demo.

Flow visualization was conducted in the Experimental Fluid Dynamics Laboratory (EFDL) with the prototype device using a double laser setup. The primary flow compressed air was injected with olive oil particles using a seeder and the secondary flow was simply compressed air. The flow rates were controlled independently, and many momentum flux ratios (J^*, secondary momentum flux to primary primary momentum flux) were tested to view their effect on vectoring angle. It was found that only low flow rates of the two jets would create vectoring ($Q_c = 0$ to 1.67×10^{-4} m^3/s and $Q_p = 2.5 \times 10^{-4}$ m^3/s, corresponding to $J^* = 0$ to 4.337). The lasers were set up to shoot sheets of light via sheet optics parallel

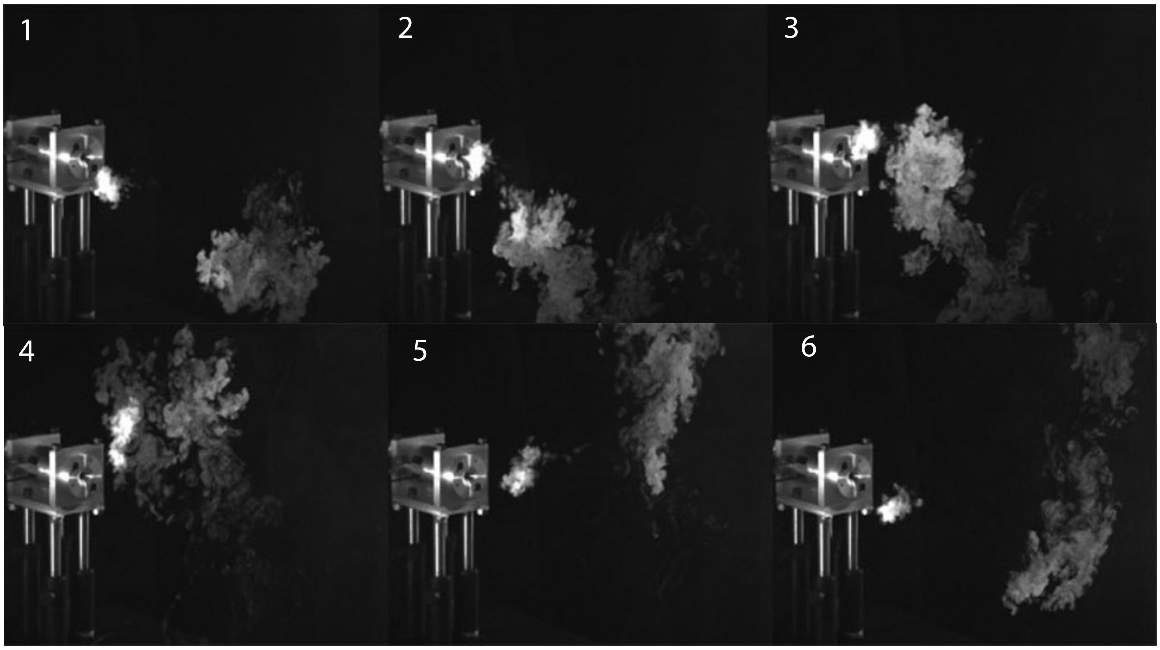

Fig. 1.4: Six frames of the CSM demonstration. The applied control flow is ramping up while being rotated in the clockwise direction.

to the exit slot of the primary jet, with the first laser sheet being a short distance from the exit plane and the second laser sheet being a short distance from the first laser sheet. A camera was set up to snap shots in cohesion with the laser pulses to generate digital photographs for flow visualization, although no quantifiable data was taken. The demonstration model was rotated at a constant speed near 1 Hz. Several frames from the demonstration are shown in Fig. 1.4.

The flow visualization showed that vectoring angle – Φ in Fig. 1.1 – increased with J^* until $J^* > 4.337$ at which point the flow no longer behaved jet-like. It was also observed that the primary jet diameter increased with momentum ratio. The flow visualization demonstrated that controlled vectoring is possible via the CSM, however the design was not optimized. The CSM could only operate at low flow rates and the main jet could not be vectored by more than 60°. The research carried out in the thesis will show tendencies of the flow in regard to the following variables: secondary exit hole size, secondary exit hole shape and upstream geometry, location of jet impingement on curved surface, size of curved wall radius, momentum ratio, and Reynolds number ratio. The knowledge of these tendencies can then be used to optimize the CSM design.

The Coanda effect has been widely used in the both aeronautics and medical applications [12], air moving technology, and other fields. Nevertheless, this phenomenon is not completely understood, especially for three-dimensional flow as in the CSM design. The nature of the Coanda effect, with boundary layer separation and entrainment interaction, make for difficulty in solving the flow numerically and analytically. In fact, Wille and Fernholz [13] claimed that there was no unique solution to this type of flow. Therefore, most recent work on the subject is based on experiments. Rask [14] and Patankar and Sridhar [15] have studied two-dimensional flows around cylindrical surfaces, looking at flow characteristics in all three dimensions (normal to surface, laterally across curved surface, and streamwise). However, to our knowledge, no research has been performed on surfaces other than two-dimensional geometries.

In order to determine the geometric and flow parameters affecting CSM control, the Coanda effect in axisymmetric geometries must be first understood. The present experiments investigate the variation of vectoring angle and jet spreading for a non-rotating axisymmetric Coanda-assisted flow as a function of the exit geometry and flow parameters and will provide guidance toward developing a more effective CSM design.

Chapter 2

Literature Review

The CSM is based on two fundamental jet principles: the tendency of a fluid to attach to and follow a curved wall (the Coanda effect) and parallel jet interaction. Both principles are interrelated through a fundamental principle of the Coanda effect: a jet attached to a curved wall will entrain the surrounding fluid [3]. In the CSM concept, the major surrounding fluid is the primary jet and the control jet (curved-wall jet) will entrain the flow of this primary jet causing the main jet to vector according to the control jet. This literature review will first present two sections providing necessary and adequate background on the two fundamental principles that work in tandem to create jet vectoring as in the CSM. Following the theoretical background, a section on applications of the two fundamental principles will be presented.

2.1 Coanda Effect

Three different phenomena are associated with the name "Coanda" [16]. The most visible is the tendency of a fluid jet initialized tangentially on a curved surface to remain attached to that surface. The effect is commonly seen in everyday jet flows such as a stream of water falling onto the convex side of a spoon. A second is the ability of a free jet to attach itself to a nearby surface. Young (1800) realized that a fluid tends toward a convex surface (as quoted in [13]) and Reynolds in 1870 described a ball suspended by a vertical jet as being held in place due to the fluid attaching to the surface of the ball (as described in [3]). The third is the tendency of jet flows over convex curved surfaces to entrain ambient fluid and increase more rapidly than that of plane wall jets. The effect is commonly associated with Henri Coanda, a Romanian inventor who was the first to employ these ideas, who received many patents for devices utilizing one or more of these effects.

2.1.1 Fundamental Theory

The landmark paper on the Coanda effect by Newman [3] investigated a two-dimensional, incompressible, turbulent jet flowing around a circular cylinder, as shown in Fig. 2.1. The nomenclature shown in the figure, as used in Newman's work, will be used consistently throughout this work.

The Coanda effect works through the balance of centrifugal forces and radial pressures [17]. As the jet emerges from the slot, the pressure on the surface, p_s, is less than the ambient fluid pressure, p_∞, due to "the slightly enhanced viscous drag experienced by the jet on the surface side." This causes the fluid to move towards the curved wall surface. The surface pressure along the curved wall rises downstream of the slot due to entrainment of

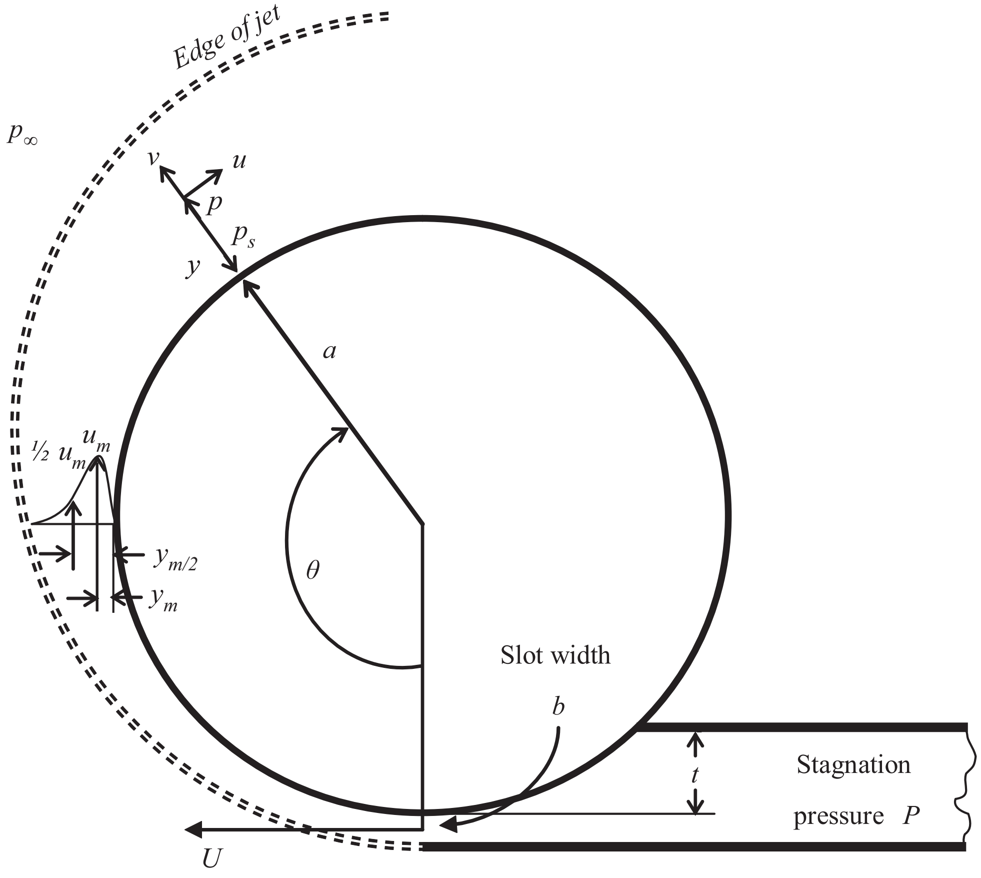

Fig. 2.1: Two-dimensional flow around a circular cylinder as shown in [3].

the surrounding fluid. Viscous effects may also contribute to the jet following the curved wall surface, though this is debateable. Bradshaw [16] said that the effect can occur in an inviscid irrotational fluid which shows that “a jet does not suck itself on by entrainment.” Assuming the flow is initially inviscid, the formula for flow derived from the Bernoulli equation is the formula $p_s = p_\infty - \frac{\rho U^2 b}{a}$, where ρ is the density of the jet fluid, U is the mean velocity, b is the slot width, and a is the radius of the curved wall (see Fig. 2.1). In an inviscid fluid, the wall pressure remains below the ambient pressure as far as $\frac{\rho U^2 b}{a} < p_\infty$. In real viscous flows, however, entrainment will cause increased jet thickness and a decrease in mean velocity, making for an adverse pressure gradient. As mean velocity decreases, surface pressure along the wall increases and eventually equals the ambient pressure. When $p_s = p_\infty$, the flow separates from the curved surface [17]. Therefore, inviscid flows may attach themselves according to the balance of centrifugal forces, but viscous effects are the cause for jet separation from the curved wall.

A second explanation involves viscous effects as the means by which the jet attaches to the curved surface. One way to demonstrate the two-dimensional Coanda effect is to bring a cylinder into contact with a free jet in ambient air [14]. A free jet entrains fluid from both sides normal to the stream. As a cylinder is brought near the jet stream, the cylinder inhibits the entrainment on that side of the jet. The ambient air on that side must then pass over the cylinder before being entrained. This causes a lower pressure on the obstructed side, curving the jet around the cylinder. Eventually if the jet is close enough to the cylinder, the flow will attach itself to the surface of the cylinder or curved wall. Therefore, entrainment causes the jet to curve and centrifugal forces balance the radial pressures as described above.

The primary parameters that describe any two-dimensional incompressible Coanda flow are the angle of separation, slot width, and radius of curvature (θ, b, and a, respectively, in Fig. 2.1). Reynolds number and pressure differential ($P - p_\infty$, where P is the supply pressure) are also governing parameters. With surrounding fluid at rest, the value of Reynolds number is inconsequential at large Reynolds numbers [18–20]. The pressure differential becomes an independent parameter at some distance downstream of the slot due to Newman's assumption that the flow depends only on the momentum for a free jet. Therefore, the angle of separation as described by Newman [3] is a function of the following form

$$\theta_{sep} = f[\{\frac{(P - p_\infty)ba}{\rho\nu^2}\}^{1/2}] \ . \tag{2.1}$$

Experimentally, the angle of separation for two-dimensional real fluids at large Reynolds numbers ($R_N > 4 \times 10^4$) and small slot width to radius ratios, b/a, remained relatively constant near 240° downstream of the slot. Other researchers have confirmed experimentally that the separation angles for two-dimensional flows are greater than 200°, with Fekete [18] citing a consistent separation angle of 210° and Rask [14] finding the separation angle to be 225°. If the fluid were inviscid and non-turbulent, the fluid would remain attached indefinitely because the pressure at the surface of the curvature would remain lower than the static pressure.

Through analytical analysis of Coanda flow at high Reynolds number, Newman [3] proposed equations for describing the flow along a cylinder. It is noted, however, that pressure distribution and velocity profiles are not discussed in this thesis as there has been adequate discussion on these topics [3, 18, 21, 22] and only θ_{sep} is crucial to this research. The angle of separation formula (2.1.1) was shown to be

$$\theta_{sep} = 245 - 391\frac{\frac{b}{a}}{1 + \frac{9}{8}\frac{b}{a}} \ . \tag{2.2}$$

Fekete [18] followed the work of Newman by experimentally investigating an incompressible wall jet flowing over a circular cylinder for velocity, surface pressure, and position of separation. As mentioned above, velocity profiles were found to be similar in the streamwise direction and similar to plane wall jets. Fekete showed that the skin friction force is negligible as long as b/a is not too small, stating that experiments where $b/a < 0.0075$ may be prone to skin friction forces. Fekete found that θ_{sep} decreases with increased surface roughness; however, with large values of Reynolds number the influence of surface roughness was nil within the roughness limits tested.

Following the work of Newman, Fekete, and others along with an increased excitement surrounding the Coanda effect at the time, a colloquium was held in Berlin in 1965 on the subject of the Coanda effect. The full proceedings of the colloquium were never published, but Wille and Fernholtz [13] have published a summary of the lectures and observations presented, as well as a background of the Coanda effect up to that point with references to previous works. The most applicable observations are those described for experimental investigations. Bradbury apparently used a setup similar to that shown in Fig. 2.1 to show that separation angle decreased with increasing pressure ratio. Gersten also used a similar test setup, varying penetration ratio (t/b), slot width to radius ratio (b/a), and jet Reynolds number. The experiments suggested that the largest deflection angle was found (assuming large Reynolds number and small b/a) where t/b is around 0.4. Fernholz found that the geometry of the nozzle exit had a large impact on deflection angle with cross-sectional aspect ratios of between 1 and 4 and b/a between 0.0714 and 0.2631. Lehmann performed tests on different insertions at the nozzle tip, reporting that a small spoiler (of height $= 0.03b$) placed at the outer edge of the nozzle lip - that opposite of the curved wall - may increase the deflection angle.

Wille and Fernholtz also discussed that measurements were to be taken in the future on logarithmic spiral curvatures. Some of these measurements were carried out by Giles *et al.* [21]. In the experiment, the jet thickness to surface radius of curvature was kept constant through the use of a logarithmic spiral curvature. The jets were found to be self-preserving and growth rates on the logarithmic spirals were larger than corresponding cylinder jets. Newman teamed up with Guitton [23] in a later work to revisit the logarithmic spiral concept. Though agreeing with Giles *et al.* that jets along logarithmic spirals can be self-preserving, they found discrepancies in the work of Giles *et al.*, namely a large difference in their experimental results as compared to results determined analytically using equations of motion. The difference (also found in Newman and Guitton's work, though to a much lesser degree) stemmed from the two-dimensionality of the flows. Variations in slot lip geometries can cause major differences in flow field downstream.

In giving an overview of turbulent curved wall jets, Newman [24] noted the “primary importance of jet momentum and the secondary importance of skin friction.” He suggested that at high Reynolds numbers, skin friction is negligible. Newman and Guitton [23] showed this was true using derivations of the momentum equations of a jet over a convex wall.

Flow visualization was the primary purpose of Panitz and Watson [25] in their experiment involving water and a birefringent milling yellow dye solution. The setup diverted from those previously described; instead of a smooth cylindrical surface, a series of three congruently angled flat plates were used and the flow around the Coanda surface was contained within a finite distance using a copper plate opposite the surface. The visualizations showed that as the jet flow rate was increased, the jet came in contact with the copper plate and reverse circulation occured. Also, conclusions on pressure profiles and flow entrainment were presented.

Bradshaw [16] gave a summary of the knowledge of Coanda flow up to the published date of the article and included many references to other works on the subject, including many of those cited in this thesis. A critical observation of Bradshaw was that velocity profiles are similar in all convex curved jets, with the only variant being possibly an increase in the maximum velocity gradient in the outer layer of the jet profile. The assumption that velocity profiles are similar for all shapes of the curved wall [3, 18, 21] and the assumption that velocity profiles of curved wall jets do not vary greatly from plane wall jets [14] allow the author to neglect a detailed discussion of velocity profiles [22, 26, 27]. Another observation was that curved wall jets entrain more and are more turbulent than plane wall jets. These are effects of additional rates of shear brought about by radial curvature.

Neuendorf and Wygnanski [28] revisited the classic experiment of a turbulent two-dimensional wall jet over a circular surface in an effort to clarify results and eliminate errors in previous research. In previous experiments, an external settling chamber was used which created an adverse pressure gradient that causes earlier jet separation from the curved wall. This experiment used an internal settling chamber. They showed that "the pressure difference between the settling chamber and the room was less than the dynamic pressure [i.e.$(p_0 - p_\infty) < \frac{1}{2}\rho U_{jet}^2$], suggesting that the flow expands to some local static pressure, p_s, that is lower than atmospheric." This confirmed earlier literature that p_s at the exit is lower than p_∞, but did not explain why the phenomenon exists.

Two regions of flow around a cylinder were defined. The first was up to $\theta = 120°$ where potential core dominates and there is a constant surface pressure. The potential core is the region in the central part of the jet stream that is virtually inviscid and irrotational and is neither effected by the boundary layer on the curved wall nor the mixing layer on the opposite edge of the jet. The flow became fully developed near $\theta = 20°$ and the velocity profiles from this point to the end of the first region matched well the profiles for flow along a plane wall. The second region runs from near 120° to the separation point (around 230°) and is characterized by an adverse pressure gradient caused by entrainment which eventually causes separation. The velocity profiles in this region no longer matched that of a plane wall, and in fact the velocity profiles changed with downstream location. In the region beyond $\theta = 180°$, the inner boundary layer grew dramatically with increasing θ and the mean velocity was pushed further away from the curved wall. The comparison was made between this lack of self-similarity and turbulent boundary layers, with the shape factor H extrapolated to the separation point being close to turbulent boundary layer values.

Neuendorf and Wygnanski suggested that the wall jet around a circular cylinder may be approximated using boundary-layer equations given that $y_m/b \ll 1$ and $\theta < 160°$. This suggests that boundary layer approximations fail a long time before separation. They also stated that entrainment, initially causing the jet to adhere to the surface, causes separation due to the disruption downstream in the sensitive balance between pressure and centrifugal forces. The constants of the experiment were $b/a = 0.0230$ and an exit velocity $U = 48$ m/s, giving a Reynolds number of 33,000.

2.1.2 Supersonic Coanda Flow

Bevilaqua and Lee [29] were possibly the first to concern themselves with two-dimensional supersonic flow over Coanda surfaces. They suggested that supersonic flows over Coanda surfaces have difficulty in initial attachment, due mainly to the balance between strong inertial forces and the necessary radial pressure gradient. In subsonic flow, the effects of the curve are transmitted upstream, therefore the jet is more likely to attach to the curved surface. Bevilaqua and Lee determined that the "principle cause of supersonic jet detachment is boundary layer separation induced by the shocks in the wave system of an underexpanded jet." At lower pressure ratios (p_∞/P, where p_∞ is ambient fluid pressure and P is the upstream stagnation pressure, see Fig. 2.1) the shocks in the wave system produced "bubbles" of minor separation with the jet reattaching after the separation. At higher pressure ratios, these bubbles eventually caused a complete separation of the jet from the radius of curvature. Although the separation phenomena can be observed, no theories were presented for predicting the point of separation.

Gregory-Smith and Gilchrist [19] continued work in supersonic flow by examining the structure of an underexpanded axisymmetric curved wall jet and the mechanism of breakaway on a Coanda flare (see Fig. 2.2). The Coanda flare jet is a three-dimensional tulip-shaped device that encourages greater entrainment in order to combust gases more efficiently, but for simplicity the examination was done only in two dimensions. Gregory-Smith and Gilchrist found the same bubble and separation characteristics that were found by Bevilaqua and Lee [29]. Hysteresis occurred in the breakaway point (hysteresis was greater for smaller b). After the pressure ratio was raised to the point of jet separation, reattachment occurred at a lower pressure ratio than the release point. Preliminary jet structure calculations were presented. This paper was followed by Gilchrist and Gregory-Smith [30] in order to expand the prediction of jet structure by presenting calculations for the jet structure of only the core region of the underexpanded jet (the region between the boundary layer and the entrainment layer). Gregory-Smith and Hawkins [31] have documented axisymmetric underexpanded curved wall jets finding values for the three mean velocities and five of the six Reynolds stresses. The tests were again conducted on a Coanda flare as shown in Fig. 2.2.

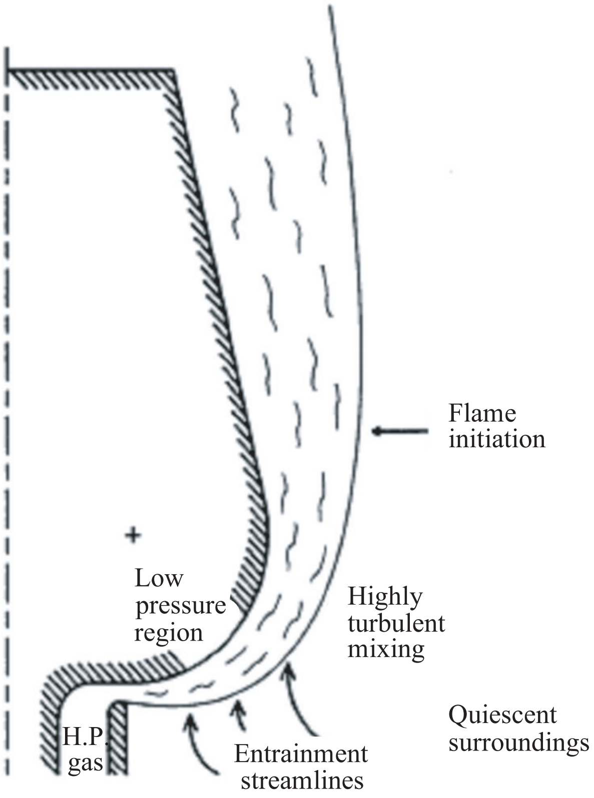

Fig. 2.2: Coanda flare as shown in Fig. 1 of [19].

In a later work, Gregory-Smith and Senior [32] continued testing on a Coanda flare; this time to determine the effects of axisymmetry and base steps on Coanda jets — both previously unstudied. The setup was much the same as in previous tests with basic geometry as shown in Fig. 2.2. The tests were conducted with a step between the slotted exit and the curved surface. The results were compared with the zero-stepped testing done previously [19]. The slot height to radius ratio (b/a) was constant at 0.1333 and step ratio of 0.125 (s/a, where s is the step height). For a full range of step and slot height variations, Gregory-Smith and Senior refer the reader to Senior's doctoral thesis [33]. The most significant attribute of the stepped flow was "the strong incoming expansion waves resulting from the reflection of the step-zone shock, which causes much earlier reattachment of the separation bubble." This quick reattachment of the jet to the Coanda surface resulted in enhanced attachment, prolonging breakaway until further downstream as compared to the zero-stepped case with consistent pressure ratios. The prolonged attachment occurs because the step caused more small bubbles that take longer to amalgamate than the large bubbles associated with zero-stepped flow. In much the same way, radial expansion also caused prolonged attachment since the radial expansion waves decreased the size of the bubbles, therefore increasing the time prior to amalgamation. Gregory-Smith and Senior state that their work was focused on outer axisymmetric Coanda flares and an important extension of the work would be to analyze internal axisymmetric Coanda jets.

Cornelius and Lucius [34] confirmed the results of those above by experimenting with a two-dimensional compressible Coanda jet at high pressure ratio citing that "jet flow detachment is brought about by large slot heights, high-pressure ratios across the nozzle, and small radii for the Coanda surface." Cornelius and Lucius also state that two-dimensional compressible flow is affected by trailing edge geometry, characteristics of the underexpanded jet, and external free stream parameters. Extending the slot wall opposite the curved surface past the tangential location of the slot improved attachment length by creating a convergent divergent nozzle.

Carpenter [17] gave an extensive overview of supersonic Coanda systems and a discussion of an axisymmetric, supersonic jet over a tulip-shaped body of revolution similar to that used by Gregory-Smith and Gilchrist (see Fig. 2.2). Carpenter recognized that design engineers have a lack of literature in the following three areas: separation and break-down characteristics, entrainment and turbulence levels, and acoustics characteristics. In this paper, Carpenter sought to review and give insight to exit nozzle and Coanda surface design. In the followup paper [35], Carpenter showed the effects of a base step and a saw-toothed exit nozzle on supersonic flow over the same surface. The base step aided in eliminating the nozzle lip shock, which increased attachment length. The saw-toothed exit nozzle showed vast improvement in the reduction of the level of noise generated.

2.1.3 Rectangular Coanda Flow

Most likely the first to experiment with the Coanda flow in three dimensions, Patankar and Sridhar [15] investigated the three-dimensional effect of turbulent, incompressible, curved wall jets. The setup was similar to that of Fig. 2.1; however, the third dimension is brought in through confining the z dimension of the jet to a finite distance (see Fig. 2.3). This type of Coanda flow will be referred to hereafter as rectangular flow in order to not confuse the reader with the three-dimensional flow of the CSM. Patankar and Sridhar varied the aspect ratios (15.6, 10.0, 5.0, 2.5, and 1.0) keeping area (0.4 sq in.) and initial velocity (140 fps) constant. Aspect ratio is defined as jet slot length (not shown in Fig. 2.1) to jet slot width. The radius of curvature was also varied in the testing (a = 6.0 in., 4.5 in., and 3.0 in.). Separation angles, θ_{sep}, were determined through droplet traces. One of the chief observations made was that θ_{sep} for rectangular flow was much less than the two-dimensional version (a maximum of $\sim 85°$ for the aspect ratios tested versus consistently greater than 200° as discussed above). Also, aspect ratio and a each had a large influence on θ_{sep}, though aspect ratio had the greatest effect. The separation angle was found to increase with both aspect ratio and radius of curvature.

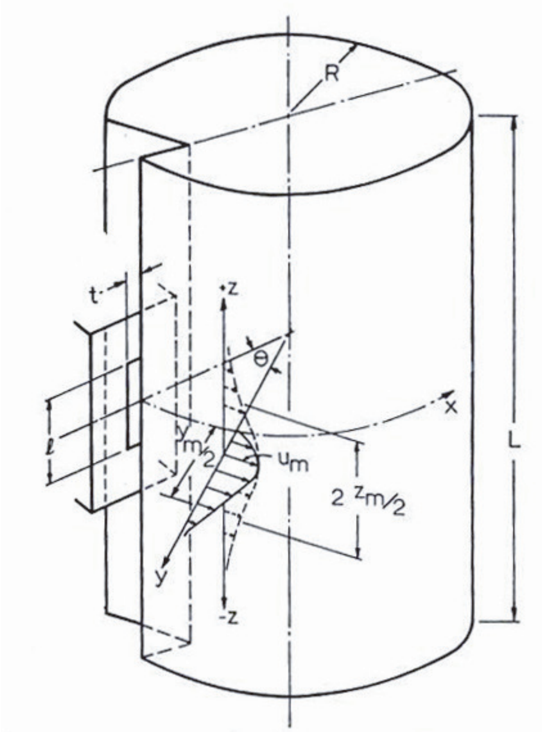

Fig. 2.3: Schematic representation of a rectangular Coanda flow field as in Fig. 1 of [15].

Following Patankar and Sridhar's work, Rask [14] completed a doctoral thesis on rectangular Coanda flow. The physical setup was similar to Patankar and Sridhar's, but Rask varied aspect ratios to a greater extent (2:1 to 40:1) and used two slot widths in his experiments (0.01 in. and 0.25 in.). Flow visualization and measurements were performed via gas tracer and hot film anemometry, respectively. Reynolds number varied between 0.9×10^4 and 5.0×10^4 depending on the aspect ratio and slot width. Rask's experiments confirmed the conclusions of Patankar and Sridhar and independently provided insight to rectangular Coanda flows. Table 2.1 shows data from the experiments of both authors to demonstrate the effect of aspect ratio and radius of curvature on rectangular Coanda flow. Rask determined separation angles from three different methods: photographs, centerline effectiveness plots, and droplets. The separation angles found through the centerline effectiveness plots are most comparable to published two-dimensional data described previously. For details on the measurement techniques, the reader is referred to Rask's work. As seen in the table, separation angle increased with aspect ratio and with a or radius of curvature.

Table 2.1: Separation Angles of Rectangular Coanda Jets (see Table 6-2 in [14])

Rask Results [14]

Aspect Ratio	Photograph θ_{sep}	CEP θ_{sep}	Droplets θ_{sep}
Thick Slot (0.01 in.)			
16 to 1	72	70	70
10 to 1	45	50	50
4 to 1	23	27	18
2 to 1	23	undet	undet
Thin Slot (0.25 in.)			
40 to 1	85	90	100
25 to 1	70	70	70
10 to 1	43	40	38

Patankar and Sridhar Results [15]

Aspect Ratio	1.0	2.5	5.0	10.0	15.6
$a = 3.0$ in.	50	60	70	77	80
4.5 in.	53	64	73	80	83
6.0 in.	64	75	80	85	87

Rask found a number of different characteristics of rectangular Coanda flow. He determined that rectangular flow was independent of Reynolds number as long as Reynolds number was high. The rectangular jets in his experiment exhibited much variation in the flow field, with large scale eddies being the major contributor to this characteristic. Flow visualization showed that eddies would attach to the curved surface up to random separation angles varying between 80 and 130° downstream of slot. Flow visualization also showed that much more turning occurred at an aspect ratio of 40:1 than at 16:1 and below the aspect ratio of 4:1 there is virtually no turning (also noticed by Patankar and Sridhar [15]).

Two other interesting phenomenon observed by Patankar and Sridhar [15] and detailed by Rask [14] are the triangular attachment pattern and the saddle shape velocity profile in the radial y direction. An equal-velocity contour plot of this phenomenon is shown in Fig. 2.4. As the three-dimensional jet exited the slot, entrainment occurred on all three sides facing ambient air. The entrainment caused the jet to separate from the curved surface not only in the radial direction but also symmetrically in the z direction. This caused an attachment trace of a triangle, which Rask found the tip of that triangle to be

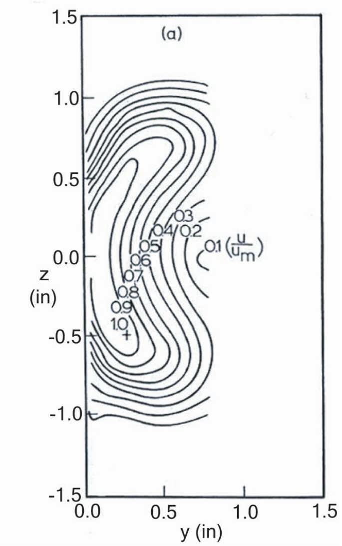

Fig. 2.4: Isotach pattern (equal-velocity contour) plot showing the saddle shape of the flow shortly downstream of a three-dimensional rectangular slot [15].

located ∼ 60° downstream. The saddle shape profile in the radial direction began near the slot exit, ran through the attachment triangle area, and may have been caused by the entrainment of the ambient air or possibly by stretched vortices as described by Patankar and Sridhar [15].

2.1.4 Coanda Effect Involving Two Parallel Flows

Juvet [20] conducted research on an axisymmetric control flow using smoke wire visualizations and hot-wire anemometry. The setup differed from previous research in two ways. First, the system was axisymmetric: a circumferential slot is used to blow air around the interior of a collar (see Fig. 2.5). Secondly, two flows were involved, a primary flow exiting a nozzle of large diameter centered in the collar with a secondary flow exiting a circumferential slot tangential to the radial surface ($D \gg b$, see Fig. 2.5).

Juvet ran tests of different blowing ratios with constant $b/a = 0.031$. Blowing ratio was define as volume flow rate of the secondary flow to flow rate of the primary flow and was varied from 0 to 0.15 (corresponding to momentum ratios of between 0.0 and 0.33). He found that with no blowing through the secondary slot, the primary jet felt little to no effects from the collar. With blowing ratios below 0.1, the primary jet width was broadened and centerline velocity decreased due to entrainment of the secondary flow. Above 0.1,

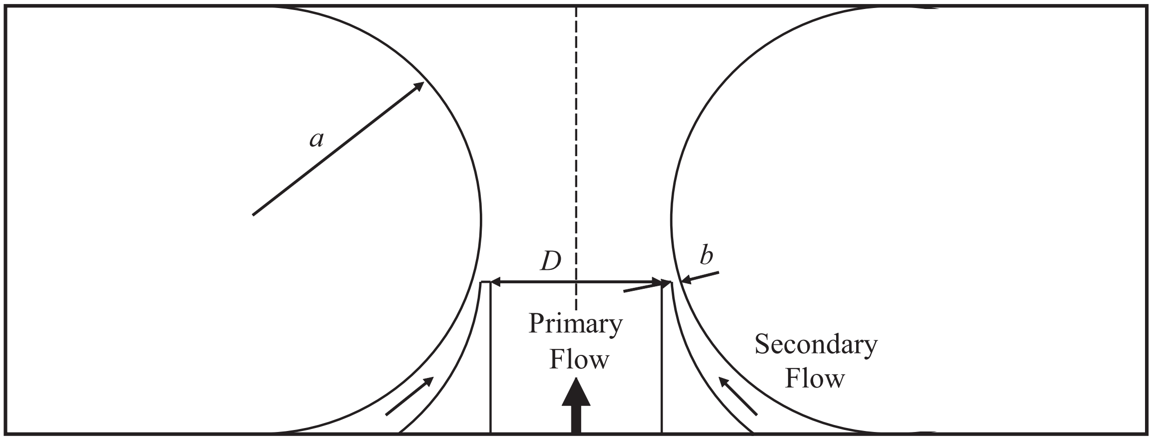

Fig. 2.5: Schematic of axisymmetric Coanda jet exit as shown in Fig. 4.1 of [20].

the main jet was vectored radially and no longer behaved like a free jet. As blowing ratio increased, the vectoring increased as was observed by the centerline velocity decreasing to null within the confines of the experiment.

Wing [36] focused on two-dimensional thrust vectoring of a primary jet using a secondary jet deflected via a Coanda surface as shown in Fig. 2.6. Using paint flow and schlieren photography for visualization and six-component strain-gauge balance for force and moment measurements, Wing found only slight vectoring of the main jet, the largest vectoring being only 6 degrees. Wing suggested that there may not have been enough momentum in the primary jet and that the nozzle may not be optimized in order to produce larger vectoring angles. Geometries of the nozzle and flow rates of the two jets may also be to blame for the small angle of deflection. Wing had set up the system to coincide with then-current aircraft designs. A detailed description of the system used is not within the scope of this work; the reader is referred to Wing's work for detailed dimensions, flow rates, pressure ratio, etc. It is noted here, however, that the mass flow rate ratio (secondary jet to primary jet mass flow rates) was varied between 0.0 and 0.1, and b/a was held constant at 0.2966 — which

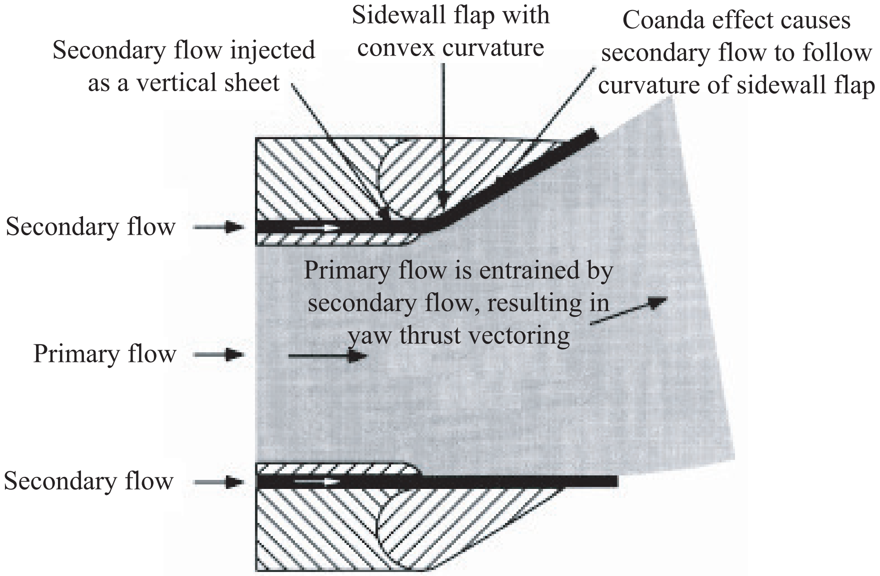

Fig. 2.6: Top view of two-dimensional convergent-divergent nozzle using the Coanda effect to produce yaw thrust vectoring in a compressible flow as shown in Fig. 1 [36].

is much larger than slot width to radius ratios used in most other experimental tests.

Mason [5] followed the work of Wing [36] by analyzing coflow fluidic thrust vectoring in the much the same way Wing had done. Mason used a two-dimensional setup shown in Fig. 2.7. The experiment used only one slot for secondary blowing, although the slot height, b, is varied throughout the experiments. The nondimensional geometric parameters were varied according to $0 \leq a/D \leq 1$ and $0 \leq b/D \leq 0.08$, corresponding to $0.007 \leq b/a \leq 0.242$ which falls in line with previous work. The primary flow rate was held constant while the secondary flow rate was varied throughout the tests making the mass flow rate ratio range $0 \leq \dot{m}_c/\dot{m}_p < 0.13$ and the momentum flow ratio range $0 \leq J_c/J_p < 0.4$.

Although Mason was focused primarily on thrust force, the data presented can also relate to jet vector angle. The vectoring angle was better than that found by Wing [36] in a similar test, but the largest angle achieved was still relatively small near 35°. Mason's found that three regions existed as momentum ratio or flow ratio was increased. The first region was characterized as the "dead zone" where the flow was sporadic and includes an negatively vectored occurrence. The second region was the "control" region where the vector angle versus momentum ratio or flow ratio was mostly linear and could be controlled. The

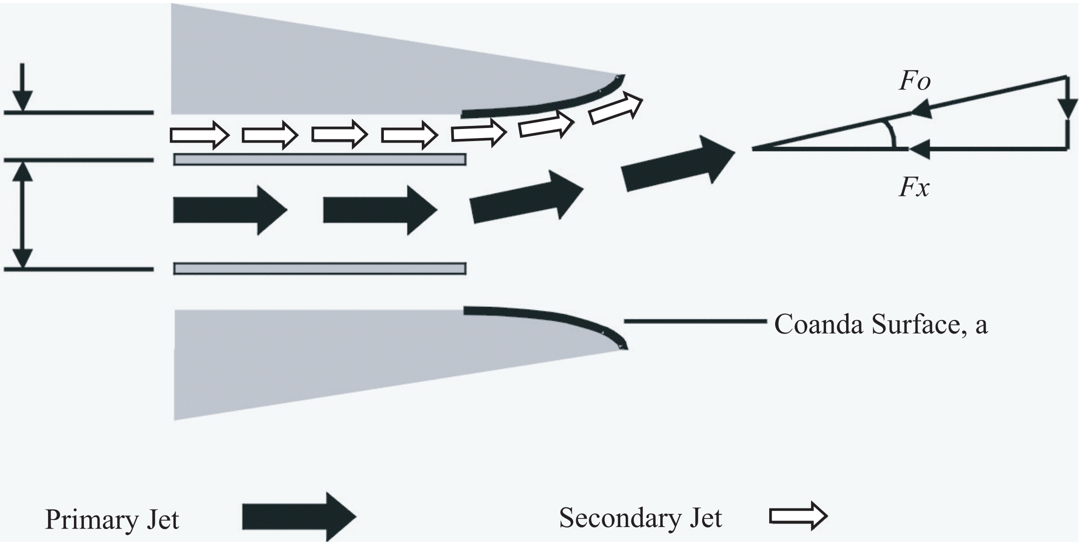

Fig. 2.7: Side view of two-dimensional nozzle using coflow Coanda effects to produce thrust vectoring as illustrated by Mason [5].

third region was the “saturation” region where the vector angle no longer increases with increased momentum or flow ratio. This work relates more directly to the present study than any known by the author.

2.1.5 Numerical Simulations for Coanda Flow

Only a brief overview of numerical studies will be presented as Coanda flow is difficult to solve numerically and experimental results are more pertinent to the thesis. Parks and Peterson [37] apply similarity analysis to approximate two-dimensional laminar Coanda flow, finding mass entrainment, thrust, and jet-sheet thickness formulas. The analysis is valid only for $b/a \ll 1$ and for Reynolds number less than 3×10^4. Moser [27] uses direct numerical simulation on low Reynolds number convex and concave surfaces finding consistent results with experimental data. Sawada [38] writes a solution for two- and three-dimensional supersonic Coanda jets, however the code only matches experimental data for the first few lengths downstream of the exit nozzle. Wernz and Fasel [39] have recently been studying turbulent Coanda flow using three-dimensional Navier-Stokes simulations and Direct Numerical Simulations providing theories and data on the streamwise and spanwise vortices.

2.2 Parallel Jet Interaction

The interaction between parallel jets is important to the effectiveness of the CSM. The marquee function of the CSM is the ability of the secondary jet to entrain the primary jet that emerges parallel to the secondary jet. The enhanced entrainment caused by the Coanda effect and the effect of parallel jets in a Coanda environment have already been discussed (most notably Juvet [20] and Wing [36]). Beyond the Coanda literature in print, no known research on parallel jets in the area of a curved surface has been conducted previously. It is assumed, however, that the flow field effects of the combination of parallel jets and a curved surface would differ greatly from plane parallel jets. This being the case, only a brief introduction into parallel jets will be discussed here.

The research listed here on parallel jets involves twin submerged jets of the same fluid emerging from the same exit plane with different and similar fluid properties (varying exit slot geometry, jet velocity ratios, momentum ratios, etc.). Lin and Sheu [40] characterized parallel jet flow by describing the three regions of the flow: converging, merging, and combined regions. The converging region is the region directly downstream from the exit plane in which the two jets converge toward one another due to entrainment. In this region, an area exists between the jets where there is lower pressure. The merging region exists when the streamwise velocity is maximum in this region and the two jets merge dramatically. The combined region occurs where the two jets combine and behave very similar to a single jet.

Bunderson and Smith [41] experimented with plane parallel jets to examine the “flapping” or instability that arises when the momentum flux ratio of the two jets approaches unity. The oscillations that are due to Reynolds stresses were found to enhance the large-scale mixing of the two jets. The instability was a function of both the geometric dimensions of the plane jets, including the jet widths and the space between the jets, and the momentum flux ratio. Maximum “flapping” and in turn maximum mixing occured when the momentum fluxes matched. When the momentum fluxes were mismatched by greater than a factor of three, the flows became steady. It was demonstrated through Schlieren flow visualization that the larger momentum jet always entrains the lower momentum jet for higher momentum ratios. This happened regardless of which plane jet had the larger jet width, for the geometries and flow rates tested.

Anderson et al. [42] experimented with plane parallel jets that had a much smaller jet width to slot distance ratio $0.6 \leq w/d \leq 2.0$. It was observed that the reduced frequency decreased with increasing jet width to slot distance ratio. They also found that for the geometries and flow rates used, at near seven slot widths downstream of the exit plane the two parallel jets would converge completely and act as a single turbulent jet as shown in Fig. 2.8.

Fujisawa et al. [43] examined the effects of parallel jets with differing velocities issuing into an ambient fluid. The experiment used PIV and dye-induced flow visualization to

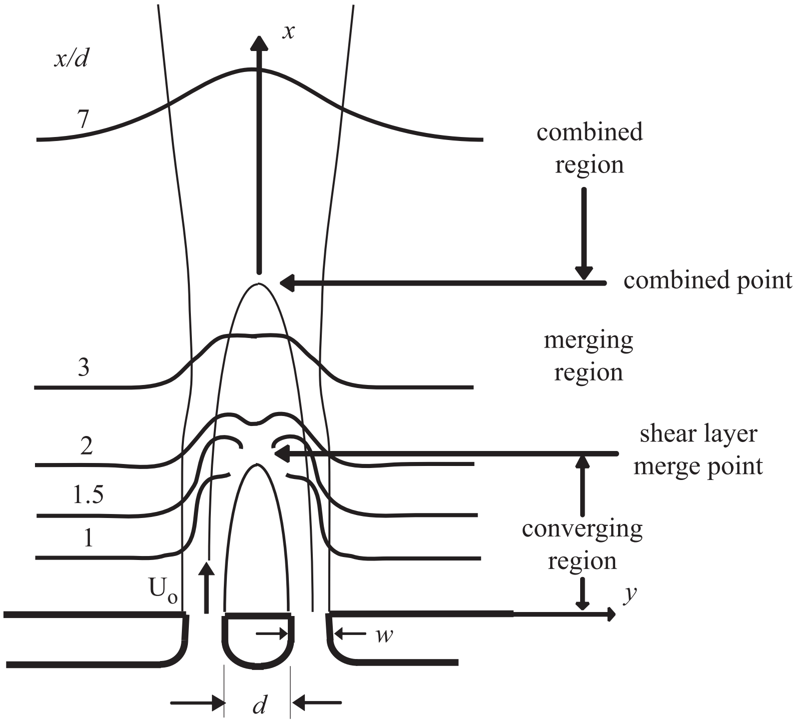

Fig. 2.8: Plane parallel jet flow with small w/d as shown in Fig. 1 of [42]).

show that parallel plane jets with velocity ratios less than unity (the velocity ratios ranged between 1 and 0.25) caused the higher velocity jet to entrain the lower velocity jet causing a modified trajectory towards the higher velocity jet region. The testing showed that interaction between the two parallel jets was weakened and the converged jet width was decreased with a decrease in velocity ratio (or increase in the difference between the two velocities). The authors stated that entrainment was proportional to velocity and that turbulent mixing was weakened with decrease in velocity ratio. Another important observation of the work was that the converging of the two jets into virtually a single jet occurs earlier with lower velocity ratios.

2.3 Applications of Coanda Effect and Parallel Jet Interaction

This section deals with some of the known applications of the Coanda effect and, separately, the known applications of parallel jet interaction.

Flow control is a primary application of the Coanda effect. Wille and Fernholz [13] discussed various applications up to the time of the colloquium. The major application has been in the aerodynamics industry in circulation-control aerofoils and wings (see Englar for a more recent overview of circulation control in aerodynamics [44]). More specific applications include reaction turbines, swirl atomizers, and fluid logic devices including an artificial respirator. Warren [45] and Joyce [12] both described the use of the Coanda effect in fluidics. More obscure uses of recent flow control are seed separation and dispersion [46] and air movers [47].

The enhanced entrainment of the Coanda effect is also useful to many applications. Jets along a cylindrical surface can be used to cool the surface [13]. High-pressure gas flares employ the Coanda effect by making use of enhanced entrainment to more efficiently burn excess gases in refineries (see examples of gas flares in [17] and also the gas flares used in [19], [30], [31], and [32]). Carpenter [17] also listed burners and other combustors as applications, along with Coanda jet pumps.

Parallel jets have many applications in flow control and mixing mechanisms. Bunderson and Smith [41] noted that both active and passive flow control methods exist and that many of those applications include the introduction of streams into enclosed chambers such as fuel and chemical mixers and the exhaustion of jets into ambient air such as in exhaust stacks and VSTOL aircraft. Fujisawa et al. [43] listed a few different parallel jet applications such as in gas turbine combustion chambers, automobile air conditioning units, and air curtain units for refrigeration systems.

Chapter 3

Approach

3.1 Objectives

The purpose of this research is to determine which parameters effect the control of the CSM. This information will be used to further develop the CSM technology. The objectives of the research are as follows:

- Use particle image velocimetry to determine the effects of the location of control jet impingement onto the curved surface on the primary jet's shape and vector angle.
- Use particle image velocimetry to determine the effects of CSM geometry at the secondary jet exit on the primary jet's shape and vector angle.
- Use particle image velocimetry to determine the effects of the momentum flux ratio on the primary jet's shape and vector angle.

The procedures that were carried out are in fulfillment of these objectives. The research was conducted using a non-rotational CSM test facility designed and built to examine the parameters outlined above. This chapter first outlines the experimental facility followed by a description of the specific experimental instrumentation. The Particle Image Velocimetry (PIV) measurement techniques are then described with a section on the data that was collected. The concluding section discusses the uncertainty analysis of the data.

3.2 Experimental Facility

The test CSM was manufactured to be similar to the current prototype design, but was much larger and did not rotate. The test CSM was made larger to reduce errors in manufacturing flaws (such as material or fit-up inconsistencies) and improve PIV data acquisition through a larger fluid jet to be analyzed. Eliminating the rotary mechanism simplified

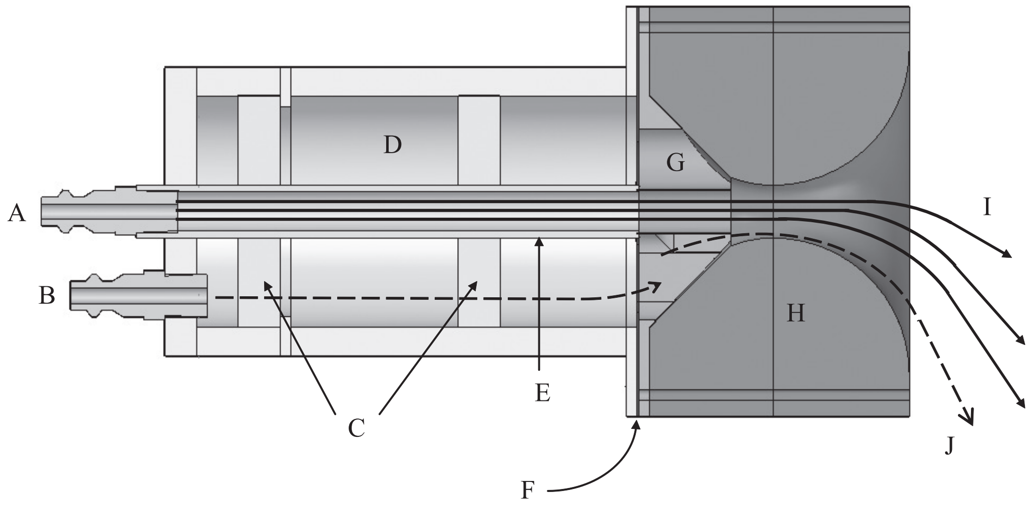

Fig. 3.1: Sketch of experimental test CSM facility. The solid streamlines represent the primary flow, while the control flow is indicated with dashed lines.

the system. The effects of rotation are secondary as compared to the effects of geometry and momentum ratio. A sketch of the test setup is shown in Fig. 3.1.

The primary (A) and the control (B) high-pressure-air flows entered separately at the rear of the test setup. The primary flow was channeled via a conduit (E) directly through the setup to the collar (H) at the exit. The control flow entered a plenum (D) that contained two flow conditioning sections (C) in order to spread the flow evenly. From the plenum, the flow was directed to a control slot (G), and a gasket (F) was used to close off slots that were not being used (each part G had several different slots, only one of which was used at any time). The exiting control flow was vectored (J) around the collar (H) by the Coanda effect and through entrainment, the primary flow (I) was vectored as well. Excepting the diffusers and the central tube, the test CSM is built entirely of Alloy 6061 Aluminum (as in the prototype model). Interchangeable parts include the flow directing gasket, the modulator, and the collar. The momentum ratio (J^*) was also changed according the the testing requirements.

The test facility was designed to allow several different geometric variations, including the collar radius a, the location of jet impingement j, and the circumferential extent of

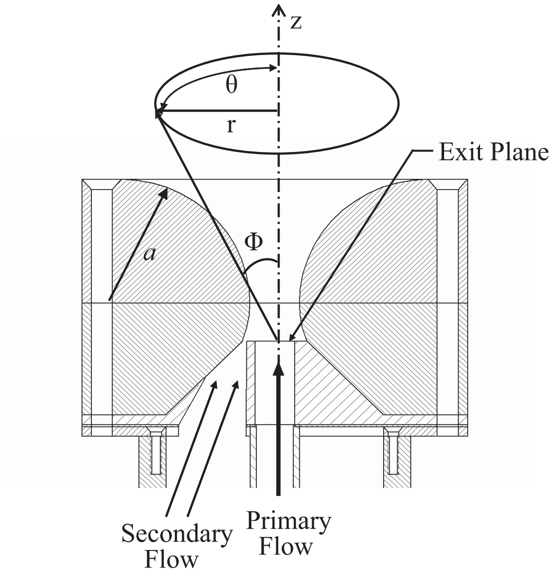

Fig. 3.2: Scale drawing of a Coanda-assisted vectoring nozzle of the test setup.

the control slot (see Fig. 3.2). Fig. 3.3 shows the geometries of the slots at the exit plane graphically from a view looking into the jet. Two different parts comprising a total of five different control slots were used. Machine shop drawings for modulators, collars, and test assembly can be found in Appendix B.

The primary jet, which had a diameter of $D = 12.7$ mm, emerged from a circular exit. The control slots were annular, with the slot width $b = 3.4$ mm. Circumferential percentages (based on the smaller radius) of 11.1%, 15.1%, 19.4%, 29.5%, and 50.0% were used. The gap between the jets at the exit plane was constant at 0.6 mm. The collar had a diameter of 15.9 mm at the most narrow position.

The point at which the control jet impinged upon the curved surface was examined using three jet exit locations. These locations were provided by three separate modulators (see Fig. 3.4). The first location was exactly at the center of the collar, the second was one diameter upstream of the collar center, and the third was two diameters upstream of the collar center. As shown in the results, it was found that the first location reduced vectoring, the third location improved vectoring but increased unwanted spreading of the jet, and the second location provided the desired vectoring and mixing. Therefore the second location, one diameter upstream of the collar center, was chosen for the secondary slot size study.

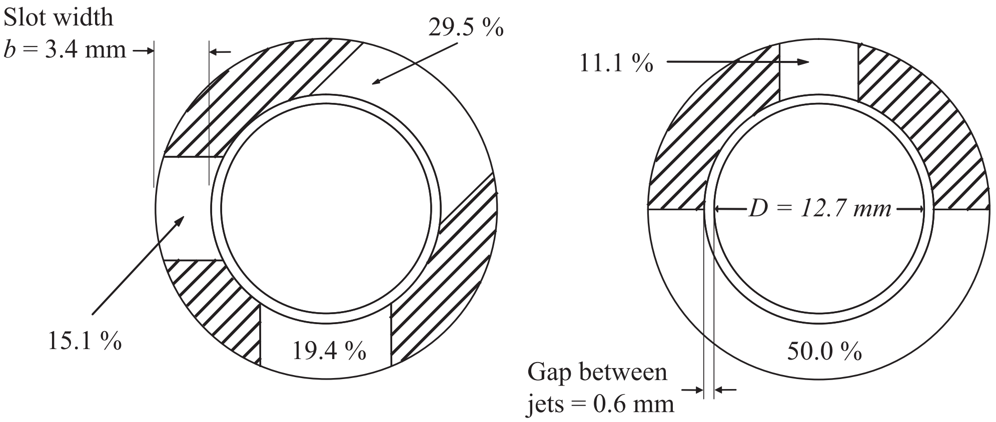

Fig. 3.3: Sketch of the control slots as viewed looking into the jet exit. All control slots had the same width, but different circumferential extents, shown as percentages of the total circumference. One slot was used for each test.

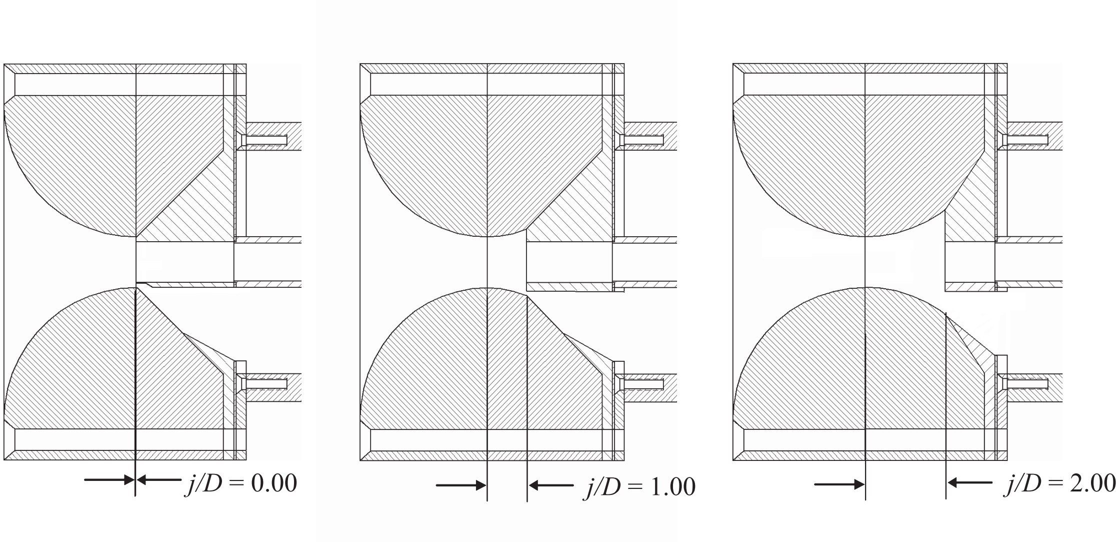

Fig. 3.4: Side cutout views of the test facility with varying locations of jet impingement (j).

The four radii used, $a/D = 2.00, 2.75, 3.25, 5.25$, provided a range of between 0.051 and 0.133 for b/a. These values correspond to similar ranges used in previous experiments (Newman's range 0.0067 to 0.0400 [3], Fekete's range 0.0074 to 0.0531 [18], Patankar and Sridhar's range 0.0266 to 0.1053 (1972) [15], a range of 0.08 to 0.24 for Fujisawa and Kobayashi [48], and 0.023 to 0.068 for Neuendorf and Wygnanski [28], to name a few). The effects of a discontinuous radius will not be examined. Fekete [18] shows that surface roughness has an effect on the Coanda flow. Each of the curved surfaces to be used will be machined, unpolished Alloy 6061 Aluminum. The material is constant throughout the testing in order to eliminate any dependency on surface roughness.

The momentum rates were controlled independently, and many values of momentum flux ratio were tested to view their effect on vectoring angle. The form of the momentum flux ratio, assuming uniform flow at the exit, is

$$J^* = \frac{J_c}{J_p} = \frac{\dot{m}_c^2}{A_c \rho} / \frac{\dot{m}_p^2}{A_p \rho} \ , \tag{3.1}$$

where J_c is the control momentum flux, J_p is the primary momentum flux, A_c is the control exit slot area, A_p is the primary exit slot area, $\dot{m}_p$ is the primary mass flow rate, $\dot{m}_c$ is the control mass flow rate, and ρ is the fluid density.

3.3 Instrumentation

The instrumentation involved in the PIV test are the mass flow controllers, the seeder, the laser, the camera(s), and the software involved in determining displacement and velocity data.

Two, independent, Porter model 204A mass flow controllers were used in the experiment. The primary mass flow controller was rated up to 1000 SLPM, while the control jet mass flow controller was rated up to 200 SLPM.

Since the fluid blown through the CSM into ambient air was compressed air the blown fluid needed to be visually different in order to visualize the flow. Small olive oil particles were fed into the primary flow and illuminated in the downstream laser plane to create an image with lighted flow and unlighted ambient air. A seeder was used to create the size of seed particles needed for PIV (small enough in size that viscosity effects overcome the weight of the particles forcing them to move with the compressed air flow). The seeder was an in-house made Laskin nozzle blowing compressed air into a chamber of olive oil to create the particles and funneling the small-enough particles into the test flow.

Two separate PIV systems were employed in the testing. The first was a single camera, two-component, system. A 12-bit, 1.3-MPixel (1280 × 1040) camera acquired images of seeded flow illuminated by a pair of 532 nm wavelength, 50 mJ Nd:YAG lasers with sheet optics. The second PIV system was a stereo (two camera) system that returns three-dimensional velocity components. The laser was the same used in the previous setup and the two cameras were identical to that used before. Both systems used LaVision DaVis software to compute the velocity vectors. The PIV system employed a dedicated computer custom built by LaVision containing two Intel Xeon 2.80 GHz processors. LaVision software utilizes an algorithm to cross correlate the light variations of the digital images and produce velocity vectors. The data outputted from the LaVision software will be manipulated via a low level code to generate the maximum velocity values at the specified location downstream and in turn the vectoring angle. The final interrogation regions were 16 × 16 pixels for both systems. The time between images was set to ensure that the maximum particle displacement was near 5 - 10 pixels for the two-component system and near 4 pixels in the three-component system.

3.4 Measurement Techniques

For the two-component PIV measurements, the beam was cast perpendicular to the CSM exit plane. The control flow was applied at a location such that the jet always vectored in a direction inside the laser plane (see Fig. 3.5a). These measurements were used primarily to determine the vector angle. For the stereo measurements, the beam was directed parallel to the CSM exit plane at a fixed distance downstream (see Fig. 3.5b). These measurements were used primarily for determine the resultant mixing of the jet.

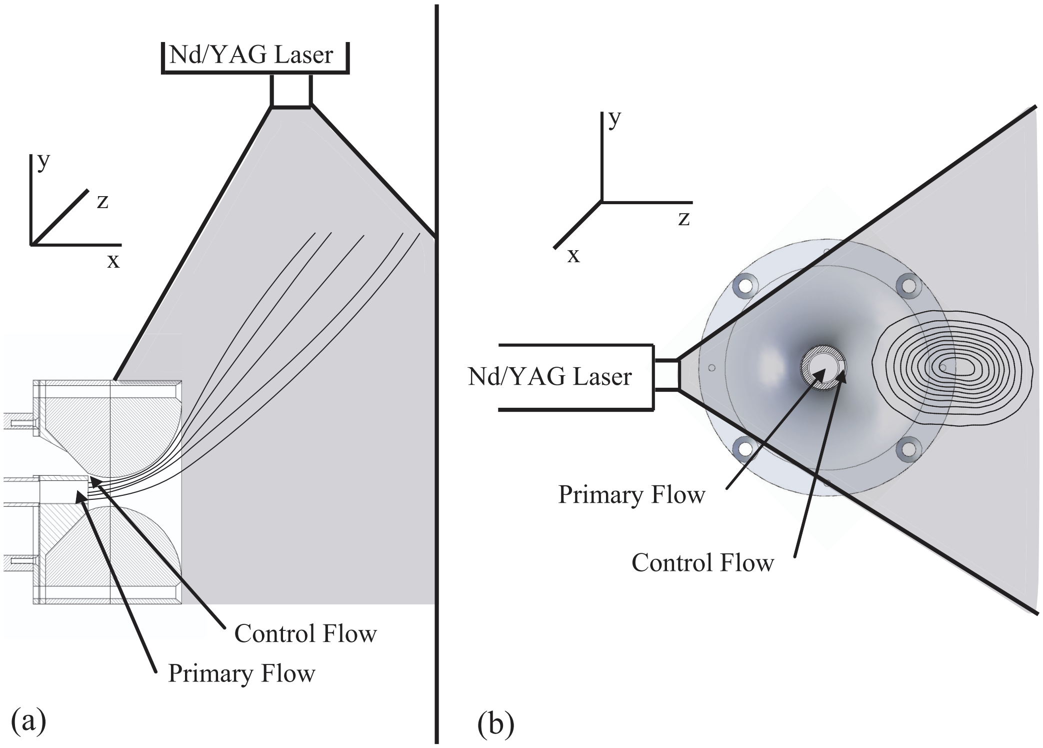

Fig. 3.5: Laser sheet configuration of two-dimensional (a) and stereo (b) systems.

Table 3.1 shows the matrix of geometries tested (for more test details see all test parameters in Appendix A.2 and A.3). The radius of the collar, a, was varied between 25.4 mm and 66.7 mm and the control jet varied from 11% to 50% of the total circumference. For each control jet exit slot geometry, the control mass flow rate to primary mass flow rate was varied between 0.0 and 1.0. In doing so, the momentum flux ratios varied between 0.00 and 7.75. The Reynolds number range for the primary jet at the exit plane was between 20,000 and 80,000. The flow was in the incompressible Mach number range (Mach$<$ 0.3).

Table 3.1: Geometric Variation Matrix (2D = Test via Two-Component PIV, 3D = Test via Three-Component PIV)

$a/D =$	2.00	2.75	3.25	5.25
Slot Size				
11.1%	2D	2D	2D, 3D	2D
15.1%	2D	2D, 3D	2D	2D
19.4%	2D, 3D	2D	2D	2D, 3D
29.5%	2D, 3D	2D	2D	2D, 3D
50.0%	2D	2D, 3D	2D, 3D	2D

For each combination of geometry and jet momentum flux, 100 two-dimensional PIV images were taken and averaged to generate mean velocity vector fields. A sample averaged velocity vector field is shown in Fig. 3.6.

When determining the vector angle of the jet, we chose not to include the entrainment regions of the jet. For each averaged velocity vector field, the standard deviation of velocity was calculated. A jet mean angle was assessed by averaging the angle for all locations where the mean jet velocity exceeds the standard deviation of velocity. The coordinate system was then shifted so that the x coordinate was parallel to the jet vectoring angle. This coordinate system is denoted $(\tilde{x}, \tilde{y})$ and has corresponding velocity components $\tilde{u}$ and $\tilde{v}$. The origin of rotation was the center of the primary jet exit. Note that the collar extends downstream of this point. At $8D$ downstream of the jet exit along this angle, the $\tilde{x}$ and $\tilde{y}$ momentum components were calculated according to $\int \rho \tilde{u}^2 \, \mathrm{d}\tilde{y}$ and $\int \rho \tilde{u}\tilde{v} \, \mathrm{d}\tilde{y}$, respectively.

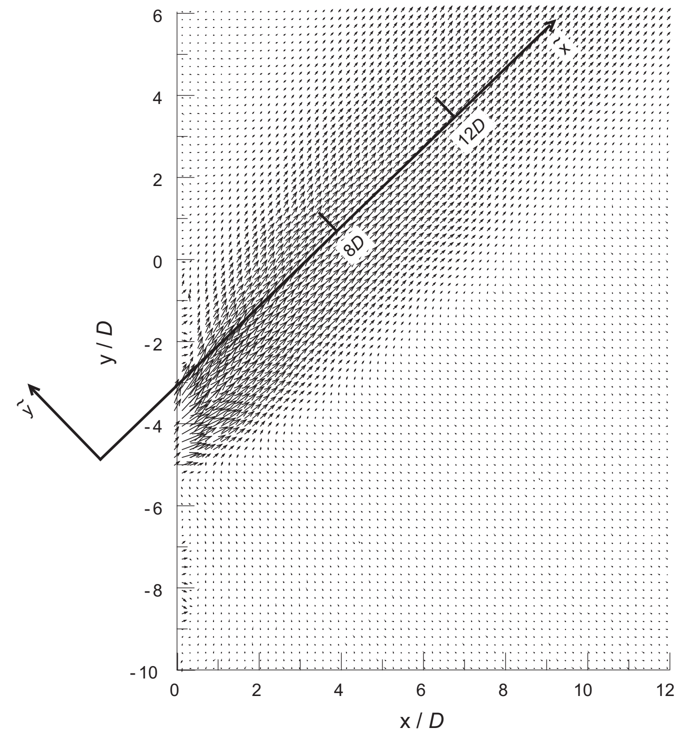

Fig. 3.6: Velocity vector field for circumferential percentage of 29.5%, $a/D = 2.00$, and $J^* = 0.769$. The coordinate system $(\tilde{x}, \tilde{y})$ is also shown.

The resultant vector was taken to be the vector angle of the jet. Thus, an initial angle guess was made, then improved by the momentum vector. The vector angle for the case in Fig. 3.6 was found to be $\Phi = 49°$.

The vectored jet area, width, height, and growth rate were examined using stereo PIV data. Data was collected at $\tilde{x} = 8D$ and at $\tilde{x} = 12D$ for three-component tests listed in Table 3.1. For each geometric setup and jet momentum flux ratio, 300 PIV images were acquired simultaneously by the two cameras at 5 Hz. LaVision DaVis software was used to generate averaged three-component velocity vector fields from these images. A low-level code was used to detect the cross-sectional width and height of the jet profile at half the maximum velocity based on the averaged velocity vector fields. It was observed that the jet cross-sectional profile was elliptical, so the cross-sectional areas of the jets were found fitting the equation for an ellipse using the measured width and height.

3.5 Uncertainty Analysis

The uncertainty in the momentum flux ratio arises from the uncertainties in the exit slot areas due to machining errors and the uncertainty of the mass flow controllers used throughout the experiments. Since density cancels in Eq. 3.1, the uncertainty in the momentum flux ratio is found according to

$$U_{J^*}^2 = U_{A_c}^2 \left(\frac{\partial J^*}{\partial A_c}\right)^2 + U_{A_p}^2 \left(\frac{\partial J^*}{\partial A_p}\right)^2 + U_{\dot{m}_c}^2 \left(\frac{\partial J^*}{\partial \dot{m}_c}\right)^2 + U_{\dot{m}_p}^2 \left(\frac{\partial J^*}{\partial \dot{m}_p}\right)^2 . \tag{3.2}$$

Calculating the partial derivatives in Eq. 3.2 and simplifying, the uncertainty equation becomes

$$U_{J^*} = J^* \sqrt{\left(\frac{U_{A_c}}{A_c}\right)^2 + \left(\frac{U_{A_p}}{A_p}\right)^2 + 4\left(\frac{U_{\dot{m}_c}}{\dot{m}_c}\right)^2 + 4\left(\frac{U_{\dot{m}_p}}{\dot{m}_p}\right)^2} . \tag{3.3}$$

Since the control slot area was varied, the uncertainties in the control slot areas range from 3 to 5%, while the primary slot area has an uncertainty of 0.02%. At most, the area uncertainties account for less than 10% of the total uncertainty. The majority of uncertainty comes from the primary and control mass flow rates which are 1.5% full scale. As the accuracy was based on full scale percentages, the uncertainty for those flow ratios on the lower end of the operating range are substantial and plots of the data show error bars to indicate this uncertainty.

Chapter 4

Results

The results are presented in the following manner. First, the jet impingement results are described as these results led to the design of the secondary exit slot study. These results are followed by a discussion on the momentum ratio effects on CSM control. Then, the results of the exit slot size tests will be shown. The velocity profiles are then discussed. The final section involves the results of the three-component PIV tests showing relationships of jet area and aspect ratio.

4.1 Jet Impingement

Three variations of jet impingement location were used and the resulting vector angles are shown in Fig. 4.1. As shown, the tangential location ($a/D = 0.00$) shows very little vectoring. The location one diameter upstream ($a/D = 1.00$) improves vectoring angle, while the greatest vectoring is achieved at $a/D = 2.00$. Although $a/D = 2.00$ gives the largest vectoring angle, the area of the jet increases much more in this case. This may be caused by the secondary and primary jets expanding radially around the curved surface prior to the center of the collar. Thus, a happy medium is found using the $a/D = 1.00$ or one diameter upstream of the center of the collar.

4.2 Momentum Ratio and Control Slot Size

The vectoring performance in terms of vector angle as a function of the momentum flux ratio for various collar radii and control slot sizes is shown in Fig. 4.2. The vectoring angle of the primary jet is a strong function of the non-dimensional momentum flux ratio. The angle is zero with no control flow and generally increases with momentum ratio to a maximum before decreasing gradually. Mason and Crowther [5], in their planar geometry experiment

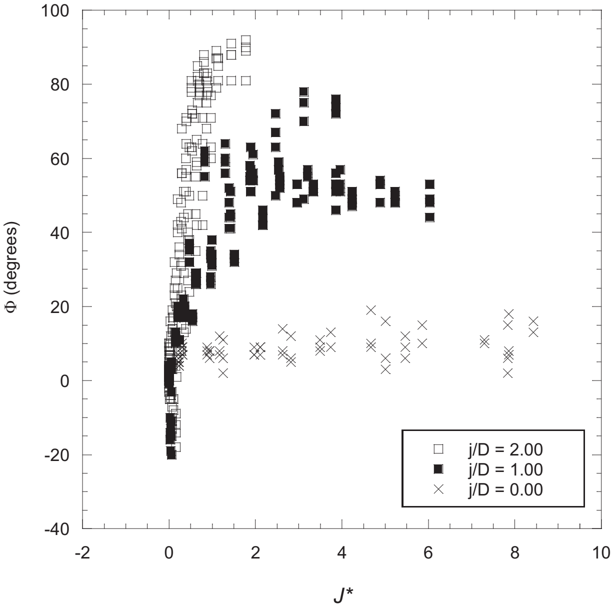

Fig. 4.1: Vector angle as a function of momentum flux ratio for three jet impingement locations. Secondary exit slots are not same as used in exit slot study shown later ($2.00 < a/D < 5.25$ and $0.032 < A_c/A_p < 0.259$).

similar to this, found a similar trend. Mason and Crowther also experienced the "reverse Coanda effect" found at very low momentum ratios in which the primary jet actually vectors toward the opposite curved wall. This is shown in the figure by the negative angles present at very small momentum ratio values.

Also shown in the plots is the effect of the radius of the collar. The Vector angle increases proportional to the radius size. The effect is substantial for the smaller control slots, while the effect of radius is negligible in the largest control slot. Insensitivity to the collar radius will be advantageous in situations where one desires to vector the flow along a radius that will allow dense particulate to remain inside the vectored flow. The area of the control slot also strongly influences the peak and minimum angles, with 29.5% providing the best performance among the values tested.

For each slot size, beyond the flux ratios that resulted in negative angles, the angle increases to a peak value. This behavior is generally linear and the initial slope of these curves is larger for the larger control slots. This can be seen more clearly by examining

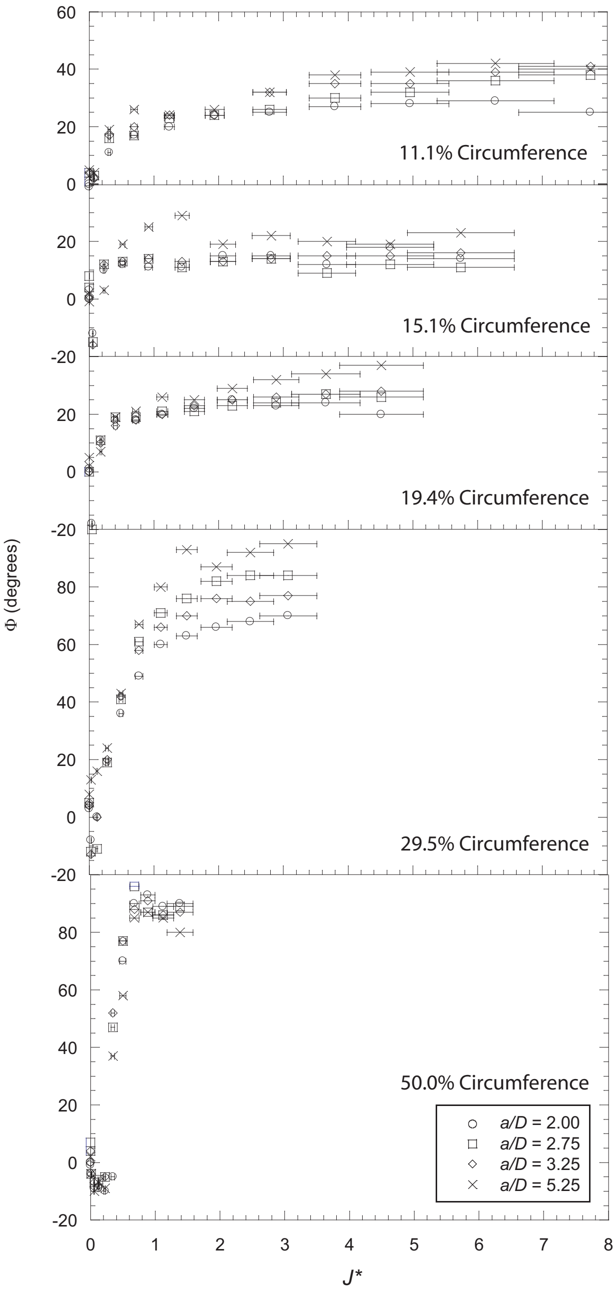

Fig. 4.2: Vector angle as a function of momentum flux ratio for several values of collar radius and control slot size.

the momentum ratio necessary to achieve 90% of the maximum angle for each control slot. As shown in Fig. 4.3, the momentum ratios corresponding to the maximum angles become smaller with the size of the control slot. This plot also shows the large sensitivity to collar radius for small control slots and the insensitivity of the vectoring to collar radius for larger control slots. For each slot size, after the initial drop in angle with momentum ratio, the angle increases to a peak value. This rise is linear and the slope is affected by slot size. The slope of the angle over momentum ratio in this area was calculated for each slot size. The slope as a function of slot size is shown in Fig. 4.4.

The data as plotted shows an exponential correlation. An exponential curve is fit to the data in the graph and fits the original data very well. Although Mason and Crowther [5] did not have an analogous parameter of the control slot circumference to compare to the slope of the linear region, they did mention a similar "control region" where the vectoring may be effectively controlled according to momentum flux ratio.

A correlation function was sought which would enable the accurate prediction of vector angle for given momentum ratios, collar radius, and exit slot circumference percentage.

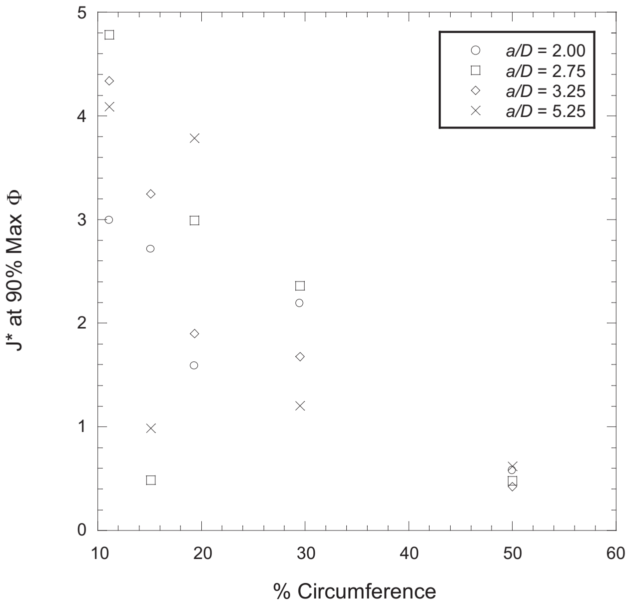

Fig. 4.3: Momentum ratio at 90% of maximum angle as a function of slot size.

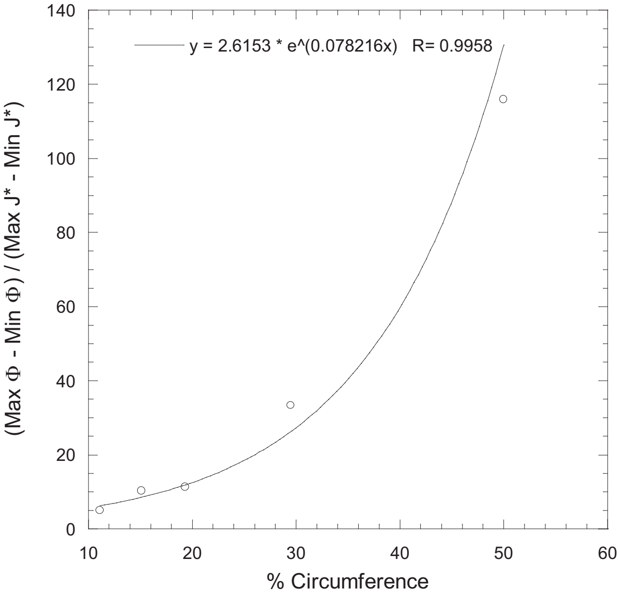

Fig. 4.4: Slope of angle over momentum ratio in the rising angle regime as a function of slot size with exponential curve fit shown (R is a correlation coefficient indicating how well the exponential curve fits the data, closeness to unity indicates a good fit).

Newman [3] described the form of a function that would predict the separation angle (angle at which the jet detaches from the curved surface) of a single jet over a Coanda surface to be

$$\Phi_{sep} = f[\{\frac{(P - p_\infty)ba}{\rho\nu^2}\}^{1/2}] \ , \tag{4.1}$$

with $P - p_\infty$ being pressure differential (where P is the supply pressure) and b as the exit slot width and a is the radius. Using this angle function as a guide, our correlation function incorporates momentum ratio rather than pressure difference as the driving force. Based on the results in Figs. 4.2-4.3, it was determined to scale the results on the control slot size and good agreement is found using

$$\Phi = \left(C1 \times J^* \times \frac{a}{D}\right)^{\left(\frac{\lambda}{C2}\right)} \ , \tag{4.2}$$

where λ is the control slot circumference divided by the primary slot circumference. The constants, $C1$ and $C2$, have values of 3.25 and 2.0, respectively. The results of this correlation function are shown in Fig. 4.5, with various geometries specified. Not only does the data collapse individually for each slot geometry, but the data also collapses generally across slot geometries. The two slot geometries with somewhat dissimilar behavior are those with slots that are 15.1% and 19.4% of the circumference.

4.3 Velocity Profile

With the relationship between the geometry, momentum ratio, and the resultant vectoring angle established, we turn our attention to the impact that this vectoring scheme has on the mixing of the jet. The velocity profile and half-maximum width of the vectored jet at $\tilde{x} = 8D$ downstream of the primary jet exit were examined using two-dimensional PIV. Two baseline measurements were taken for each geometry, one with zero control blowing and primary mass flow rate of 0.004 kg/s (Re = 20,400) and another with zero control blowing and primary mass flow rate of 0.011 kg/s (Re = 61,300). These baseline profiles were compared with vectored jet profiles having the same primary mass flow rate. The average baseline vector angle is 2.63°, apparently due to small variations in the machining.

A comparison of vectored and unvectored cross-stream profiles of the streamwise

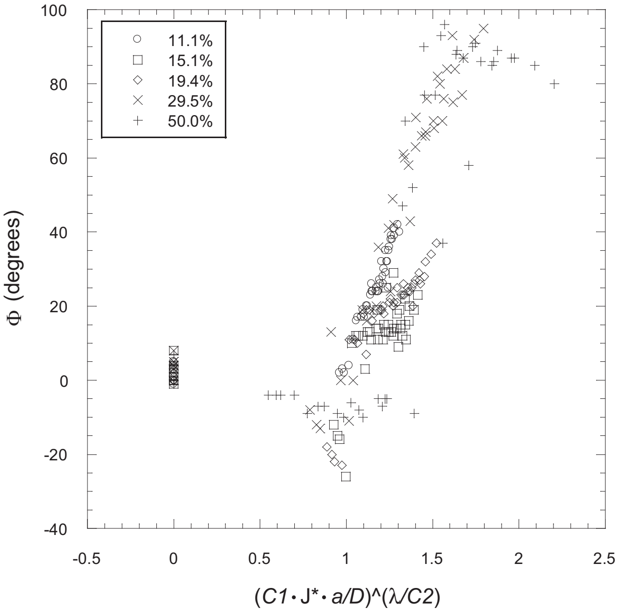

Fig. 4.5: Vector angle as a function of correlation formula including all test data, outlined according to slot size.

component of velocity is shown in Fig. 4.6. Profiles for vectored and unvectored (secondary velocity $u_s = 0$) jets of the same initial primary velocity are more similar for higher primary velocity. Both the vectored and unvectored profiles have maximum velocities occurring at or near $\tilde{y}/D = 0$, and the profiles are nearly symmetric about the centerline. For the lower initial primary velocity, the profile shapes of the vectored jets are widened by the control flow, the maximum velocities occur away from the centerline of the vector angle (and on the side away from the collar), and the profiles are no longer symmetric. These trends were found to be consistent over the entire range of geometries tested. This suggests a smaller change in jet profile with higher primary velocities, regardless of secondary exit slot or collar geometry.

To examine the jet spreading, and thus the mixing, the maximum half-widths were calculated for each of the experiments and the percent difference of the vectored to unvectored maximum half-widths was calculated. The average percent difference for the lower velocity jets was found to be 19.6%, while the higher velocity jets were more similar with an average percent difference of 9.5%. The profile shape changes with increasing momentum flux ratio

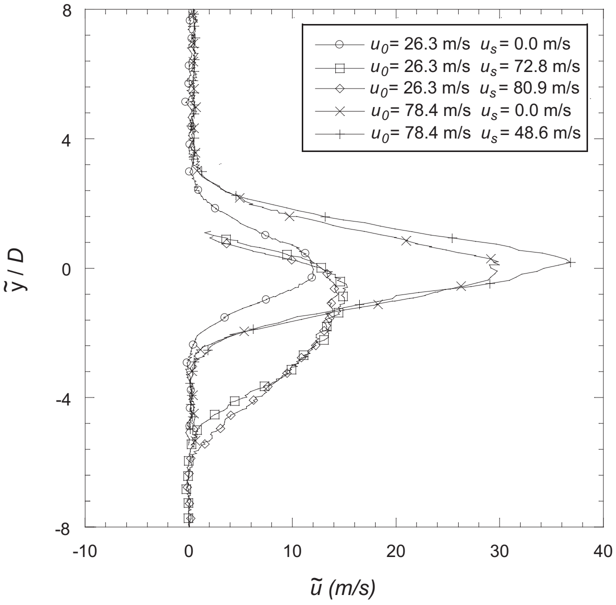

Fig. 4.6: Velocity profiles at $\tilde{x} = 8D$ for 29.50% circumference slot and $a/D = 2.00$ comparing unvectored jets with vectored jets.

as shown in Fig. 4.7. The maximum half-width (indicated by the dashed lines), normalized by D, ranges from 2.25 for no blowing to 4.32 for the largest flow ratio ($J_c = J_p = 3.08$). Also, the maximum velocity location shifts from near the centerline to below the centerline or away from the curved surface adjacent to the control slot. At the same time, the shape also becomes asymmetric with the maximum velocity tending toward the Coanda (positive y) surface.

4.4 Area and Aspect Ratio

The cross-sectional area of the jet at $8D$ and $12D$ downstream of the exit plane was measured using stereo PIV. Contour plots of one geometric combination and J^* are shown in Fig. 4.8. The control flow was applied to the top of the primary jet in this figure. For this case, the area of the vectored jet is 4.07 times greater than the unvectored jet area.

The areas (based on half-maximum velocity) of vectored jets are compared with unvectored jets in Fig. 4.9 at $8D$ and $12D$, respectively. We find that the cross-sectional area at $8D$ increases linearly for all cases. However, at $12D$ downstream, the area increases linearly only until the saturation angle is reached in each geometric combination. After this point, the area increases dramatically. This trend was consistent throughout all testing parameters.

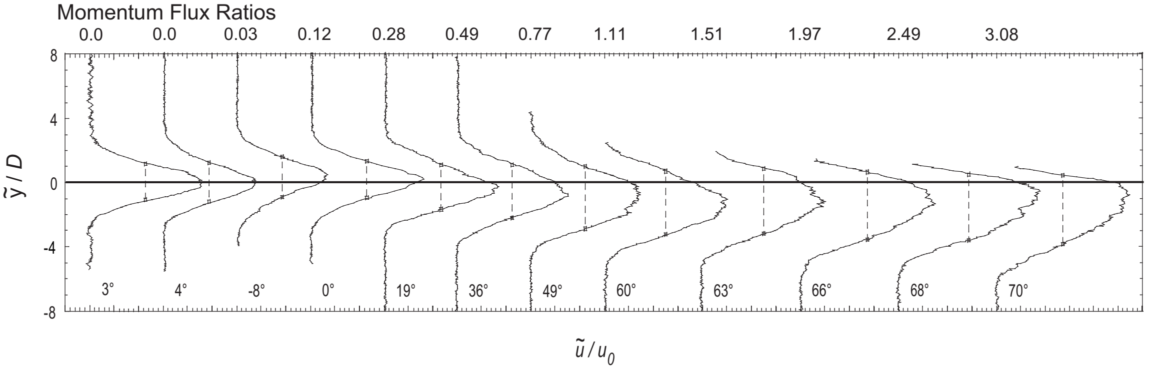

Fig. 4.7: Velocity profiles at $\tilde{x} = 8D$ with increasing momentum flux ratio ($J^* = 0.0$ through 3.08) for 29.50% circumference and $a/D = 2.00$. The maximum half-width and vectored angle for each momentum ratio are also shown.

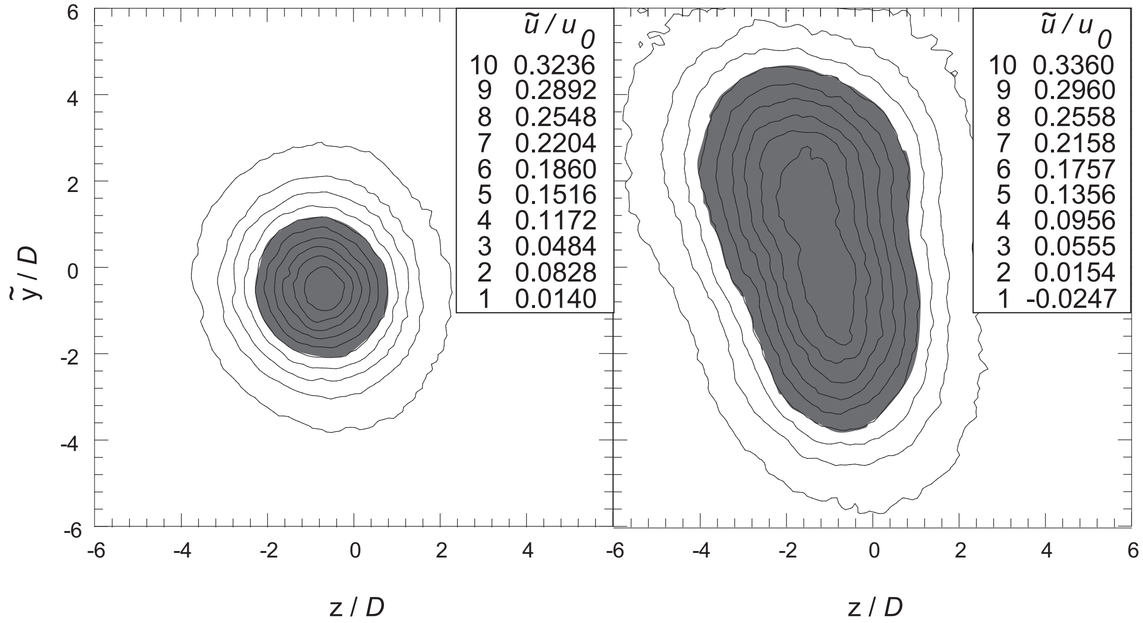

Fig. 4.8: Contour plots of the velocity non-dimensionalized by the exit velocity in a plane normal to the jet at $\tilde{x} = 12D$ for 29.5% circumference and $a/D = 2.00$. The left plot is no vectoring (zero control blowing), while the right plot is with vectoring ($J^* = 2.49$, $\Phi = 70°$). The velocity contours above half the maximum velocity are shaded.

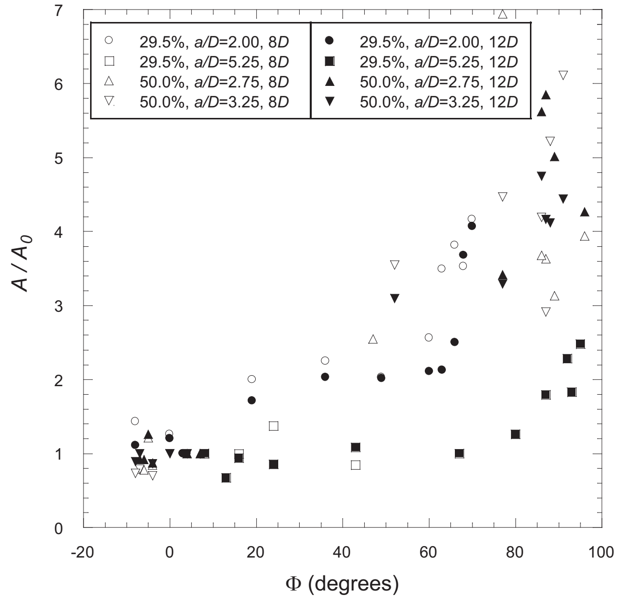

Fig. 4.9: The area of the jet normalized by unvectored jet area at $\tilde{x} = 8D$ and $x = 12D$ as a function of vector angle for various geometries.

Although the normalized areas were different for the two distances downstream, the aspect ratio was not affected by distance downstream as illustrated in Fig. 4.10 where both $8D$ and $12D$ data are plotted. The data is linearly decreasing, or the height increases more rapidly than the width for angles up to 90°. In terms of the CSM geometry, the jet profile is stretching in the $\tilde{y}$-positive direction or towards the control slot. After this point the width increases extremely fast with increasing angle. In other words, the jet spreads more rapidly across the Coanda surface as vector angle is increased past $\Phi = 90°$.

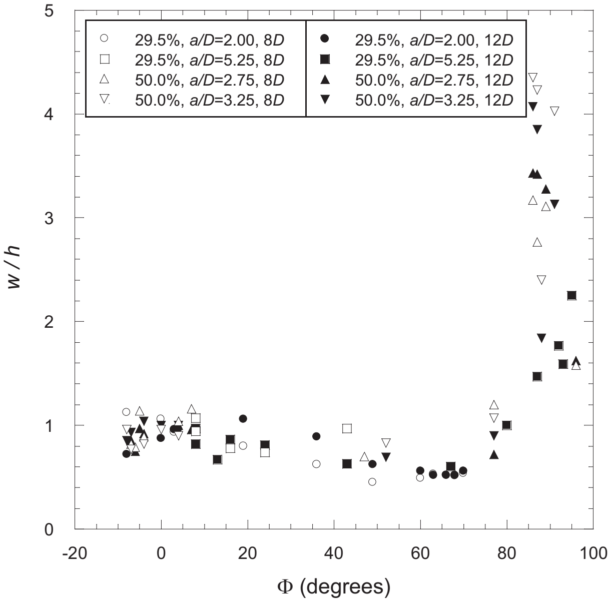

Fig. 4.10: Aspect ratio of the vectored jets at both $\tilde{x} = 8D$ and $\tilde{x} = 12D$ for various geometries as a function of vector angle.

Chapter 5

Conclusions and Future Work

A fluidic jet-vectoring scheme termed “Coanda-assisted Vectoring” is demonstrated on an axisymmetric geometry. For the parameter space including $20,000 < \mathrm{Re} < 80,000$ and Mach< 0.3, the vectoring performance of twenty-eight geometric combinations was examined. The control/primary momentum flux ratio was varied in the range from 0.00 to 7.75. It was found that the jet impingement location that maximized vector angle and minimized jet spreading was one diameter upstream of the collar center. The maximum vector angle was found to be 96°. The fundamental behavior of the vectoring angle with momentum flux ratio was similar for all values tested: for very small momentum ratios, negative vectoring was observed; after vectoring in the positive direction (toward the control flow), the vectoring angle increased nearly linearly with momentum ratio to a peak value; then angle decreased gradually with increasing momentum ratio. The control jet exit slot area was found to have a strong effect on the maximum angle and the momentum ratios required to achieve the maximum vectoring angle. The slope of the linear portion of the vectoring angle as a function of momentum ratio increased with slot size. The vectoring angle was found to increase with collar radius, with greater increase for smaller slots. A correlation function was shown to describe the complete set of data well.

The velocity profiles for vectored and unvectored jets were similar in shape for high velocity cases. For lower velocities, vectoring caused the maximum velocity to shift away from the Coanda surface and the velocity profile to widen. The profile became increasingly asymmetric with momentum flux ratio.

Vectored flow cross-sectional area increased proportional to vector angle at $8D$, while saturation angle caused rapid growth in area at $12D$ downstream of the primary jet exit. The aspect ratio remains constant until $\Phi = 90°$, afterwhich the width of the jet increases dramatically.

The goal of this work has been to gain insight into the control of the CSM. Using the results shown, it is recommended that the prototype CSM be redesigned to incorporate the optimum jet impingement location, secondary slot size, and radius of curvature ($j/D = 1.00$, 29.5% circumference, $a/D = 2.75$). Also, the information on momentum ratio in the linear or control region should also be used. Recommended further work includes a time resolved PIV study of rotational characteristics of the vectored jet.

References

[1] Davis, J. R., editor, *Handbook of Thermal Spray Technology*, ASM International, Materials Park, OH, 2004.

[2] Kodas, T. T., and Hampden-Smith, M. J., *Aerosol Processing of Materials*, Wiley-VCH, New York, 1999.

[3] Newman, B. G., "The Deflexion of Plane Jets by Adjacent Boundaries– Coanda Effect," *Boundary Layer and Flow Control*, edited by G. V. Lachmann, Vol. 1, Pergamon Press, Oxford, 1961, pp. 232–264.

[4] Schlichting, H., *Boundary-Layer Theory*, McGraw Hill, New York, 1968.

[5] Mason, M. S., and Crowther, W. J., "Fluidic Thrust Vectoring of Low Observable Aircraft," CEAS Aerospace Aerodynamic Research Conference, June 2002.

[6] Smith, B. L., and Glezer, A., "Jet Vectoring Using Synthetic Jets," *Journal of Fluid Mechanics*, Vol. 458, 2002, pp. 1–34.

[7] Bettridge, M. W., Spall, R. E., and Smith, B. L., "Aerodynamic Jet Steering Using Steady Blowing and Suction," *Experiments in Fluids*, Vol. 40, No. 5, 2006, pp. 776–785.

[8] Hammond, D. A., and Redekopp, L. G., "Global Dynamics and Aerodynamic Flow Vectoring of Wakes," *Journal of Fluid Mechanics*, Vol. 338, 1997, pp. 231–248.

[9] Pack, L. G., and Seifert, A., "Periodic Excitation for Jet Vectoring and Enhanced Spreading," *Journal of Aircraft*, Vol. 38, 2001, pp. 486–495.

[10] Strykowski, P. J., Krothapalli, A., and Forliti, D. J., "Counterflow Thrust Vectoring," *AIAA Journal*, Vol. 34, No. 11, 1996, pp. 2306–2314.

[11] Strock, E., Ruggiero, P., and Reynolds, D., "The Effect of Off-Angle Spraying on the Structure and Properties of HVOF WC/CoCr Coatings," *Proceedings of the International Thermal Spray Conference*, 2001, pp. 671–676.

[12] Joyce, J. W., "Fluidics: Basic Components and Applications," Tech. Rept. HDL-SR-83-9, Harry Diamond Laboratories, Adelphi, MD, 1983.

[13] Wille, R., and Fernholz, H., "Report on the First European Mechanics Colloquium," *Journal of Fluid Mechanics*, Vol. 23, 1965, pp. 801–819.

[14] Rask, R. B., *An Experimental Study of Two-Dimensional and Three-Dimensional Curved Wall Jets*, Ph.D. thesis, University of Minnesota, 1973.

[15] Patankar, U. M., and Sridhar, K., "Three-Dimensional Curved Wall Jets," *Journal of Basic Engineering (changed to Journal of Engineering Materials and Technology; and the Journal of Fluids Engineering)*, Vol. 94, No. 2, 1972, pp. 339–344.

[16] Bradshaw, P., "Effects of Streamline Curvature on Turbulent Flow," *AGARDograph*, 1990, AGARDograph AG-169.

[17] Carpenter, P. W., and Green, P. N., "The Aeroacoustics and Aerodynamics of High-Speed Coanda Devices, Part 1: Conventional Arrangement of Exit Nozzle and Surface," *Journal of Sound and Vibration*, Vol. 208, No. 5, 1997, pp. 777–801.

[18] Fekete, G. I., "Coanda Flow of a Two-Dimensional Wall Jet on the Outside of a Circular Cylinder," Tech. Rept. 63-11, Mechanical Engineering Research Laboratories, McGill University, 1963.

[19] Gregory-Smith, D. G., and Gilchrist, A. R., "The Compressible Coanda Wall Jet - an Experimental Study of Jet Structure and Breakaway," *International Journal of Heat and Fluid Flow*, Vol. 8, No. 2, 1987, pp. 156–164.

[20] Juvet, P. J. D., *Control of High Reynolds Number Round Jets*, Ph.D. thesis, Department of Mechanical Engineering, Stanford University, 1993.

[21] Giles, J. A., Hays, A. P., and Sawyer, R. A., "Turbulent Wall Jets on Logarithmic Spiral Surfaces," *The Aeronautical Quarterly*, 1966, pp. 201–215.

[22] Wilson, D. J., and Goldstein, R. J., "Turbulent Wall Jets with Cylindrical Streamwise Surface Curvature," *Journal of Fluids Engineering*, 1976, pp. 550–557.

[23] Guitton, D. E., and Newman, B. G., "Self-Preserving Turbulent Wall Jets over Convex Surfaces," *Journal of Fluid Mechanics*, Vol. 81, No. 1, 1977, pp. 155–185.

[24] Newman, B. G., "The Prediction of Turbulent Jets and Wall Jets," *Canadian Aeronautics and Space Journal*, Vol. 15, 1969, pp. 287–305.

[25] Panitz, T., and Wasan, D. T., "Flow Attachment to Solid Surfaces: The Coanda Effect," *AIChE*, Vol. 18, No. 1, 1972, pp. 51–57.

[26] Alcaraz, E., Charnay, G., and Mathieu, J., "Measurements in a Wall Jet over a Convex Surface," *The Physics of Fluids*, Vol. 20, No. 2, 1977, pp. 203–211.

[27] Moser, R. D., "The Effects of Curvature in Wall-Bounded Turbulent Flows," *Journal of Fluid Mechanics*, Vol. 175, 1987, pp. 479–510.

[28] Neuendorf, R., and Wygnanski, I., "On a Turbulent Wall Jet Flowing over a Circular Cylinder," *Journal of Fluid Mechanics*, Vol. 381, 1999, pp. 1–25.

[29] Bevilaqua, P. M., and Lee, J. D., "Design of Supersonic Coanda Jet Nozzles," Proceedings of the Circulation-Control Workshop 1986, 1986.

[30] Gilchrist, A. R., and Gregory-Smith, D. G., "Compressible Coanda Wall Jet - Predictions of Jet Structure and Comparison with Experiment," *International Journal of Heat and Fluid Flow*, Vol. 9, No. 3, 1988, pp. 286–295.

[31] Gregory-Smith, D. G., and Hawkins, M. J., "The Development of an Axisymmetric Curved Turbulent Wall Jet," *International Journal of Heat and Fluid Flow*, Vol. 12, No. 4, 1991, pp. 323–330.

[32] Gregory-Smith, D. G., and Senior, P., “The Effects of Base Steps and Axisymmetry on Supersonic Jets over Coanda Surfaces,” *International Journal of Heat and Fluid Flow*, Vol. 15, No. 4, 1994, pp. 291–298.

[33] Senior, P., *The Aerodynamics of Curved Wall Jets and Breakaway in Coanda Flares*, Ph.D. thesis, University of Durham, UK, 1991.

[34] Cornelius, K. C., and Lucius, G. A., “Physics of Coanda Detachment at High-Pressure Ratio,” *Journal of Aircraft*, Vol. 31, No. 3, 1994, pp. 591–596.

[35] Carpenter, P. W., and Smith, C., “The Aeroacoustics and Aerodynamics of High-Speed Coanda Devices, part 2: Effects of Modifications for Flow Control and Noise Reduction,” *Journal of Sound and Vibration*, Vol. 208, No. 5, 1997, pp. 803–822.

[36] Wing, D. J., “Static Investigation of Two Fluidic Thrust-Vectoring Concepts on a Two-Dimensional Convergent-Divergent Nozzle,” Tech. Rept. NASA TM-4574, Hampton, VA, 1994.

[37] Parks, E. K., and Petersen, R. E., “Analysis of a Coanda Type Flow,” *AIAA Journal*, Vol. 6, No. 1, 1968, pp. 4–7.

[38] Sawada, K., and Asami, K., “Numerical Study on the Underexpanded Coanda Jet,” *Journal of Aircraft*, Vol. 34, No. 5, 1997, pp. 641–647.

[39] Wernz, S., and Fasel, H. F., “Numerical Investigation of Transition Mechanisms Influencing the Development of Turbulent Wall Jets,” *Collection of Technical Papers - 36th AIAA Fluid Dynamics Conference*, Vol. 4, 2006, pp. 2442 – 2457.

[40] Lin, Y. F., and Sheu, M. J., “Investigation of Two Plane Parallel Unventilated Jets,” *Experiments in Fluids*, Vol. 10, 1990, pp. 17–22.

[41] Bunderson, N., and Smith, B. L., “Passive Mixing Control of Plane Parallel Jets,” *Experiments in Fluids*, Vol. 39, 2005, pp. 66–74.

[42] Anderson, E. A., Snyder, D. O., and Christensen, J., “Periodic Flow Between Low Aspect Ratio Parallel Jets,” *ASME Journal of Fluids Engineering*, Vol. 125, 2003, pp. 389–392.

[43] Fujisawa, N., Nakamura, K., and Srinivas, K., “Interaction of Two Parallel Plane Jets of Different Velocities,” *Journal of Visualization*, Vol. 7, No. 2, 2004, pp. 135–142.

[44] Englar, R. J., “Circulation Control Pneumatic Aerodynamics: Blown Force and Moment Augmentation and Modification; Past, Present, and Future,” AIAA, 2000, Paper 2000-2541.

[45] Warren, R. W., “Some Parameters Affecting the Design of Bistable Fluid Amplifiers,” *ASME Symposium of Fluid Jet Control Devices*, Nov. 1962, pp. 75–82.

[46] Dewald, C. L., Swift, T. L., and Beisel, V. A., “The Woodward Chaffy Seed Conditioner 2000,” *Applied Engineering In Agriculture*, Vol. 19, No. 2, 2003, pp. 219–223.

[47] Nex Flow, *Nex Flow Air Amplifier*, `http://www.nexflowtech.com/pdf_nex_flow/air_amplifier.pdf`.

[48] Fujisawa, N., and Kobayashi, R., "Turbulence Characteristics of Wall Jets along Strong Convex Surfaces," *International Journal of Mechanical Sciences*, Vol. 29, No. 5, 1987, pp. 311–320.

Appendices

Appendix A

Test Data Tables

A.1 Test Parameters of Jet Impingement Study

Run	J*	A_c/A_p	*a/D*	*j/D*	Φ
1	0.00	0.19	2.00	1.00	2
2	0.00	0.19	2.00	1.00	2
3	0.05	0.19	2.00	1.00	6
4	0.21	0.19	2.00	1.00	19
5	0.47	0.19	2.00	1.00	35
6	0.84	0.19	2.00	1.00	58
7	1.31	0.19	2.00	1.00	67
8	1.88	0.19	2.00	1.00	63
9	2.56	0.19	2.00	1.00	59
10	3.35	0.19	2.00	1.00	56
11	4.23	0.19	2.00	1.00	52
12	5.23	0.19	2.00	1.00	52
13	0.00	0.19	2.75	1.00	3
14	0.00	0.19	2.75	1.00	2
15	0.05	0.19	2.75	1.00	7
16	0.21	0.19	2.75	1.00	21
17	0.47	0.19	2.75	1.00	39
18	0.84	0.19	2.75	1.00	63
19	1.31	0.19	2.75	1.00	64
20	1.88	0.19	2.75	1.00	60
21	2.56	0.19	2.75	1.00	57
22	3.35	0.19	2.75	1.00	56
23	4.23	0.19	2.75	1.00	53
24	5.23	0.19	2.75	1.00	53
25	0.00	0.19	3.25	1.00	3
26	0.00	0.19	3.25	1.00	2
27	0.05	0.19	3.25	1.00	7
28	0.21	0.19	3.25	1.00	23
29	0.47	0.19	3.25	1.00	43
30	0.84	0.19	3.25	1.00	65
31	1.31	0.19	3.25	1.00	61
32	1.88	0.19	3.25	1.00	59
33	2.56	0.19	3.25	1.00	57
34	3.35	0.19	3.25	1.00	55
35	4.23	0.19	3.25	1.00	53
36	5.23	0.19	3.25	1.00	53
37	0.00	0.19	5.25	1.00	2
38	0.00	0.19	5.25	1.00	4
39	0.05	0.19	5.25	1.00	4
40	0.21	0.19	5.25	1.00	20
41	0.47	0.19	5.25	1.00	37
42	0.84	0.19	5.25	1.00	59
43	1.31	0.19	5.25	1.00	63
44	1.88	0.19	5.25	1.00	58
45	2.56	0.19	5.25	1.00	58
46	3.35	0.19	5.25	1.00	56
47	4.23	0.19	5.25	1.00	55
48	5.23	0.19	5.25	1.00	55
49	0.00	0.25	2.00	1.00	1
50	0.00	0.25	2.00	1.00	1
51	0.04	0.25	2.00	1.00	-14
52	0.16	0.25	2.00	1.00	11
53	0.36	0.25	2.00	1.00	19
54	0.63	0.25	2.00	1.00	28
55	0.99	0.25	2.00	1.00	33
56	1.43	0.25	2.00	1.00	44
57	1.94	0.25	2.00	1.00	55
58	2.54	0.25	2.00	1.00	60
59	3.21	0.25	2.00	1.00	59
60	3.96	0.25	2.00	1.00	59
61	0.00	0.25	2.75	1.00	4
62	0.00	0.25	2.75	1.00	0
63	0.04	0.25	2.75	1.00	-16
64	0.16	0.25	2.75	1.00	12
65	0.36	0.25	2.75	1.00	21
66	0.63	0.25	2.75	1.00	30
67	0.99	0.25	2.75	1.00	36
68	1.43	0.25	2.75	1.00	48
69	1.94	0.25	2.75	1.00	56
70	2.54	0.25	2.75	1.00	60
71	3.21	0.25	2.75	1.00	59
72	3.96	0.25	2.75	1.00	57
73	0.00	0.25	3.25	1.00	3
74	0.00	0.25	3.25	1.00	-1
75	0.04	0.25	3.25	1.00	-18
76	0.16	0.25	3.25	1.00	13
77	0.36	0.25	3.25	1.00	22
78	0.63	0.25	3.25	1.00	30
79	0.99	0.25	3.25	1.00	42
80	1.43	0.25	3.25	1.00	54
81	1.94	0.25	3.25	1.00	62
82	2.54	0.25	3.25	1.00	60
83	3.21	0.25	3.25	1.00	59
84	3.96	0.25	3.25	1.00	57
85	0.00	0.25	5.25	1.00	4
86	0.00	0.25	5.25	1.00	4
87	0.04	0.25	5.25	1.00	-24
88	0.16	0.25	5.25	1.00	13

Run	J*	A_c/A_p	*a/D*	*j/D*	*Φ*
89	0.36	0.25	5.25	1.00	23
90	0.63	0.25	5.25	1.00	33
91	0.99	0.25	5.25	1.00	38
92	1.43	0.25	5.25	1.00	49
93	1.94	0.25	5.25	1.00	57
94	2.54	0.25	5.25	1.00	58
95	3.21	0.25	5.25	1.00	57
96	3.96	0.25	5.25	1.00	56
97	0.00	0.17	2.00	1.00	2
98	0.00	0.17	2.00	1.00	1
99	0.06	0.17	2.00	1.00	-3
100	0.24	0.17	2.00	1.00	13
101	0.54	0.17	2.00	1.00	19
102	0.97	0.17	2.00	1.00	28
103	1.51	0.17	2.00	1.00	34
104	2.17	0.17	2.00	1.00	43
105	2.96	0.17	2.00	1.00	50
106	3.86	0.17	2.00	1.00	53
107	4.89	0.17	2.00	1.00	54
108	6.03	0.17	2.00	1.00	53
109	0.00	0.17	2.75	1.00	4
110	0.00	0.17	2.75	1.00	3
111	0.06	0.17	2.75	1.00	-14
112	0.24	0.17	2.75	1.00	13
113	0.54	0.17	2.75	1.00	19
114	0.97	0.17	2.75	1.00	28
115	1.51	0.17	2.75	1.00	35
116	2.17	0.17	2.75	1.00	46
117	2.96	0.17	2.75	1.00	53
118	3.86	0.17	2.75	1.00	53
119	4.89	0.17	2.75	1.00	53
120	6.03	0.17	2.75	1.00	51
121	0.00	0.17	3.25	1.00	0
122	0.00	0.17	3.25	1.00	0
123	0.06	0.17	3.25	1.00	-18
124	0.24	0.17	3.25	1.00	13
125	0.54	0.17	3.25	1.00	19
126	0.97	0.17	3.25	1.00	29
127	1.51	0.17	3.25	1.00	35
128	2.17	0.17	3.25	1.00	46
129	2.96	0.17	3.25	1.00	51
130	3.86	0.17	3.25	1.00	52
131	4.89	0.17	3.25	1.00	49
132	6.03	0.17	3.25	1.00	48
133	0.00	0.17	5.25	1.00	1
134	0.00	0.17	5.25	1.00	2
135	0.06	0.17	5.25	1.00	-22
136	0.24	0.17	5.25	1.00	13
137	0.54	0.17	5.25	1.00	21
138	0.97	0.17	5.25	1.00	30
139	1.51	0.17	5.25	1.00	36
140	2.17	0.17	5.25	1.00	46
141	2.96	0.17	5.25	1.00	49
142	3.86	0.17	5.25	1.00	55
143	4.89	0.17	5.25	1.00	54
144	6.03	0.17	5.25	1.00	50
145	0.00	0.26	2.00	1.00	1
146	0.00	0.26	2.00	1.00	1
147	0.04	0.26	2.00	1.00	-12
148	0.15	0.26	2.00	1.00	13
149	0.35	0.26	2.00	1.00	23
150	0.62	0.26	2.00	1.00	32
151	0.97	0.26	2.00	1.00	38
152	1.39	0.26	2.00	1.00	42
153	1.89	0.26	2.00	1.00	52
154	2.47	0.26	2.00	1.00	64
155	3.13	0.26	2.00	1.00	69
156	3.86	0.26	2.00	1.00	74
157	0.00	0.26	2.75	1.00	2
158	0.00	0.26	2.75	1.00	1
159	0.04	0.26	2.75	1.00	-17
160	0.15	0.26	2.75	1.00	14
161	0.35	0.26	2.75	1.00	25
162	0.62	0.26	2.75	1.00	32
163	0.97	0.26	2.75	1.00	38
164	1.39	0.26	2.75	1.00	53
165	1.89	0.26	2.75	1.00	58
166	2.47	0.26	2.75	1.00	66
167	3.13	0.26	2.75	1.00	72
168	3.86	0.26	2.75	1.00	73
169	0.00	0.26	3.25	1.00	1
170	0.00	0.26	3.25	1.00	1
171	0.04	0.26	3.25	1.00	-21
172	0.15	0.26	3.25	1.00	15
173	0.35	0.26	3.25	1.00	23
174	0.62	0.26	3.25	1.00	34
175	0.97	0.26	3.25	1.00	39
176	1.39	0.26	3.25	1.00	51
177	1.89	0.26	3.25	1.00	62
178	2.47	0.26	3.25	1.00	69
179	3.13	0.26	3.25	1.00	71
180	3.86	0.26	3.25	1.00	72
181	0.00	0.26	5.25	1.00	0
182	0.00	0.26	5.25	1.00	4
183	0.04	0.26	5.25	1.00	-18
184	0.15	0.26	5.25	1.00	13
185	0.35	0.26	5.25	1.00	21
186	0.62	0.26	5.25	1.00	31
187	0.97	0.26	5.25	1.00	37
188	1.39	0.26	5.25	1.00	48
189	1.89	0.26	5.25	1.00	54
190	2.47	0.26	5.25	1.00	53
191	3.13	0.26	5.25	1.00	51
192	3.86	0.26	5.25	1.00	50
193	0.00	0.03	2.00	0.00	0
194	0.31	0.03	2.00	0.00	11
195	1.25	0.03	2.00	0.00	13
196	2.82	0.03	2.00	0.00	15
197	5.01	0.03	2.00	0.00	20
198	7.83	0.03	2.00	0.00	19
199	11.28	0.03	2.00	0.00	15
200	15.35	0.03	2.00	0.00	14
201	20.05	0.03	2.00	0.00	11
202	25.37	0.03	2.00	0.00	14
203	31.33	0.03	2.00	0.00	12
204	0.31	0.03	2.75	0.00	8
205	1.25	0.03	2.75	0.00	8
206	2.82	0.03	2.75	0.00	8

Run	J*	A_c/A_p	*a/D*	*j/D*	*Φ*
207	5.01	0.03	2.75	0.00	9
208	7.83	0.03	2.75	0.00	8
209	11.28	0.03	2.75	0.00	4
210	15.35	0.03	2.75	0.00	2
211	20.05	0.03	2.75	0.00	-1
212	25.37	0.03	2.75	0.00	5
213	31.33	0.03	2.75	0.00	4
214	0.00	0.03	3.25	0.00	2
215	0.00	0.03	3.25	0.00	0
216	0.31	0.03	3.25	0.00	9
217	1.25	0.03	3.25	0.00	-7
218	2.82	0.03	3.25	0.00	7
219	5.01	0.03	3.25	0.00	5
220	7.83	0.03	3.25	0.00	3
221	11.28	0.03	3.25	0.00	8
222	15.35	0.03	3.25	0.00	9
223	20.05	0.03	3.25	0.00	12
224	25.37	0.03	3.25	0.00	14
225	31.33	0.03	3.25	0.00	12
226	0.00	0.03	2.00	0.00	1
227	0.29	0.03	2.00	0.00	12
228	1.17	0.03	2.00	0.00	15
229	2.62	0.03	2.00	0.00	17
230	4.67	0.03	2.00	0.00	23
231	23.62	0.03	2.00	0.00	13
232	29.16	0.03	2.00	0.00	12
233	0.00	0.03	2.75	0.00	3
234	0.00	0.03	2.75	0.00	2
235	0.29	0.03	2.75	0.00	9
236	1.17	0.03	2.75	0.00	9
237	2.62	0.03	2.75	0.00	11
238	4.67	0.03	2.75	0.00	14
239	7.29	0.03	2.75	0.00	17
240	10.50	0.03	2.75	0.00	13
241	14.29	0.03	2.75	0.00	16
242	18.66	0.03	2.75	0.00	14
243	23.62	0.03	2.75	0.00	13
244	29.16	0.03	2.75	0.00	11
245	0.00	0.03	3.25	0.00	2
246	0.00	0.03	3.25	0.00	2
247	0.29	0.03	3.25	0.00	11
248	1.17	0.03	3.25	0.00	11
249	2.62	0.03	3.25	0.00	10
250	4.67	0.03	3.25	0.00	14
251	7.29	0.03	3.25	0.00	15
252	10.50	0.03	3.25	0.00	11
253	14.29	0.03	3.25	0.00	12
254	18.66	0.03	3.25	0.00	14
255	23.62	0.03	3.25	0.00	16
256	29.16	0.03	3.25	0.00	14
257	0.00	0.04	2.00	0.00	0
258	0.23	0.04	2.00	0.00	5
259	0.94	0.04	2.00	0.00	8
260	2.11	0.04	2.00	0.00	9
261	3.75	0.04	2.00	0.00	11
262	5.85	0.04	2.00	0.00	13
263	8.43	0.04	2.00	0.00	15
264	11.47	0.04	2.00	0.00	21
265	14.99	0.04	2.00	0.00	22
266	18.97	0.04	2.00	0.00	19
267	23.42	0.04	2.00	0.00	17
268	0.00	0.04	2.75	0.00	1
269	0.23	0.04	2.75	0.00	6
270	0.94	0.04	2.75	0.00	9
271	2.11	0.04	2.75	0.00	11
272	3.75	0.04	2.75	0.00	14
273	5.85	0.04	2.75	0.00	17
274	8.43	0.04	2.75	0.00	18
275	11.47	0.04	2.75	0.00	20
276	14.99	0.04	2.75	0.00	19
277	18.97	0.04	2.75	0.00	20
278	23.42	0.04	2.75	0.00	19
279	0.00	0.04	3.25	0.00	1
280	0.23	0.04	3.25	0.00	5
281	0.94	0.04	3.25	0.00	9
282	2.11	0.04	3.25	0.00	11
283	18.97	0.04	3.25	0.00	19
284	23.42	0.04	3.25	0.00	17
285	0.00	0.05	2.00	0.00	1
286	0.00	0.05	2.00	0.00	1
287	0.22	0.05	2.00	0.00	7
288	0.87	0.05	2.00	0.00	10
289	1.96	0.05	2.00	0.00	11
290	3.49	0.05	2.00	0.00	12
291	5.46	0.05	2.00	0.00	13
292	7.86	0.05	2.00	0.00	17
293	10.69	0.05	2.00	0.00	18
294	13.96	0.05	2.00	0.00	16
295	17.67	0.05	2.00	0.00	18
296	21.82	0.05	2.00	0.00	17
297	0.00	0.05	2.75	0.00	2
298	0.00	0.05	2.75	0.00	0
299	0.22	0.05	2.75	0.00	8
300	0.87	0.05	2.75	0.00	10
301	1.96	0.05	2.75	0.00	9
302	3.49	0.05	2.75	0.00	11
303	5.46	0.05	2.75	0.00	12
304	7.86	0.05	2.75	0.00	12
305	10.69	0.05	2.75	0.00	13
306	13.96	0.05	2.75	0.00	14
307	17.67	0.05	2.75	0.00	14
308	21.82	0.05	2.75	0.00	14
309	0.00	0.05	3.25	0.00	2
310	0.00	0.05	3.25	0.00	1
311	0.22	0.05	3.25	0.00	7
312	0.87	0.05	3.25	0.00	9
313	1.96	0.05	3.25	0.00	9
314	3.49	0.05	3.25	0.00	11
315	5.46	0.05	3.25	0.00	9
316	7.86	0.05	3.25	0.00	9
317	10.69	0.05	3.25	0.00	14
318	13.96	0.05	3.25	0.00	15
319	17.67	0.05	3.25	0.00	15
320	21.82	0.05	3.25	0.00	17
321	0.00	1.23	2.00	2.00	0
322	0.00	1.23	2.00	2.00	3
323	0.01	1.23	2.00	2.00	3
324	0.03	1.23	2.00	2.00	3

Run	J*	A_c/A_p	*a/D*	*j/D*	*Φ*
325	0.07	1.23	2.00	2.00	3
326	0.13	1.23	2.00	2.00	13
327	0.20	1.23	2.00	2.00	25
328	0.29	1.23	2.00	2.00	41
329	0.40	1.23	2.00	2.00	57
330	0.52	1.23	2.00	2.00	63
331	0.66	1.23	2.00	2.00	75
332	0.81	1.23	2.00	2.00	83
333	0.00	1.23	2.75	2.00	2
334	0.00	1.23	2.75	2.00	3
335	0.01	1.23	2.75	2.00	4
336	0.03	1.23	2.75	2.00	6
337	0.07	1.23	2.75	2.00	13
338	0.13	1.23	2.75	2.00	23
339	0.20	1.23	2.75	2.00	40
340	0.29	1.23	2.75	2.00	56
341	0.40	1.23	2.75	2.00	64
342	0.52	1.23	2.75	2.00	78
343	0.66	1.23	2.75	2.00	81
344	0.81	1.23	2.75	2.00	86
345	0.00	1.23	3.25	2.00	2
346	0.00	1.23	3.25	2.00	3
347	0.01	1.23	3.25	2.00	4
348	0.03	1.23	3.25	2.00	8
349	0.07	1.23	3.25	2.00	14
350	0.13	1.23	3.25	2.00	25
351	0.20	1.23	3.25	2.00	42
352	0.29	1.23	3.25	2.00	56
353	0.40	1.23	3.25	2.00	70
354	0.52	1.23	3.25	2.00	79
355	0.66	1.23	3.25	2.00	85
356	0.81	1.23	3.25	2.00	88
357	0.00	1.23	5.25	2.00	3
358	0.00	1.23	5.25	2.00	3
359	0.01	1.23	5.25	2.00	9
360	0.03	1.23	5.25	2.00	8
361	0.07	1.23	5.25	2.00	19
362	0.13	1.23	5.25	2.00	32
363	0.20	1.23	5.25	2.00	49
364	0.29	1.23	5.25	2.00	68
365	0.40	1.23	5.25	2.00	71
366	0.52	1.23	5.25	2.00	81
367	0.66	1.23	5.25	2.00	82
368	0.81	1.23	5.25	2.00	83
369	0.00	1.03	2.00	2.00	1
370	0.00	1.03	2.00	2.00	1
371	0.01	1.03	2.00	2.00	4
372	0.04	1.03	2.00	2.00	4
373	0.09	1.03	2.00	2.00	4
374	0.15	1.03	2.00	2.00	4
375	0.24	1.03	2.00	2.00	8
376	0.35	1.03	2.00	2.00	13
377	0.47	1.03	2.00	2.00	24
378	0.62	1.03	2.00	2.00	35
379	0.78	1.03	2.00	2.00	42
380	0.96	1.03	2.00	2.00	60
381	0.00	1.03	2.75	2.00	3
382	0.00	1.03	2.75	2.00	3
383	0.01	1.03	2.75	2.00	6
384	0.04	1.03	2.75	2.00	9
385	0.09	1.03	2.75	2.00	10
386	0.15	1.03	2.75	2.00	12
387	0.24	1.03	2.75	2.00	19
388	0.35	1.03	2.75	2.00	29
389	0.47	1.03	2.75	2.00	38
390	0.62	1.03	2.75	2.00	45
391	0.78	1.03	2.75	2.00	50
392	0.96	1.03	2.75	2.00	63
393	0.00	1.03	3.25	2.00	-2
394	0.00	1.03	3.25	2.00	3
395	0.01	1.03	3.25	2.00	6
396	0.04	1.03	3.25	2.00	10
397	0.09	1.03	3.25	2.00	14
398	0.15	1.03	3.25	2.00	21
399	0.24	1.03	3.25	2.00	34
400	0.35	1.03	3.25	2.00	44
401	0.47	1.03	3.25	2.00	50
402	0.62	1.03	3.25	2.00	55
403	0.78	1.03	3.25	2.00	64
404	0.96	1.03	3.25	2.00	71
405	0.00	1.03	5.25	2.00	-3
406	0.00	1.03	5.25	2.00	10
407	0.01	1.03	5.25	2.00	10
408	0.04	1.03	5.25	2.00	16
409	0.09	1.03	5.25	2.00	17
410	0.15	1.03	5.25	2.00	27
411	0.24	1.03	5.25	2.00	36
412	0.35	1.03	5.25	2.00	51
413	0.47	1.03	5.25	2.00	63
414	0.62	1.03	5.25	2.00	71
415	0.78	1.03	5.25	2.00	71
416	0.96	1.03	5.25	2.00	77
417	0.00	0.56	2.00	2.00	0
418	0.00	0.56	2.00	2.00	0
419	0.02	0.56	2.00	2.00	-5
420	0.07	0.56	2.00	2.00	-10
421	0.16	0.56	2.00	2.00	-9
422	0.29	0.56	2.00	2.00	15
423	0.45	0.56	2.00	2.00	27
424	0.64	0.56	2.00	2.00	42
425	0.87	0.56	2.00	2.00	68
426	1.14	0.56	2.00	2.00	85
427	1.44	0.56	2.00	2.00	88
428	1.78	0.56	2.00	2.00	90
429	0.00	0.56	2.75	2.00	0
430	0.00	0.56	2.75	2.00	1
431	0.02	0.56	2.75	2.00	-4
432	0.07	0.56	2.75	2.00	-11
433	0.16	0.56	2.75	2.00	-12
434	0.29	0.56	2.75	2.00	23
435	0.45	0.56	2.75	2.00	38
436	0.64	0.56	2.75	2.00	58
437	0.87	0.56	2.75	2.00	81
438	1.14	0.56	2.75	2.00	87
439	1.44	0.56	2.75	2.00	91
440	1.78	0.56	2.75	2.00	92
441	0.00	0.56	3.25	2.00	4
442	0.00	0.56	3.25	2.00	3

Run	J*	A_c/A_p	*a/D*	*j/D*	*Φ*
443	0.02	0.56	3.25	2.00	-5
444	0.07	0.56	3.25	2.00	-13
445	0.16	0.56	3.25	2.00	-14
446	0.29	0.56	3.25	2.00	22
447	0.45	0.56	3.25	2.00	40
448	0.64	0.56	3.25	2.00	59
449	0.87	0.56	3.25	2.00	77
450	1.14	0.56	3.25	2.00	87
451	1.44	0.56	3.25	2.00	88
452	1.78	0.56	3.25	2.00	89
453	0.00	0.56	5.25	2.00	2
454	0.00	0.56	5.25	2.00	8
455	0.02	0.56	5.25	2.00	7
456	0.07	0.56	5.25	2.00	-7
457	0.16	0.56	5.25	2.00	-18
458	0.29	0.56	5.25	2.00	32
459	0.45	0.56	5.25	2.00	45
460	0.64	0.56	5.25	2.00	65
461	0.87	0.56	5.25	2.00	75
462	1.14	0.56	5.25	2.00	81
463	1.44	0.56	5.25	2.00	81
464	1.78	0.56	5.25	2.00	81
465	0.00	0.92	2.00	2.00	4
466	0.00	0.92	2.00	2.00	1
467	0.01	0.92	2.00	2.00	0
468	0.04	0.92	2.00	2.00	-5
469	0.10	0.92	2.00	2.00	-5
470	0.18	0.92	2.00	2.00	1
471	0.27	0.92	2.00	2.00	8
472	0.39	0.92	2.00	2.00	14
473	0.54	0.92	2.00	2.00	62
474	0.70	0.92	2.00	2.00	77
475	0.88	0.92	2.00	2.00	79
476	1.09	0.92	2.00	2.00	87
477	0.00	0.92	2.75	2.00	4
478	0.00	0.92	2.75	2.00	3
479	0.01	0.92	2.75	2.00	1
480	0.04	0.92	2.75	2.00	-4
481	0.10	0.92	2.75	2.00	-5
482	0.18	0.92	2.75	2.00	6
483	0.27	0.92	2.75	2.00	31
484	0.39	0.92	2.75	2.00	51
485	0.54	0.92	2.75	2.00	72
486	0.70	0.92	2.75	2.00	79
487	0.88	0.92	2.75	2.00	83
488	1.09	0.92	2.75	2.00	89
489	0.00	0.92	3.25	2.00	5
490	0.00	0.92	3.25	2.00	2
491	0.01	0.92	3.25	2.00	3
492	0.04	0.92	3.25	2.00	-4
493	0.10	0.92	3.25	2.00	-8
494	0.18	0.92	3.25	2.00	20
495	0.27	0.92	3.25	2.00	43
496	0.39	0.92	3.25	2.00	55
497	0.54	0.92	3.25	2.00	73
498	0.70	0.92	3.25	2.00	80
499	0.88	0.92	3.25	2.00	82
500	1.09	0.92	3.25	2.00	87
501	0.00	0.92	5.25	2.00	1
502	0.00	0.92	5.25	2.00	9
503	0.01	0.92	5.25	2.00	7
504	0.04	0.92	5.25	2.00	12
505	0.10	0.92	5.25	2.00	17
506	0.18	0.92	5.25	2.00	29
507	0.27	0.92	5.25	2.00	48
508	0.39	0.92	5.25	2.00	60
509	0.54	0.92	5.25	2.00	72
510	0.70	0.92	5.25	2.00	78
511	0.88	0.92	5.25	2.00	78
512	1.09	0.92	5.25	2.00	79

A.2 Test Parameters of Two-Component PIV Study

Run	J^*	% Circ.	*a/D*	*j/D*	Φ
513	0.00	11.1	2.00	1.00	-1
514	0.00	11.1	2.00	1.00	0
515	0.09	11.1	2.00	1.00	2
516	0.35	11.1	2.00	1.00	11
517	0.79	11.1	2.00	1.00	17
518	1.41	11.1	2.00	1.00	20
519	2.20	11.1	2.00	1.00	24
520	3.17	11.1	2.00	1.00	25
521	4.31	11.1	2.00	1.00	27
522	5.63	11.1	2.00	1.00	28
523	7.13	11.1	2.00	1.00	29
524	8.80	11.1	2.00	1.00	25
525	0.00	11.1	2.75	1.00	1
526	0.00	11.1	2.75	1.00	4
527	0.09	11.1	2.75	1.00	3
528	0.35	11.1	2.75	1.00	16
529	0.79	11.1	2.75	1.00	17
530	1.41	11.1	2.75	1.00	23
531	2.20	11.1	2.75	1.00	24
532	3.17	11.1	2.75	1.00	26
533	4.31	11.1	2.75	1.00	30
534	5.63	11.1	2.75	1.00	32
535	7.13	11.1	2.75	1.00	36
536	8.80	11.1	2.75	1.00	38
537	0.00	11.1	3.25	1.00	4
538	0.00	11.1	3.25	1.00	4
539	0.09	11.1	3.25	1.00	2
540	0.35	11.1	3.25	1.00	17
541	0.79	11.1	3.25	1.00	20
542	1.41	11.1	3.25	1.00	24
543	2.20	11.1	3.25	1.00	24
544	3.17	11.1	3.25	1.00	32
545	4.31	11.1	3.25	1.00	35
546	5.63	11.1	3.25	1.00	35
547	7.13	11.1	3.25	1.00	39
548	8.80	11.1	3.25	1.00	41
549	0.00	11.1	5.25	1.00	3
550	0.00	11.1	5.25	1.00	5
551	0.09	11.1	5.25	1.00	4
552	0.35	11.1	5.25	1.00	19
553	0.79	11.1	5.25	1.00	26
554	1.41	11.1	5.25	1.00	24
555	2.20	11.1	5.25	1.00	26
556	3.17	11.1	5.25	1.00	32
557	4.31	11.1	5.25	1.00	38
558	5.63	11.1	5.25	1.00	39
559	7.13	11.1	5.25	1.00	42
560	8.80	11.1	5.25	1.00	40
561	0.00	15.1	2.00	1.00	3
562	0.00	15.1	2.00	1.00	0
563	0.07	15.1	2.00	1.00	-12
564	0.26	15.1	2.00	1.00	10
565	0.59	15.1	2.00	1.00	12
566	1.04	15.1	2.00	1.00	11
567	1.63	15.1	2.00	1.00	11
568	2.35	15.1	2.00	1.00	15
569	3.20	15.1	2.00	1.00	15
570	4.18	15.1	2.00	1.00	12
571	5.28	15.1	2.00	1.00	18
572	6.52	15.1	2.00	1.00	14
573	0.00	15.1	2.75	1.00	8
574	0.00	15.1	2.75	1.00	4
575	0.07	15.1	2.75	1.00	-15
576	0.26	15.1	2.75	1.00	12
577	0.59	15.1	2.75	1.00	13
578	1.04	15.1	2.75	1.00	14
579	1.63	15.1	2.75	1.00	11
580	2.35	15.1	2.75	1.00	13
581	3.20	15.1	2.75	1.00	14
582	4.18	15.1	2.75	1.00	9
583	5.28	15.1	2.75	1.00	12
584	6.52	15.1	2.75	1.00	11
585	0.00	15.1	3.25	1.00	0
586	0.00	15.1	3.25	1.00	1
587	0.07	15.1	3.25	1.00	-16
588	0.26	15.1	3.25	1.00	12
589	0.59	15.1	3.25	1.00	13
590	1.04	15.1	3.25	1.00	14
591	1.63	15.1	3.25	1.00	13
592	2.35	15.1	3.25	1.00	13
593	3.20	15.1	3.25	1.00	14
594	4.18	15.1	3.25	1.00	15
595	5.28	15.1	3.25	1.00	15
596	6.52	15.1	3.25	1.00	16
597	0.00	15.1	5.25	1.00	-1
598	0.00	15.1	5.25	1.00	2
599	0.07	15.1	5.25	1.00	-26
600	0.26	15.1	5.25	1.00	3
601	0.59	15.1	5.25	1.00	19
602	1.04	15.1	5.25	1.00	25
603	1.63	15.1	5.25	1.00	29
604	2.35	15.1	5.25	1.00	19

Run	J*	% Circ.	a/D	j/D	Φ
605	3.20	15.1	5.25	1.00	22
606	4.18	15.1	5.25	1.00	20
607	5.28	15.1	5.25	1.00	19
608	6.52	15.1	5.25	1.00	23
609	0.00	19.4	2.00	1.00	1
610	0.00	19.4	2.00	1.00	0
611	0.05	19.4	2.00	1.00	-18
612	0.21	19.4	2.00	1.00	11
613	0.46	19.4	2.00	1.00	18
614	0.82	19.4	2.00	1.00	18
615	1.28	19.4	2.00	1.00	20
616	1.85	19.4	2.00	1.00	22
617	2.51	19.4	2.00	1.00	25
618	3.28	19.4	2.00	1.00	23
619	4.15	19.4	2.00	1.00	24
620	5.13	19.4	2.00	1.00	20
621	0.00	19.4	2.75	1.00	0
622	0.00	19.4	2.75	1.00	0
623	0.05	19.4	2.75	1.00	-20
624	0.21	19.4	2.75	1.00	11
625	0.46	19.4	2.75	1.00	19
626	0.82	19.4	2.75	1.00	19
627	1.28	19.4	2.75	1.00	21
628	1.85	19.4	2.75	1.00	21
629	2.51	19.4	2.75	1.00	23
630	3.28	19.4	2.75	1.00	24
631	4.15	19.4	2.75	1.00	27
632	5.13	19.4	2.75	1.00	26
633	0.00	19.4	3.25	1.00	0
634	0.00	19.4	3.25	1.00	0
635	0.05	19.4	3.25	1.00	-22
636	0.21	19.4	3.25	1.00	10
637	0.46	19.4	3.25	1.00	16
638	0.82	19.4	3.25	1.00	18
639	1.28	19.4	3.25	1.00	20
640	1.85	19.4	3.25	1.00	23
641	2.51	19.4	3.25	1.00	25
642	3.28	19.4	3.25	1.00	26
643	4.15	19.4	3.25	1.00	27
644	5.13	19.4	3.25	1.00	28
645	0.00	19.4	5.25	1.00	5
646	0.00	19.4	5.25	1.00	2
647	0.05	19.4	5.25	1.00	-23
648	0.21	19.4	5.25	1.00	7
649	0.46	19.4	5.25	1.00	19
650	0.82	19.4	5.25	1.00	21
651	1.28	19.4	5.25	1.00	26
652	1.85	19.4	5.25	1.00	25
653	2.51	19.4	5.25	1.00	29
654	3.28	19.4	5.25	1.00	32
655	4.15	19.4	5.25	1.00	34
656	5.13	19.4	5.25	1.00	37
657	0.00	29.5	2.00	1.00	3
658	0.00	29.5	2.00	1.00	4
659	0.04	29.5	2.00	1.00	-8
660	0.14	29.5	2.00	1.00	0
661	0.31	29.5	2.00	1.00	19
662	0.56	29.5	2.00	1.00	36
663	0.87	29.5	2.00	1.00	49
664	1.26	29.5	2.00	1.00	60
665	1.71	29.5	2.00	1.00	63
666	2.24	29.5	2.00	1.00	66
667	2.83	29.5	2.00	1.00	68
668	3.49	29.5	2.00	1.00	70
669	0.00	29.5	2.75	1.00	5
670	0.00	29.5	2.75	1.00	5
671	0.04	29.5	2.75	1.00	-12
672	0.14	29.5	2.75	1.00	-11
673	0.31	29.5	2.75	1.00	19
674	0.56	29.5	2.75	1.00	41
675	0.87	29.5	2.75	1.00	61
676	1.26	29.5	2.75	1.00	71
677	1.71	29.5	2.75	1.00	76
678	2.24	29.5	2.75	1.00	82
679	2.83	29.5	2.75	1.00	84
680	3.49	29.5	2.75	1.00	84
681	0.00	29.5	3.25	1.00	5
682	0.00	29.5	3.25	1.00	4
683	0.04	29.5	3.25	1.00	-13
684	0.14	29.5	3.25	1.00	0
685	0.31	29.5	3.25	1.00	20
686	0.56	29.5	3.25	1.00	42
687	0.87	29.5	3.25	1.00	58
688	1.26	29.5	3.25	1.00	66
689	1.71	29.5	3.25	1.00	70
690	2.24	29.5	3.25	1.00	76
691	2.83	29.5	3.25	1.00	75
692	3.49	29.5	3.25	1.00	77
693	0.00	29.5	5.25	1.00	8
694	0.00	29.5	5.25	1.00	8
695	0.04	29.5	5.25	1.00	13
696	0.14	29.5	5.25	1.00	16
697	0.31	29.5	5.25	1.00	24
698	0.56	29.5	5.25	1.00	43
699	0.87	29.5	5.25	1.00	67
700	1.26	29.5	5.25	1.00	80
701	1.71	29.5	5.25	1.00	93
702	2.24	29.5	5.25	1.00	87
703	2.83	29.5	5.25	1.00	92
704	3.49	29.5	5.25	1.00	95
705	0.00	50.0	2.00	1.00	-1
706	0.00	50.0	2.00	1.00	0
707	0.02	50.0	2.00	1.00	-4
708	0.06	50.0	2.00	1.00	-9
709	0.14	50.0	2.00	1.00	-9
710	0.25	50.0	2.00	1.00	-10
711	0.39	50.0	2.00	1.00	-5
712	0.57	50.0	2.00	1.00	70
713	0.77	50.0	2.00	1.00	90
714	1.01	50.0	2.00	1.00	93
715	1.27	50.0	2.00	1.00	89
716	1.57	50.0	2.00	1.00	90
717	0.00	50.0	2.75	1.00	7
718	0.00	50.0	2.75	1.00	4
719	0.02	50.0	2.75	1.00	-4
720	0.06	50.0	2.75	1.00	-7
721	0.14	50.0	2.75	1.00	-6
722	0.25	50.0	2.75	1.00	-5

Run	*J**	% Circ.	*a/D*	*j/D*	*Φ*
723	0.39	50.0	2.75	1.00	47
724	0.57	50.0	2.75	1.00	77
725	0.77	50.0	2.75	1.00	96
726	1.01	50.0	2.75	1.00	87
727	1.27	50.0	2.75	1.00	86
728	1.57	50.0	2.75	1.00	89
729	0.00	50.0	3.25	1.00	0
730	0.00	50.0	3.25	1.00	4
731	0.02	50.0	3.25	1.00	-4
732	0.06	50.0	3.25	1.00	-7
733	0.14	50.0	3.25	1.00	-8
734	0.25	50.0	3.25	1.00	-5
735	0.39	50.0	3.25	1.00	52
736	0.57	50.0	3.25	1.00	77
737	0.77	50.0	3.25	1.00	88
738	1.01	50.0	3.25	1.00	91
739	1.27	50.0	3.25	1.00	86
740	1.57	50.0	3.25	1.00	87
741	0.00	50.0	5.25	1.00	2
742	0.00	50.0	5.25	1.00	2
743	0.02	50.0	5.25	1.00	-4
744	0.06	50.0	5.25	1.00	-10
745	0.14	50.0	5.25	1.00	-7
746	0.25	50.0	5.25	1.00	-9
747	0.39	50.0	5.25	1.00	37
748	0.57	50.0	5.25	1.00	58
749	0.77	50.0	5.25	1.00	85
750	1.01	50.0	5.25	1.00	87
751	1.27	50.0	5.25	1.00	85
752	1.57	50.0	5.25	1.00	80

A.3 Test Parameters of Three-Component PIV Study

Run	J^*	% Circ.	*a/D*	*j/D*	Φ	*xD* downstream
753	0.00	29.5	2.00	1.00	3	8
754	0.00	29.5	2.00	1.00	4	8
755	0.04	29.5	2.00	1.00	-8	8
756	0.14	29.5	2.00	1.00	0	8
757	0.31	29.5	2.00	1.00	19	8
758	0.56	29.5	2.00	1.00	36	8
759	0.87	29.5	2.00	1.00	49	8
760	1.26	29.5	2.00	1.00	60	8
761	1.71	29.5	2.00	1.00	63	8
762	2.24	29.5	2.00	1.00	66	8
763	2.83	29.5	2.00	1.00	68	8
764	3.49	29.5	2.00	1.00	70	8
765	0.00	29.5	5.25	1.00	8	8
766	0.00	29.5	5.25	1.00	8	8
767	0.04	29.5	5.25	1.00	13	8
768	0.14	29.5	5.25	1.00	16	8
769	0.56	29.5	5.25	1.00	43	8
770	0.87	29.5	5.25	1.00	67	8
771	1.26	29.5	5.25	1.00	80	8
772	0.00	50.0	2.75	1.00	7	8
773	0.00	50.0	2.75	1.00	4	8
774	0.02	50.0	2.75	1.00	-4	8
775	0.06	50.0	2.75	1.00	-7	8
776	0.14	50.0	2.75	1.00	-6	8
777	0.25	50.0	2.75	1.00	-5	8
778	0.39	50.0	2.75	1.00	47	8
779	0.57	50.0	2.75	1.00	77	8
780	0.77	50.0	2.75	1.00	96	8
781	1.01	50.0	2.75	1.00	87	8
782	1.27	50.0	2.75	1.00	86	8
783	1.57	50.0	2.75	1.00	89	8
784	0.00	50.0	3.25	1.00	0	8
785	0.00	50.0	3.25	1.00	4	8
786	0.02	50.0	3.25	1.00	-4	8
787	0.06	50.0	3.25	1.00	-7	8
788	0.14	50.0	3.25	1.00	-8	8
789	0.39	50.0	3.25	1.00	52	8
790	0.57	50.0	3.25	1.00	77	8
791	0.77	50.0	3.25	1.00	88	8
792	1.01	50.0	3.25	1.00	91	8
793	1.27	50.0	3.25	1.00	86	8
794	1.57	50.0	3.25	1.00	87	8
795	0.00	29.5	2.00	1.00	3	12
796	0.00	29.5	2.00	1.00	4	12
797	0.04	29.5	2.00	1.00	-8	12
798	0.14	29.5	2.00	1.00	0	12
799	0.31	29.5	2.00	1.00	19	12
800	0.56	29.5	2.00	1.00	36	12
801	0.87	29.5	2.00	1.00	49	12
802	1.26	29.5	2.00	1.00	60	12
803	1.71	29.5	2.00	1.00	63	12
804	2.24	29.5	2.00	1.00	66	12
805	2.83	29.5	2.00	1.00	68	12
806	3.49	29.5	2.00	1.00	70	12
807	0.00	29.5	5.25	1.00	8	12
808	0.00	29.5	5.25	1.00	8	12
809	0.04	29.5	5.25	1.00	13	12
810	0.14	29.5	5.25	1.00	16	12
811	0.31	29.5	5.25	1.00	24	12
812	0.56	29.5	5.25	1.00	43	12
813	0.87	29.5	5.25	1.00	67	12
814	1.26	29.5	5.25	1.00	80	12
815	1.71	29.5	5.25	1.00	93	12
816	2.24	29.5	5.25	1.00	87	12
817	2.83	29.5	5.25	1.00	92	12
818	3.49	29.5	5.25	1.00	95	12
819	0.00	50.0	2.75	1.00	7	12
820	0.00	50.0	2.75	1.00	4	12
821	0.02	50.0	2.75	1.00	-4	12
822	0.06	50.0	2.75	1.00	-7	12
823	0.14	50.0	2.75	1.00	-6	12
824	0.25	50.0	2.75	1.00	-5	12
825	0.39	50.0	2.75	1.00	47	12
826	0.57	50.0	2.75	1.00	77	12
827	0.77	50.0	2.75	1.00	96	12
828	1.01	50.0	2.75	1.00	87	12
829	1.27	50.0	2.75	1.00	86	12
830	1.57	50.0	2.75	1.00	89	12
831	0.00	50.0	3.25	1.00	0	12
832	0.00	50.0	3.25	1.00	4	12
833	0.02	50.0	3.25	1.00	-4	12
834	0.06	50.0	3.25	1.00	-7	12
835	0.14	50.0	3.25	1.00	-8	12
836	0.39	50.0	3.25	1.00	52	12
837	0.57	50.0	3.25	1.00	77	12
838	0.77	50.0	3.25	1.00	88	12
839	1.01	50.0	3.25	1.00	91	12
840	1.27	50.0	3.25	1.00	86	12
841	1.57	50.0	3.25	1.00	87	12

Appendix B

Machinist Drawings

Shown are the machinist drawings created in Solid Edge v. 20, beginning with the test assembly and curved wall radius drawings and followed by sections including modulator drawings for the jet impingement and circumferential exit slot studies, respectively.

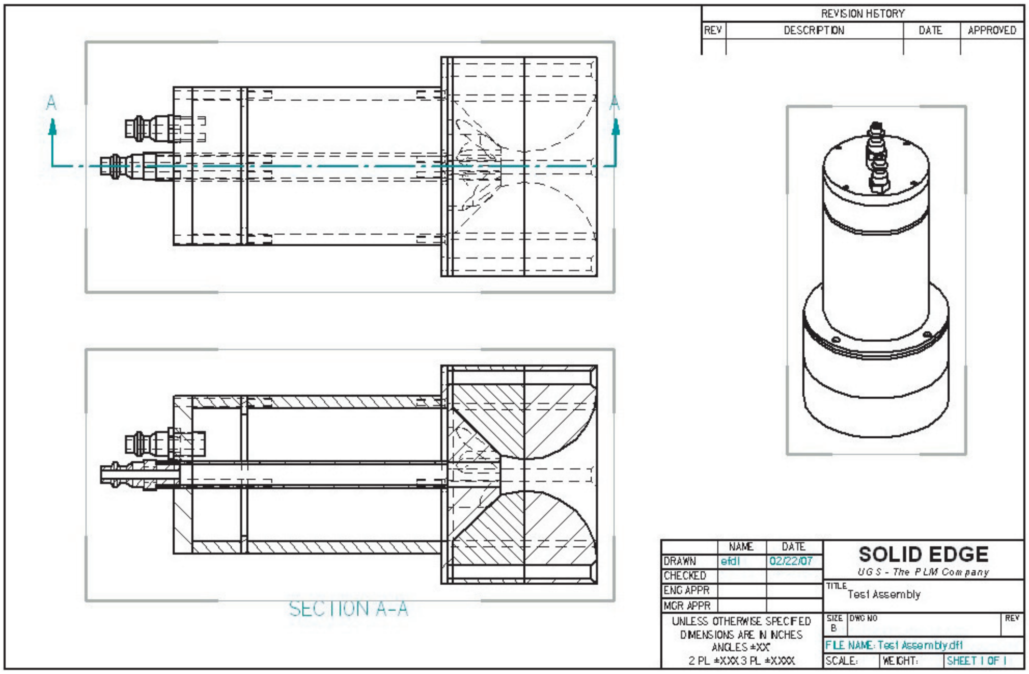

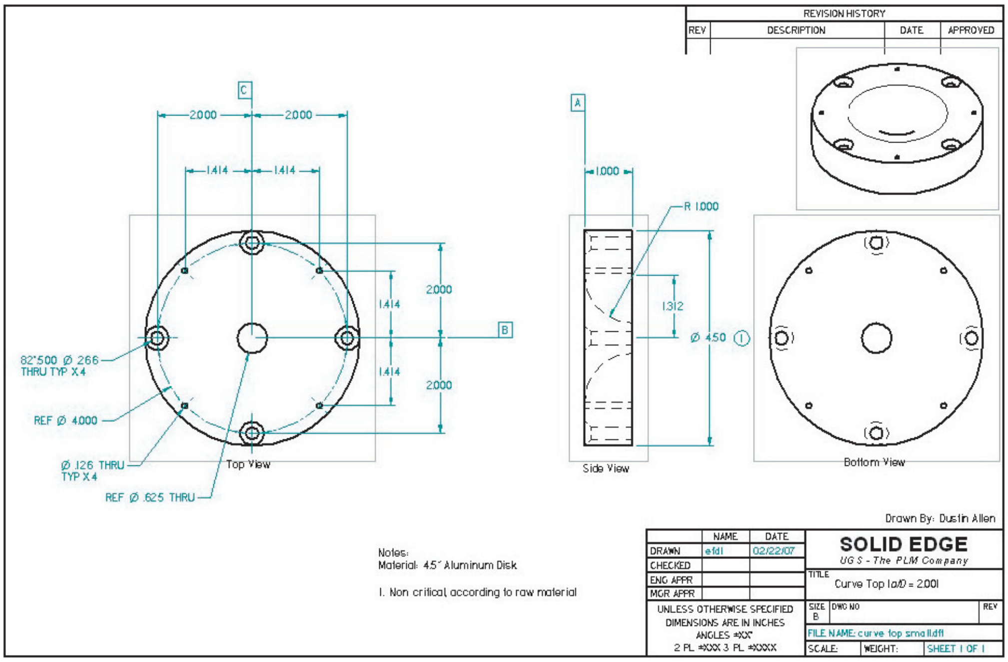
REVISION HISTORY
REV
DESCRIPTION
DATE
APPROVED
C
2.000
2.000
1.414
1.414
A
1.000
R 1.000
2.000
1.414
1.414
2.000
1.312
Ø 4.50 ①
B
82°.500 Ø .266
THRU TYP X4
REF Ø 4.000
Ø .126 THRU
TYP X4
REF Ø .625 THRU
Top View
Side View
Bottom View
Drawn By: Dustin Allen
Notes:
Material: 4.5" Aluminum Disk
1. Non critical according to raw material
NAME
DATE
DRAWN
efdl
02/22/07
CHECKED
ENG APPR
MGR APPR
UNLESS OTHERWISE SPECIFIED
DIMENSIONS ARE IN INCHES
ANGLES ±XX°
2 PL ±XXX 3 PL ±XXXX
SOLID EDGE
UGS - The PLM Company
TITLE
Curve Top la/D = 2.001
SIZE
B
DWG NO
REV
FILE NAME: curve top small.dft
SCALE:
WEIGHT:
SHEET 1 OF 1

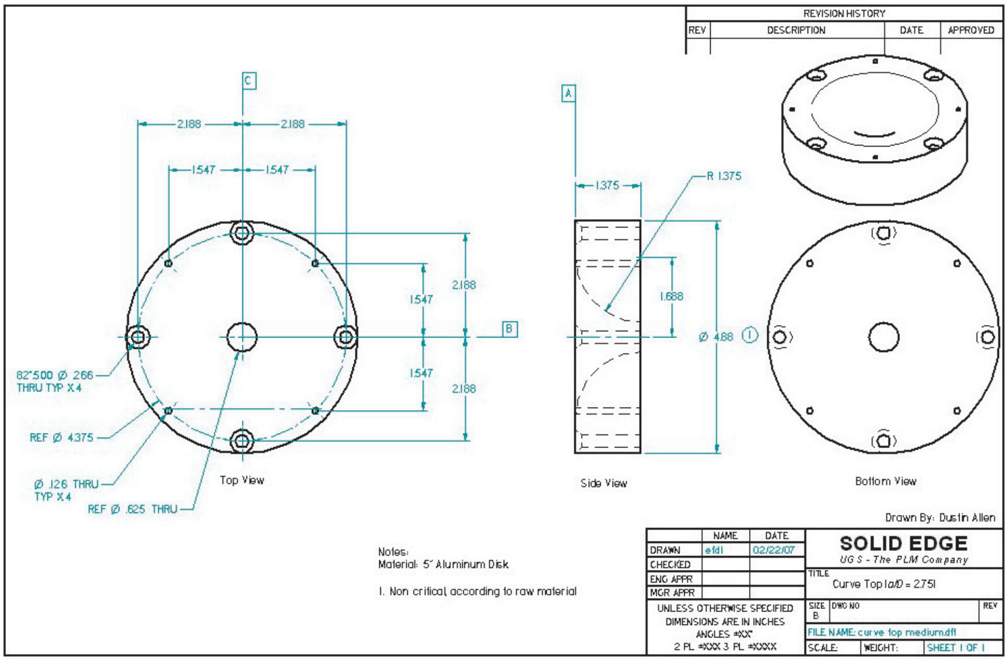
REVISION HISTORY
REV
DESCRIPTION
DATE
APPROVED
C
2.188
2.188
1.547
1.547
A
1.375
R 1.375
2.188
1.547
1.547
2.188
1.688
Ø 4.88 ①
B
82°.500 Ø .266
THRU TYP X4
REF Ø 4.375
Ø .126 THRU
TYP X4
REF Ø .625 THRU
Top View
Side View
Bottom View
Drawn By: Dustin Allen
Notes:
Material: 5" Aluminum Disk
1. Non critical according to raw material
NAME
DATE
DRAWN
efdl
02/22/07
CHECKED
ENG APPR
MGR APPR
UNLESS OTHERWISE SPECIFIED
DIMENSIONS ARE IN INCHES
ANGLES ±XX°
2 PL ±XXX 3 PL ±XXXX
SOLID EDGE
UGS - The PLM Company
TITLE
Curve Top la/D = 2.751
SIZE
B
DWG NO
REV
FILE NAME: curve top medium.dft
SCALE:
WEIGHT:
SHEET 1 OF 1

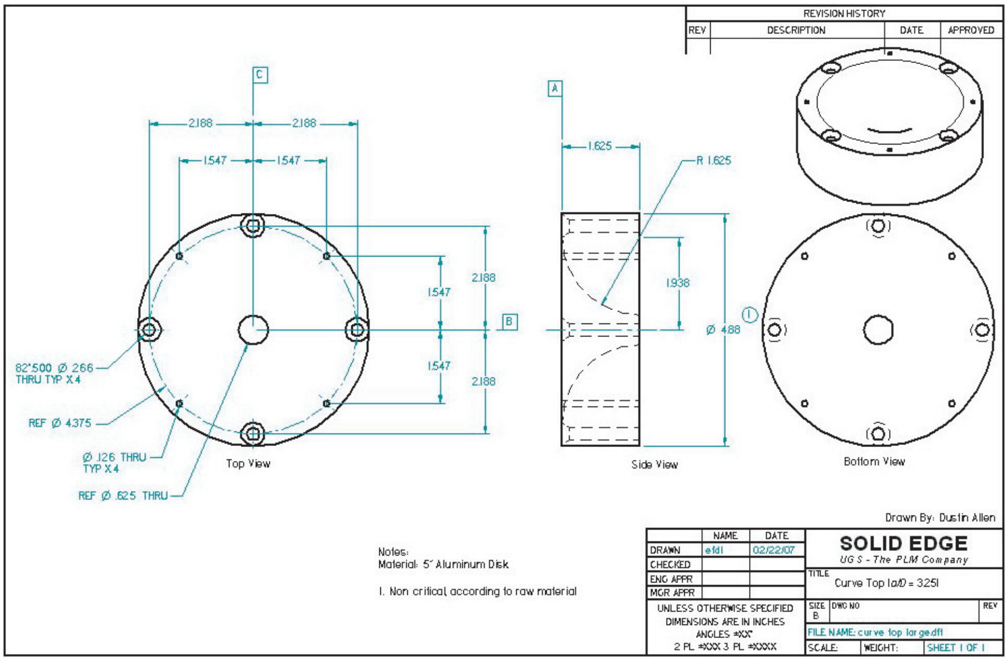
REVISION HISTORY
REV
DESCRIPTION
DATE
APPROVED
C
2.188
2.188
1.547
1.547
2.188
1.547
1.547
2.188
B
82°.500 Ø .266
THRU TYP X 4
REF Ø 4.375
Ø .126 THRU
TYP X 4
REF Ø .625 THRU
Top View
A
1.625
R 1.625
1.938
Ø 4.88
①
Side View
Bottom View
Drawn By: Dustin Allen
Notes:
Material: 5" Aluminum Disk
1. Non critical, according to raw material
NAME
DATE
DRAWN
efdl
02/22/07
CHECKED
ENG APPR
MGR APPR
UNLESS OTHERWISE SPECIFIED
DIMENSIONS ARE IN INCHES
ANGLES ±XX°
2 PL ±XXX 3 PL ±XXXX
SOLID EDGE
UGS - The PLM Company
TITLE
Curve Top la/D = 3251
SIZE
B
DWG NO
REV
FILE NAME: curve top large.dft
SCALE:
WEIGHT:
SHEET 1 OF 1

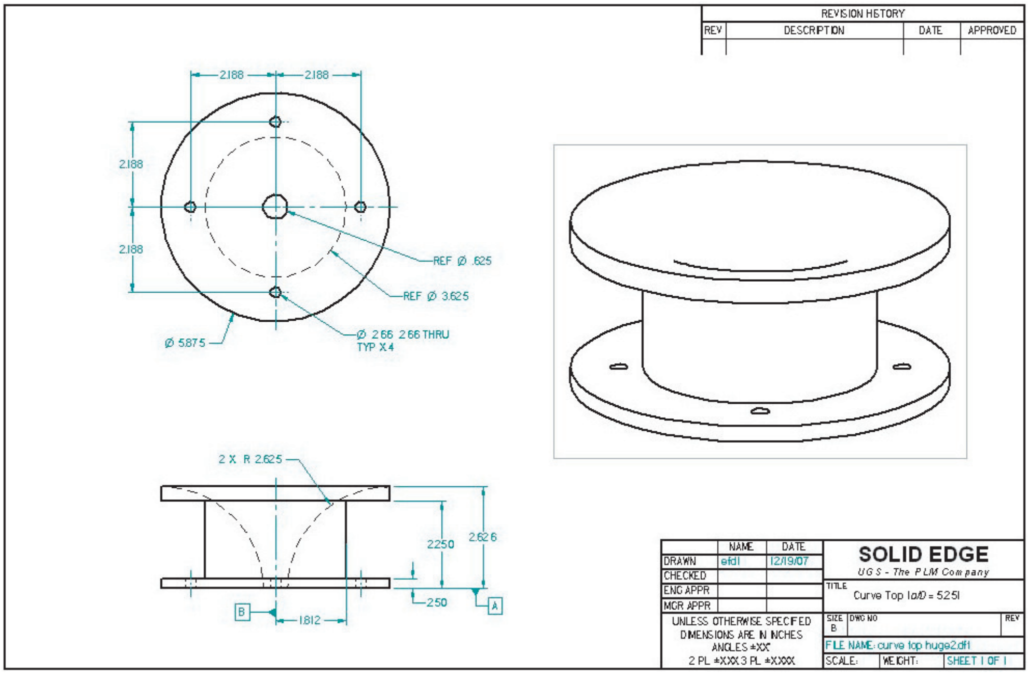
REVISION HISTORY
REV
DESCRIPTION
DATE
APPROVED
2.188
2.188
2.188
2.188
REF Ø .625
REF Ø 3.625
Ø .266 .266 THRU
TYP X 4
Ø 5.875
2 X R 2.625
2.250
2.626
.250
A
B
1.812
NAME
DATE
DRAWN
efdl
12/19/07
CHECKED
ENG APPR
MGR APPR
UNLESS OTHERWISE SPECIFIED
DIMENSIONS ARE IN INCHES
ANGLES ±XX°
2 PL ±XXX 3 PL ±XXXX
SOLID EDGE
UGS - The PLM Company
TITLE
Curve Top la/D = 5251
SIZE
B
DWG NO
REV
FILE NAME: curve top huge2.dft
SCALE:
WEIGHT:
SHEET 1 OF 1

B.1 Machine Shop Drawings of Jet Impingement Study

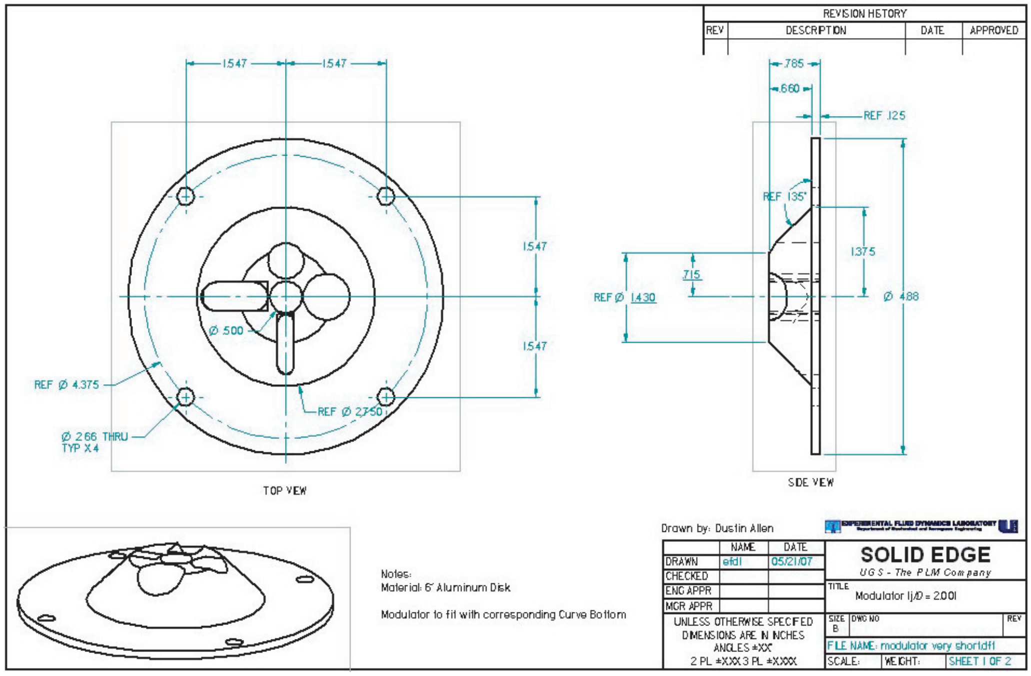

Notes:
Material: 6" Aluminum Disk

Modulator to fit with corresponding Curve Bottom

Drawn by: Dustin Allen

	NAME	DATE
DRAWN	efdl	05/21/07
CHECKED		
ENG APPR		
MGR APPR		

UNLESS OTHERWISE SPECIFIED
DIMENSIONS ARE IN INCHES
ANGLES ±XX°
2 PL ±XXX 3 PL ±XXXX

TITLE Modulator lj/D = 2.001

SIZE B
DWG NO
REV

FILE NAME: modulator very short.dft

SCALE:
WEIGHT:
SHEET 1 OF 2

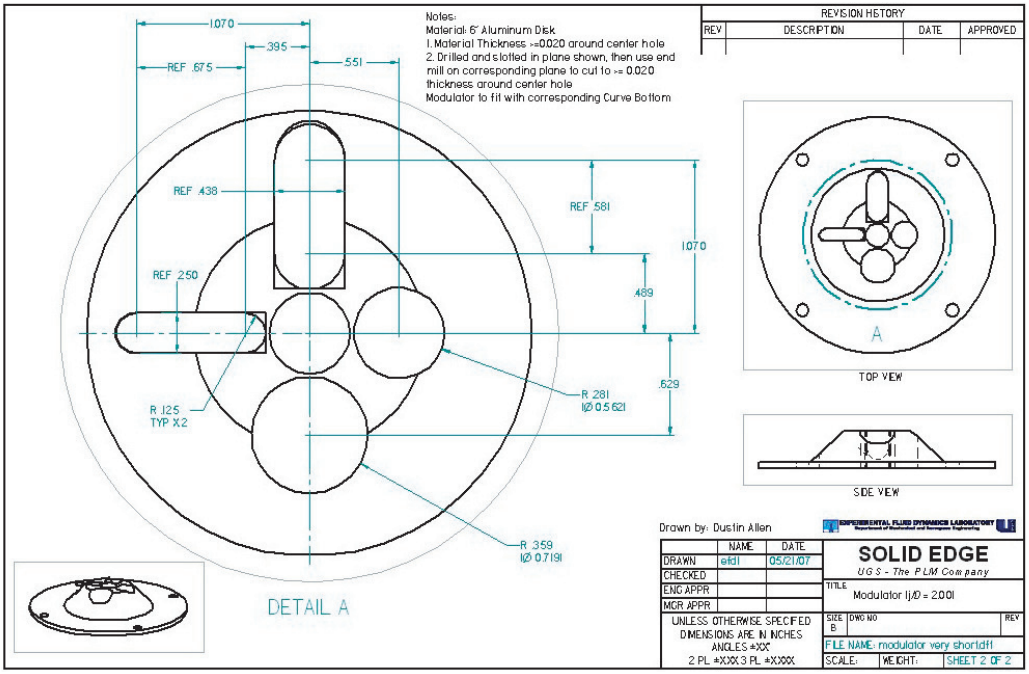

Notes:
Material: 6" Aluminum Disk
1. Material Thickness >=0.020 around center hole
2. Drilled and slotted in plane shown, then use end mill on corresponding plane to cut to >= 0.020 thickness around center hole
Modulator to fit with corresponding Curve Bottom

Drawn by: Dustin Allen

	NAME	DATE
DRAWN	efdl	05/21/07
CHECKED		
ENG APPR		
MGR APPR		

UNLESS OTHERWISE SPECIFIED
DIMENSIONS ARE IN INCHES
ANGLES ±XX°
2 PL ±XXX 3 PL ±XXXX

SOLID EDGE
UGS - The PLM Company

TITLE Modulator lj/D = 2.001
SIZE B
DWG NO
REV
FILE NAME: modulator very short.dft
SCALE:
WEIGHT:
SHEET 2 OF 2

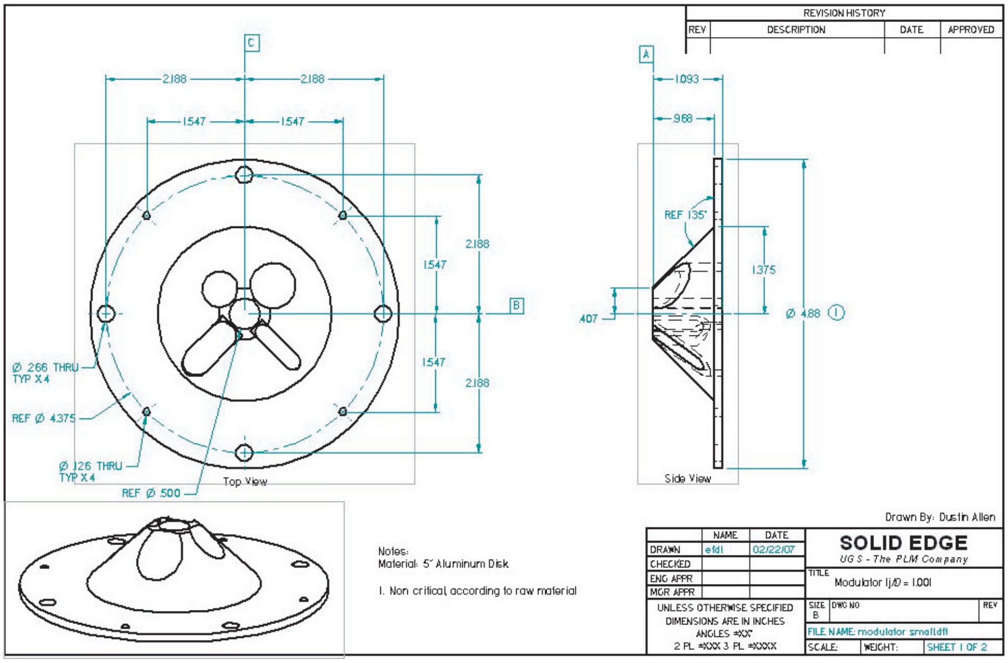

Drawn By: Dustin Allen

Notes:
Material: 5" Aluminum Disk

1. Non critical, according to raw material

	NAME	DATE
DRAWN	efdl	02/22/07
CHECKED		
ENG APPR		
MGR APPR		

UNLESS OTHERWISE SPECIFIED
DIMENSIONS ARE IN INCHES
ANGLES ±XX°
2 PL ±XXX 3 PL ±XXXX

SOLID EDGE
UGS - The PLM Company

TITLE Modulator lj/D = 1.001
SIZE B
DWG NO
REV
FILE NAME: modulator small.dft
SCALE:
WEIGHT:
SHEET 1 OF 2

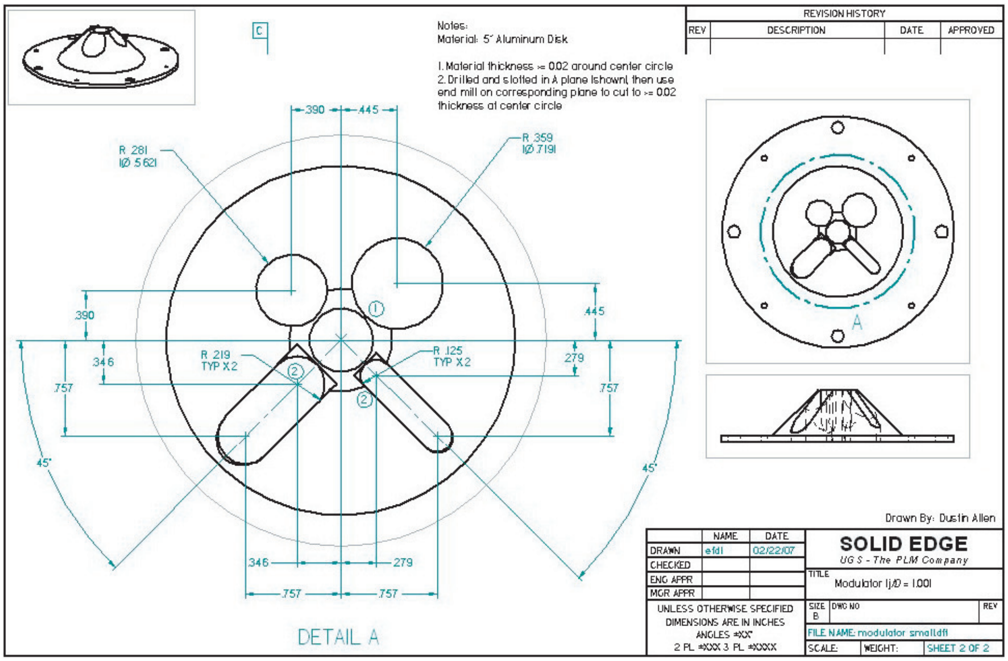

Notes:
Material: 5″ Aluminum Disk

1. Material thickness >= 0.02 around center circle
2. Drilled and slotted in A plane (shown), then use end mill on corresponding plane to cut to >= 0.02 thickness at center circle

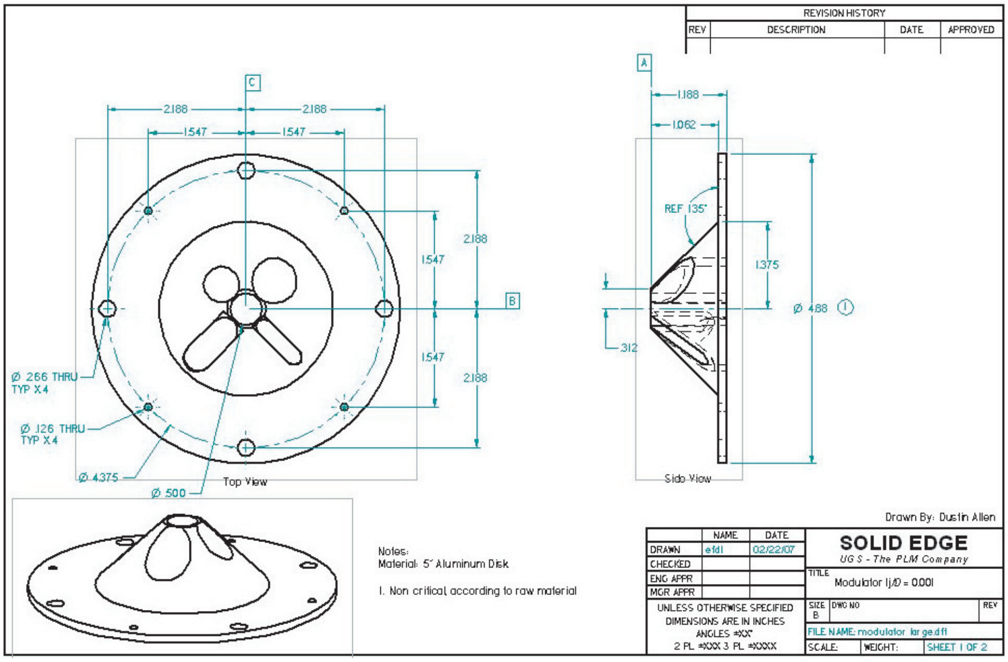

Notes:
Material: 5″ Aluminum Disk

1. Non critical, according to raw material

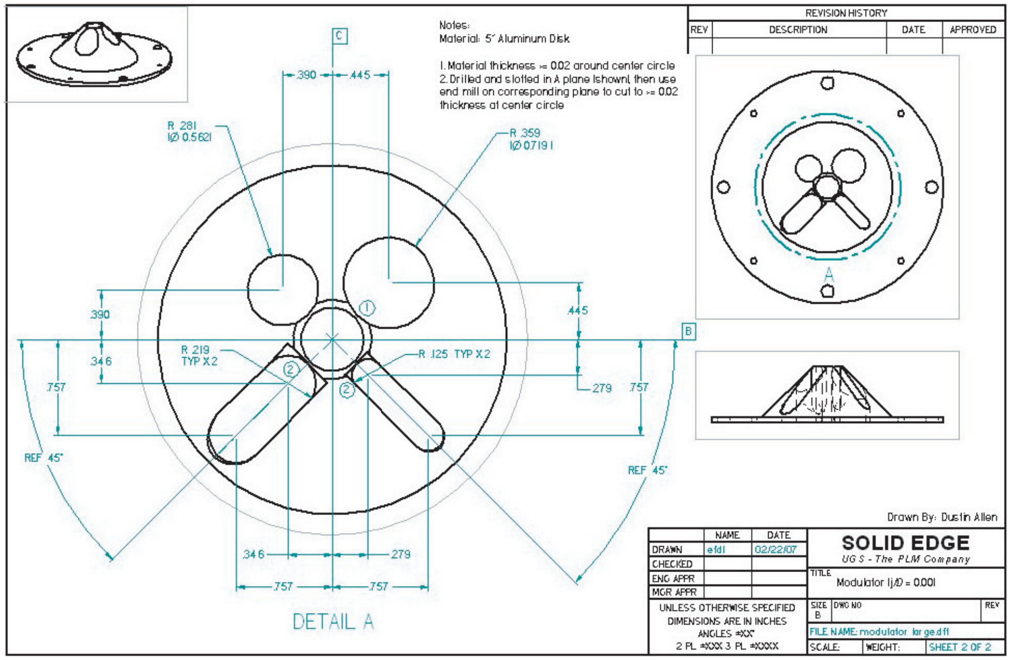

Notes:
Material: 5" Aluminum Disk

1. Material thickness >= 0.02 around center circle
2. Drilled and slotted in A plane (shown), then use end mill on corresponding plane to cut to >= 0.02 thickness at center circle

Drawn By: Dustin Allen

	NAME	DATE
DRAWN	efdl	02/22/07
CHECKED		
ENG APPR		
MGR APPR		

UNLESS OTHERWISE SPECIFIED
DIMENSIONS ARE IN INCHES
ANGLES ±XX°
2 PL ±XXX 3 PL ±XXXX

SOLID EDGE
UGS - The PLM Company

TITLE
Modulator lj/D = 0.001

SIZE B
DWG NO
REV

FILE NAME: modulator large.dft

SCALE:
WEIGHT:
SHEET 2 OF 2

B.2 Machine Shop Drawings of Exit Slot Study

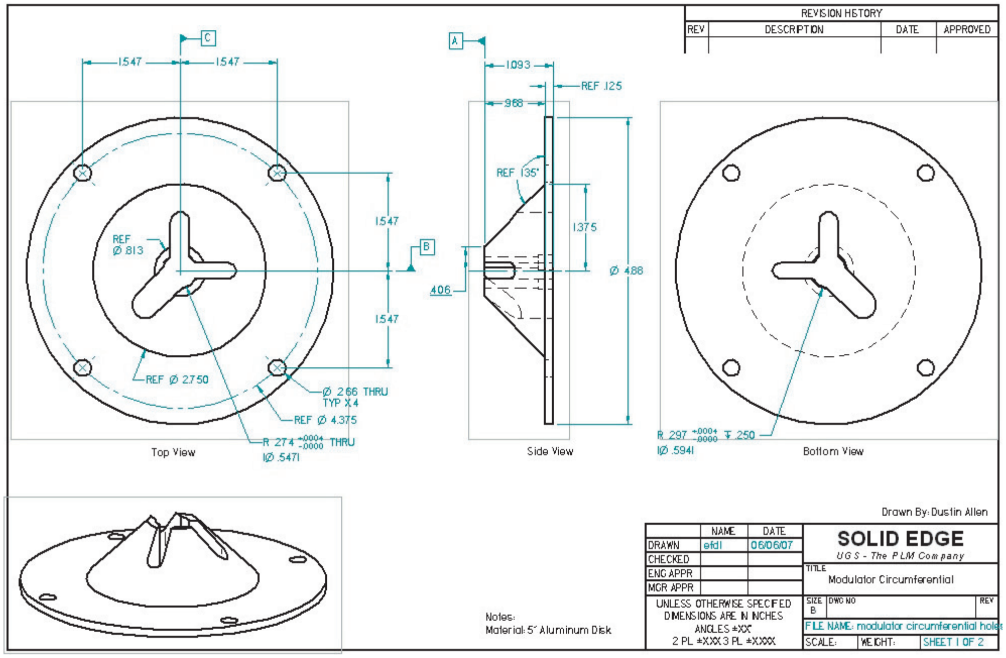

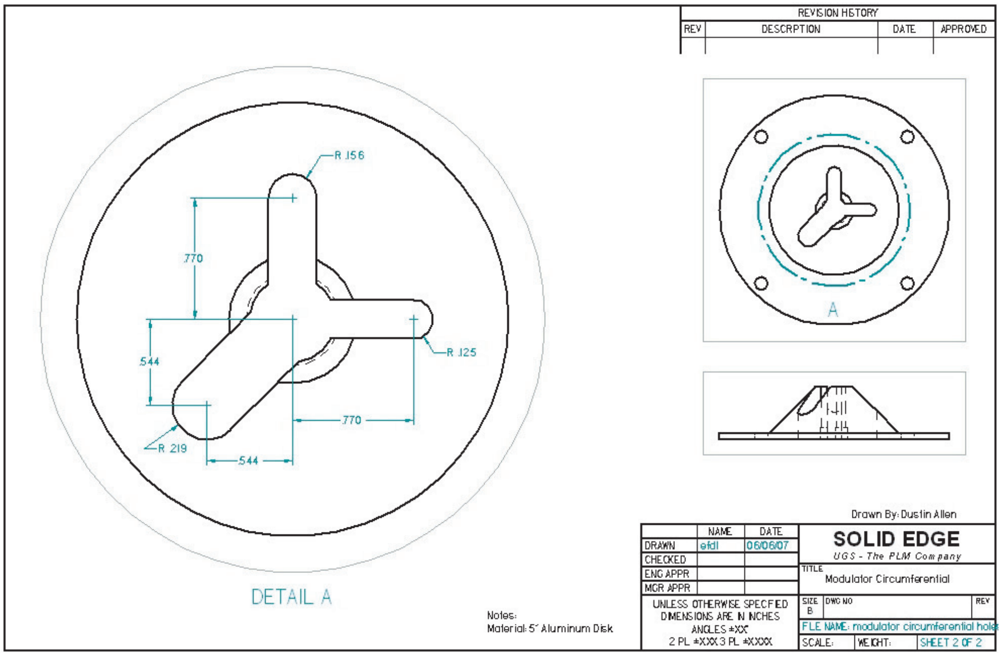
REVISION HISTORY
REV
DESCRIPTION
DATE
APPROVED
R .156
.770
R .125
.544
.770
R .219
.544
DETAIL A
A
Drawn By: Dustin Allen
NAME
DATE
DRAWN
efdl
06/06/07
CHECKED
ENG APPR
MGR APPR
SOLID EDGE
UGS - The PLM Company
TITLE
Modulator Circumferential
UNLESS OTHERWISE SPECIFIED
DIMENSIONS ARE IN INCHES
ANGLES ±XX°
2 PL ±XXX 3 PL ±XXXX
SIZE
B
DWG NO
REV
FILE NAME: modulator circumferential hole
SCALE:
WEIGHT:
SHEET 2 OF 2
Notes:
Material: 5" Aluminum Disk

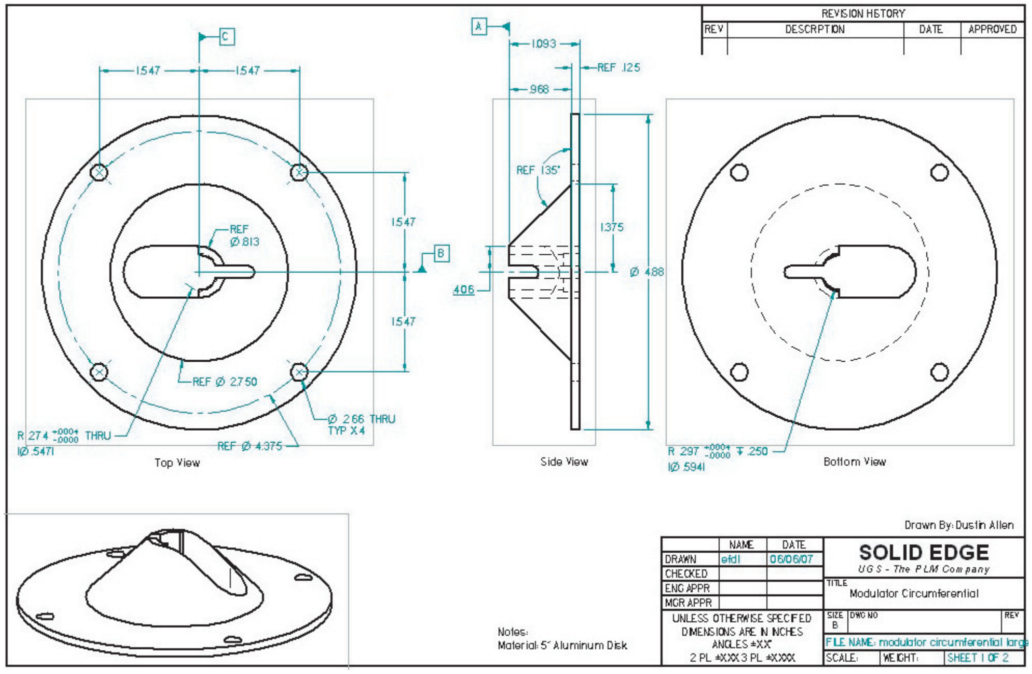
REVISION HISTORY
REV
DESCRIPTION
DATE
APPROVED
C
1.547
1.547
REF
Ø .813
1.547
B
1.547
REF Ø 2.750
Ø .266 THRU
TYP X4
R .274 +.0004 -.0000 THRU
IØ .5471
REF Ø 4.375
Top View
A
1.093
REF .125
.968
REF 135°
1.375
Ø 4.88
.406
Side View
R .297 +.0004 -.0000 ↧ .250
IØ .5941
Bottom View
Drawn By: Dustin Allen
NAME
DATE
DRAWN
efdl
06/06/07
CHECKED
ENG APPR
MGR APPR
SOLID EDGE
UGS - The PLM Company
TITLE
Modulator Circumferential
UNLESS OTHERWISE SPECIFIED
DIMENSIONS ARE IN INCHES
ANGLES ±XX°
2 PL ±XXX 3 PL ±XXXX
SIZE
B
DWG NO
REV
FILE NAME: modulator circumferential large
SCALE:
WEIGHT:
SHEET 1 OF 2
Notes:
Material: 5" Aluminum Disk

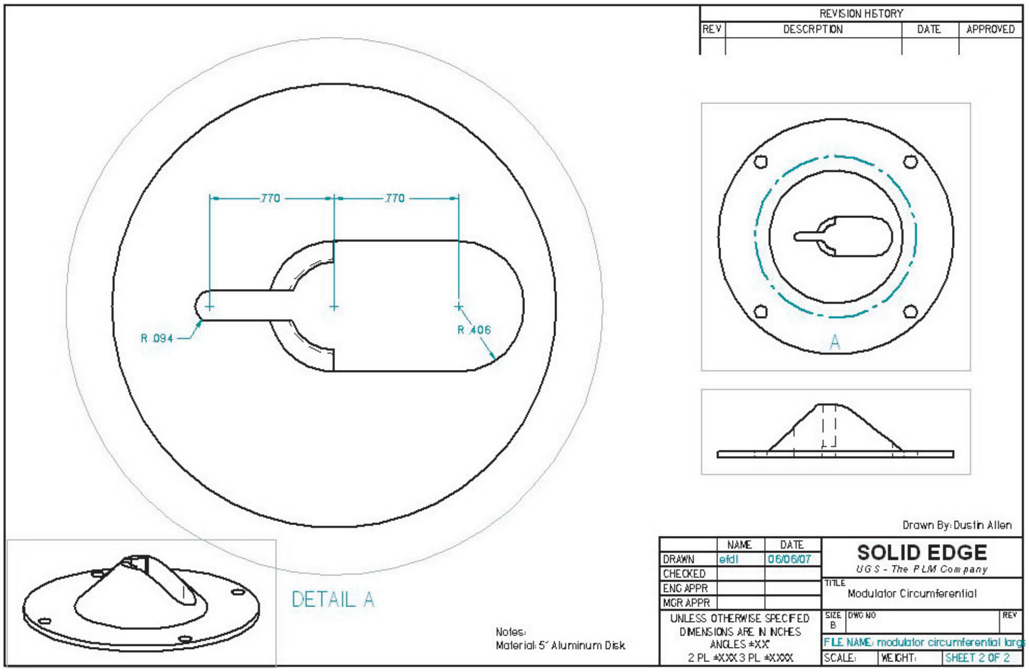
REVISION HISTORY
REV
DESCRIPTION
DATE
APPROVED
.770
.770
R .094
R .406
A
DETAIL A
Drawn By: Dustin Allen
NAME
DATE
DRAWN
efdl
06/06/07
CHECKED
ENG APPR
MGR APPR
SOLID EDGE
UGS - The PLM Company
TITLE
Modulator Circumferential
UNLESS OTHERWISE SPECIFIED
DIMENSIONS ARE IN INCHES
ANGLES ±X.X°
2 PL ±X.XX 3 PL ±X.XXX
SIZE
B
DWG NO
REV
FILE NAME: modulator circumferential larg
SCALE:
WEIGHT:
SHEET 2 OF 2
Notes:
Material: 5" Aluminum Disk

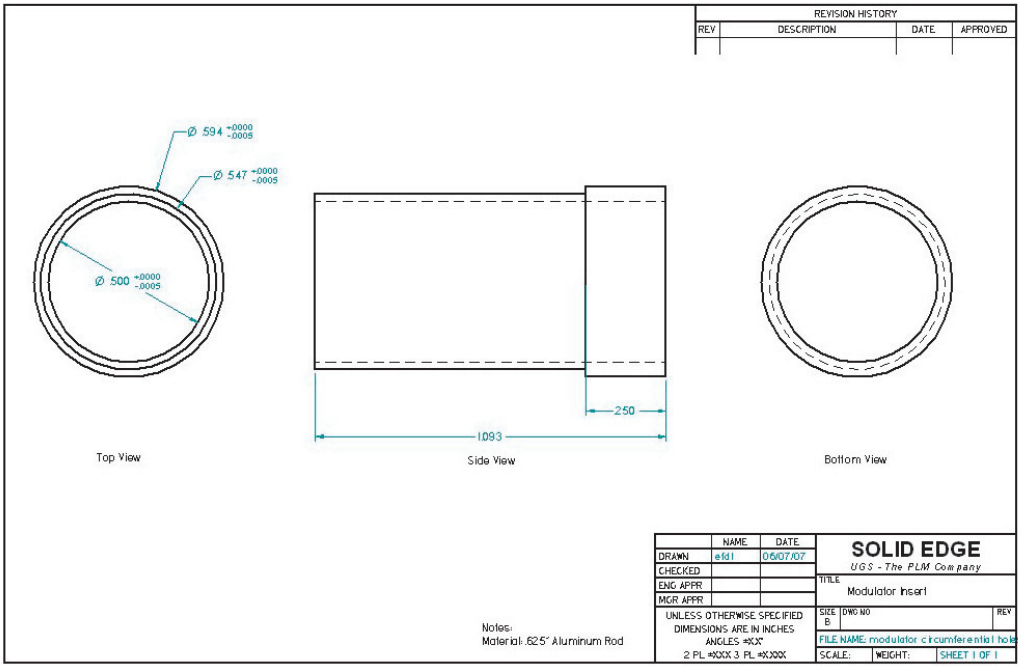
REVISION HISTORY
REV
DESCRIPTION
DATE
APPROVED
Ø .594 +.0000 -.0005
Ø .547 +.0000 -.0005
Ø .500 +.0000 -.0005
.250
1.093
Top View
Side View
Bottom View
NAME
DATE
DRAWN
efdl
06/07/07
CHECKED
ENG APPR
MGR APPR
SOLID EDGE
UGS - The PLM Company
TITLE
Modulator Insert
UNLESS OTHERWISE SPECIFIED
DIMENSIONS ARE IN INCHES
ANGLES ±X.X°
2 PL ±X.XX 3 PL ±X.XXX
SIZE
B
DWG NO
REV
FILE NAME: modulator circumferential hole
SCALE:
WEIGHT:
SHEET 1 OF 1
Notes:
Material: .625" Aluminum Rod